

Qualification of SLM

Additive Manufacturing for Aluminium

Vom Promotionsausschuss der
Technischen Universität Hamburg
zur Erlangung des akademischen Grades

Doktor-Ingenieur(in) (Dr.-Ing.)

genehmigte Dissertation

von
Katja Schmidtke

aus
Zehdenick

2019

Vorsitzender: Herr Prof. Dr. rer. nat. R. God

1. Gutachter: Herr Prof. Dr.-Ing. C. Emmelmann

2. Gutachter: Herr Prof. Dr.-Ing. C. Leyens

Tag der mündlichen Prüfung: 13. Dezember 2018

To

My wonderful husband,

My adorable children,

My beloved family and friends...

Summary

The present thesis QUALIFICATION OF SLM – ADDITIVE MANUFACTURING FOR ALUMINIUM ALLOYS considers the suitability of two aluminum alloys for the additive manufacturing technique Selective Laserbeam Melting (SLM). High cooling rates can be realised in SLM which allow the use of the tailored Al-alloy options Scalmalloy and SilmagAl. The investigations deepen the scholarly understanding of processing both alloys in SLM. Different aspects of the process chain are described, analysed and discussed with regard to define powder and material specifications for aerospace applications. Main process influencing powder characteristics are identified and characterising techniques are discussed. The additive manufactured material of both alloys is comprehensively investigated regarding mechanical and physical properties. As result, different processing routes are identified which aim to meet the final proposed material specification for principle structural elements (PSE) and non-principle structural elements (non-PSE) in aerospace qualifications.

Contents

| | |
|---|-----------|
| Acronyms | 1 |
| Symbols | 5 |
| 1. Motivation | 8 |
| 2. Fundamentals | 12 |
| 2.1. Manufacturing review | 12 |
| 2.1.1. Selective laserbeam melting | 12 |
| 2.1.2. Laser beam welding of aluminium alloys | 14 |
| 2.2. Material science review | 18 |
| 2.2.1. Alloying elements in Scalmalloy and SilmagAl | 18 |
| 2.2.2. Influence of oxygen | 21 |
| 2.2.3. Hardening mechanisms | 22 |
| 2.3. Aluminium alloy powder characteristics | 24 |
| 2.4. Material characterisation | 28 |
| 2.4.1. Physical properties | 28 |
| 2.4.2. Mechanical properties | 30 |
| 3. Experimental Procedure | 32 |
| 3.1. Powder identification | 32 |
| 3.1.1. Flowability | 33 |
| 3.1.2. Bulk properties | 34 |
| 3.1.3. Particle morphology | 35 |
| 3.1.4. Particle size distribution and particle size | 35 |
| 3.1.5. Chemical composition | 35 |
| 3.1.6. Micro structural impurities, phases and porosity | 36 |
| 3.2. Process parameter identification | 37 |
| 3.3. Post-build temper conditions | 39 |
| 3.3.1. "As built" condition | 39 |
| 3.3.2. Heat treatment | 39 |
| 3.3.3. Hot isostatic pressing | 39 |
| 3.4. Material characterisation: physical and mechanical testing | 41 |
| 3.4.1. Microstructural response | 42 |
| 3.4.2. Density | 42 |
| 3.4.3. Corrosion analysis | 42 |
| 3.4.4. Static tensile testing | 45 |
| 3.4.5. High cycle fatigue | 46 |
| 3.4.6. Fracture mechanic testing | 47 |

Contents

| | |
|--|------------|
| 4. Results and discussion | 50 |
| 4.1. Results: powder analysis | 50 |
| 4.1.1. Results: flowability | 50 |
| 4.1.2. Results: bulk density | 53 |
| 4.1.3. Results: particle morphology | 54 |
| 4.1.4. Results: particle size distribution and particle size | 57 |
| 4.1.5. Results: chemical composition | 58 |
| 4.1.6. Results: impurities, phases and porosity | 60 |
| 4.1.7. Discussion powder analysis | 63 |
| 4.2. Results and discussion of process analysis | 67 |
| 4.2.1. Single and multi-layer weld traces of Scalmetalloy Batch I | 68 |
| 4.2.2. Influence of process parameters on porosity | 75 |
| 4.2.3. Microstructural response | 81 |
| 4.2.4. Influence of process parameter on static tensile strength | 85 |
| 4.3. Results and discussion of post process heat treatments | 90 |
| 4.4. Results and discussion of material characterisation | 96 |
| 4.4.1. Result and discussion: density | 96 |
| 4.4.2. Results and discussion: corrosion | 96 |
| 4.4.3. Result and discussion: static tensile strength | 101 |
| 4.4.4. Result and discussion: high cycle fatigue | 107 |
| 4.4.5. Result and discussion: fracture toughness | 111 |
| 4.4.6. Result and discussion: crack growth and crack growth threshold . . . | 113 |
| 4.4.7. Discussion of powder, process and material properties correlation . . | 116 |
| 5. Conclusion and Outlook | 123 |
| A. Appendix | 128 |
| A.1. Powder analysis | 128 |
| A.1.1. Particle morphology | 128 |
| A.1.2. Particle size distribution and particle size | 130 |
| A.1.3. Impurities analysis | 134 |
| A.2. Process analysis | 137 |
| A.3. Material characterisation | 138 |

Acronyms

| Abbreviation | Description |
|---------------------|---|
| 2 $\frac{1}{2}$ D | Two and a half dimensional |
| 3D | Three dimensional |
| AA | Aluminium alloys, Aluminium Association |
| AIC | Alternate immersion corrosion |
| Al | Aluminium |
| AM | Additive Manufacturing |
| AMZ | Additive manufactured zone |
| Ar | Argon |
| ASSET | Assessment of exfoliation corrosion susceptibility of 5XXX series aluminum alloys |
| ASTM | American society for testing and materials |
| BM | Basis material |
| C | Carbon |
| CAD | Computer-aided design |
| Cl | Chlorine |
| CRT | Central Research and Technology |
| CS | Constitutional supercooling |
| CT | Computer tomography |
| CT18 | Compact tension specimen with a width of W=18mm |
| CT30 | Compact tension specimen with a width of W=30mm |
| Cu | Copper |
| DIN | Deutsches Institut für Normung |
| DT | Destructive testing |
| EAC | Environmentally assisted cracking |

Acronyms

| | |
|---------|--|
| EDS | Energy dispersive X-ray spectroscopy |
| EIGA | Electrode induction-melting gas atomisation |
| EXCO | Exfoliation corrosion |
| F-AAS | Flame atomic absorption spectrometry |
| FCG | Fatigue crack growth |
| Fe | Iron |
| FG | Fine grain |
| FZ | Fusion zone |
| HAZ | Heat affected zone |
| HB | Hardness according to Brinell |
| HCF | High cycle fatigue |
| HE | Carrier gas hot extraction |
| HIP | Hot isostatic pressing |
| HV | Hardness according to Vickers |
| IC | Intergranular corrosion |
| ICP-OES | Inductively coupled plasma optical emission spectrometry |
| IGA | Inert gas atomisation |
| ISO | Internationale Organisation für Normung |
| LBW | Laser beam welding |
| LZ | Liquid zone |
| Mg | Magnesium |
| Mn | Manganese |
| MZ | Mushy zone |
| Na | Sodium |
| NaCl | Sodium chloride |
| NAMLT | Mass loss after exposure to nitric acid |
| Ni | Nitrogen |

Acronyms

| | |
|---------|--|
| non-PSE | Non-principle structural element |
| O | Oxygen |
| P | Acronym of platforms used for investigations (P1-P5) |
| PB | Powder bed |
| PMZ | Partly melted zone |
| PS | Particle size |
| PSD | Particle size distribution |
| PSE | Principle structural element |
| RP | Rapid prototyping |
| RPA | Revolution powder analyser |
| SAED | Selected area electron diffraction |
| SC | Specification conform |
| Sc | Scandium |
| SCC | Stress corrosion cracking |
| SEM | Scanning electron microscope |
| Si | Silicon |
| SLM | Selective laserbeam melting |
| ST | Static tensile strength |
| STL | Standard triangulation language |
| SZ | Solid zone |
| T6 | Temper condition - combination of annealing and age hardening; here 550°C/1h + WQ + 165°C/7h |
| TEM | Transmission electron microscopy |
| TFCG | Fatigue crack growth threshold |
| TiAl6V4 | $\alpha + \beta$ titanium alloy |
| UFG | Ultra-fine grain |
| WQ | Water quenching |

Acronyms

Zi

Tin

Zr

Zircon

Symbols

| Symbol | Unit | Description |
|-----------------|------------------|---|
| A_N | 1 | Aspect ratio |
| A | %; 1 | Elongation at failure, Absorption (of laser energy) |
| ΔK_{th} | $MPa\sqrt{m}$ | Stress intensity threshold value |
| ΔK | $MPa\sqrt{m}$ | Stress intensity factor |
| $E; I$ | $\frac{W}{cm^2}$ | Laser energy density; laser intensity |
| E_{av} | $\frac{kJ}{kg}$ | Avalanche energy |
| E | GPa | Young's modulus |
| FR_C | $\frac{s}{g}$ | Flow rate by use of a Carney Funnel |
| H | 1 | Hausner ratio |
| I_0 | $\frac{W}{cm^2}$ | Laser intensity |
| $K_{IC(intr)}$ | $MPa\sqrt{m}$ | Intrinsic critical plain strain fracture toughness for opening mode I |
| K_{IC} | $MPa\sqrt{m}$ | Critical plain strain fracture toughness for opening mode I |
| K_I | $MPa\sqrt{m}$ | Stress intensity factor for opening mode I |
| K_q | $MPa\sqrt{m}$ | Provisional plane strain fracture toughness |
| K_t | 1 | Theoretical stress concentration factor / notch factor |
| L | $\frac{W}{mK}$ | Heat conductivity |
| L_t | mm | Total length of test piece |
| N | 1 | Number of cycles |
| P_L | W | Laser power |
| Pe_{Al} | 1 | Peclet-number for aluminium |

Symbols

| | | |
|--------------------------|--------------------|--|
| Q | mm | Diameter (of test specimen) |
| $R_{p0.2}$ | MPa | Yield strength |
| R_m | MPa | Ultimate strength |
| R | 1 | Load ratio of $\frac{\sigma_{min}}{\sigma_{max}}$, Reflection (of laser energy) |
| σ_0 | MPa | Peierls stress |
| $Span$ | 1 | Particle size distribution range |
| T_E | °C | Eutectic temperature |
| T_L | °C | Liquidus temperature |
| T_S | °C | Solidus temperature |
| T_V | °C | Evaporation temperature |
| T | 1; °C | Transmission (of laser energy), temperature |
| V | cm^3 | Volume |
| Z | % | Reduction of area |
| α_P | ° | Avalanche angle |
| a | 1 | Filling factor |
| $d_{10}; d_{50}; d_{90}$ | μm | 10%, 50%, 90% percentile of the particle size distribution |
| d_d | μm | Weld seam depth |
| d_f | μm | Laser focus diameter |
| d_w | μm | Weld seam width |
| $\frac{da}{dN}$ | $\frac{mm}{cycle}$ | Fatigue crack growth rate |
| d_g | μm | Grain diameter |
| $\frac{d\sigma}{dT}$ | 1 | Surface tension gradient |
| d^* | μm | Layer shrinkage |
| d_w | μm | Weld seam width |
| d | μm | True layer thickness |

Symbols

| | | |
|-------------|----------------------|-----------------------------|
| h | μm | Hatch distance |
| k_y | $\text{MPa}\sqrt{m}$ | Strengthening coefficient |
| m | g | Mass |
| n | 1 | Number of layers |
| ψ_P | 1 | Surface fractal |
| ρ_{ac} | $\frac{g}{cm^3}$ | Apparent density |
| ρ_T | $\frac{g}{cm^3}$ | Tap density |
| ρ | $\frac{g}{cm^3}$ | Density |
| t | s | Time |
| v_s | $\frac{mm}{s}$ | Welding (scan) velocity |
| xyz | [-] | Coordinates |
| z | μm | Lowering of the build plate |

1. Motivation

Since the 1980s, manufacturing methods named Rapid Prototyping were developed and available for quick delivery of prototypes. Rapid prototyping became a synonym for numerous of techniques which all have in common, that on the basis of a three-dimensional (3D) model, a real part is manufactured additively, layer by layer. The feedstock can be powder, wire, sheets or liquids. All methods were initially intended to be used only for prototypes, small series or tools. Thirty years later, further techniques were invented to be used for prototyping, tooling and manufacturing and since then all are named under the term of Additive Manufacturing (AM). They became a point of great attention for example in the production of aerospace parts. Additive Manufacturing offers completely new design possibilities and therefore potential weight savings. Such new manufacturing opportunities require new or adapted materials, however, and any new process, material or part needs to pass a qualification assessment for guaranteeing targeted material properties as specified by design before it can be finally approved for use in aircrafts. Commercial aircrafts are at the time using only AM parts of a Ti64, and they are qualified and designed mainly for static load cases. The reason, for this exclusivity of Ti64, is preliminary due to the absence of fundamental research in the field of Additive Manufacturing on both topics the materials and processes.

Al-alloys still play an important role in the aircraft industry. The adaption and continuous improvement of the performance of existing alloys or the development of new Al alloys is necessary to meet requirements regarding weight savings. Important for the development of Al alloys is the development of high strength properties and high plasticity, improved corrosion resistance and a damage-tolerant behaviour. The requirements on a material for structural components in aircrafts are reasonably high.

Al-alloys containing scandium (Sc) and zircon (Zr) show remarkable performance and are hence key elements in Al alloy development at Airbus Central Research and Technology (CRT). This material is called "Scalmalloy[®]". Scandium is a rather expensive alloying element, as it is generally considered a rare earth element. An alternative, low-cost Al material is SilmagAl, which is based on already aircraft-qualified Al cast alloys and contains silicon (Si) and magnesium (Mg). SilmagAl lacks strength compared to Scalmalloy, but its feedstock is for now considerably cheaper. Both, Scalmalloy[®] and SilmagAl[®], are registered trademarks, but for sake of readability, in this thesis the trademark symbol [®] is omitted throughout.

Selective Laser Melting (SLM) processes are so far generally considered as AM technique with the greatest potential for serial production. The functional principle of this technique is quite simple. A CAD model of a part is sliced into several layers and these layers are additively welded by a laser in a powder bed chamber in an inert gas atmosphere (see Figure

1. Motivation

1.1). As such, a three dimensional (3D) part is manufactured in multiple two-and-a-half dimensional steps. The process chain, starting with a CAD-Model and finishing with the final part, remained for aluminium so far in important steps at a low maturity level.



Figure 1.1.: SLM process on a SLM 125HL platform

This thesis aims to increase the maturity level of the Al alloys Scalmlalloy and SilmagAl in SLM systems for the time-consuming aerospace qualification. The process chain is adapted to these materials, and the necessity of adjustment of qualification standards according to the process is discussed.

Investigations into Scalmlalloy started in 2009 within the German-funded project AluGenerativ [1], where initial trials showed the potential of this material. Deeper investigations on the material behaviour of AM Scalmlalloy followed in the EU-funded project Coalsece² [2] one year later. At that time, SLM systems of only limited laser power ($P_L = 200\text{W}$) and with small build chambers were available. This limitation led to build rates not suitable for commercial use. An internally funded Airbus CRT project called "Scalmlalloy Nursery" allowed the continuation of this research regarding evaluation of possible powder atomisation techniques and modification of process parameters to improve the low build rates. The success of these studies led, finally, to commercial sales of Scalmlalloy powder and parts by the Airbus spin-off Apworks [3]. Since the first paper on Scalmlalloy research in [4] was published, several institutes have started their own research, each under support of Airbus CRT by providing powder [5, 6, 7] or AM Scalmlalloy parts produced during this study [8].

Alongside increasing attention to Scalmlalloy, enquiry into low-cost Al-alloys also increased. So far, the established Al-alloys for SLM systems are AlSi12 or AlSi10Mg. However, both alloys only offer high ductility at low yield-strength levels. SilmagAl belongs to the same AlSi(Mg) material class, but a processing route was identified by which SilmagAl can achieve a moderate strength level and still moderate elongation at failure. Another important advantage of processing SilmagAl is that at a higher build rate a higher process stability is realised than for Scalmlalloy. The insights gained during the development of Scalmlalloy at CRT allowed a fairly fast development of the alternative alloy SilmagAl for SLM.

The unique material properties of Scalmlalloy are not yet fully investigated or understood. Microstructural analysis is only partially available [9, 4, 10, 5, 6, 7, 8] and reveals a structure of alternating ultra-fine grain (UFG) and fine grain (FG) bands. However, the microstructure of AM AlSi(Mg) alloys has already been described in the literature, for example in [11, 12, 13]. Still, a correlation between powder characteristics, process stability, microstructural response and material behaviour remains absent for both.

1. Motivation

The process chain for Scalmalloy and SilmagAl SLM processes can be clustered in different steps [14], as illustrated in Figure 1.2. Step 1 covers the definition of the part. A 3D model of the part must be available to start the process. This 3D CAD model is geometrically optimised to take advantage of the high geometrical freedom the process offers, on the one hand, and to determine its limits, on the other hand. Design guidelines for AM of Ti64 are comprehensively described in [15]. However, guidelines for processing Al-alloys in SLM systems are not extensively available in the literature at the moment. The final 3D CAD model is converted into a *.stl (standard triangulation language) model.

Special AM software is necessary for step 2, where the preparation of the part for the manufacturing process takes place. AM of metals requires a platform upon which the part is built. At this stage the part is orientated and placed on the platform in the build chamber; it gets support structures where necessary and is sliced and hatched into multiple layers of a predefined thickness. Other process parameters like laser power, scan speed, hatch distance and others are also recorded in this step. The final format of the generated file for manufacturing depends on the chosen machine and varies in the following investigations between *.SLI (EOS), *.SLM (SLM) or *.CLS (Concept Laser). Build envelopes have increased significantly in recent years. Prominent machine manufacturers that presently offer large build chambers for metals are as follows: SLM Solutions Group AG [16], EOS Electro Optical Systems GmbH [17], Concept Laser GmbH (part of GE Additive) [18] or Matsuura [19].

Step 3 describes the powder as raw material, and each Al powder must be analysed and described in its full complexity. In most analyses, it is characterised only partly, but the powder has to be specified precisely if a stable and reproducible manufacturing process is to be established. Additionally, regular quality checks are necessary to confirm whether each used powder batch meets the specifications. The manufacturing of the part follows in Step 4. A stable process parameter set (defined in Step 2) ensures equal and uniform creation of the part. As Al has a high affinity to oxygen, a closed powder handling practice is recommended during the building process.

After the part is built, heat treatment follows in Step 5. According to the final requirements of the given part, different heat treatment possibilities exist for Scalmalloy and SilmagAl. The next Step 6 is about surface treatment of both Al alloys. The requirements in aerospace industry do not presently allow the use of AM-Al parts without suitable surface conditioning. Surface finishing may vary from polishing or peening processes to reduce roughness as much as possible to mechanical milling of interfaces. Coating is currently additionally essential for Al alloys in airplanes to ensure the surface and corrosion protection. Both post process steps (the heat and surface treatment) can be time consuming and expensive, dependent on the final application.

Step 7 concerns quality control. In situ process control techniques for now do not have the maturity to be used reliably for Al alloys. Therefore established non-destructive testing (NDT) methods, based on radiography, need to be adapted and used for the detection of process-related defects. For destructive testing (DT), witness samples are the means of choice to confirm that the targeted material-quality is achieved. Only a qualified approach of each step results in a high-quality AM-Al part in Step 8 which fulfills the necessary material specification.

1. Motivation

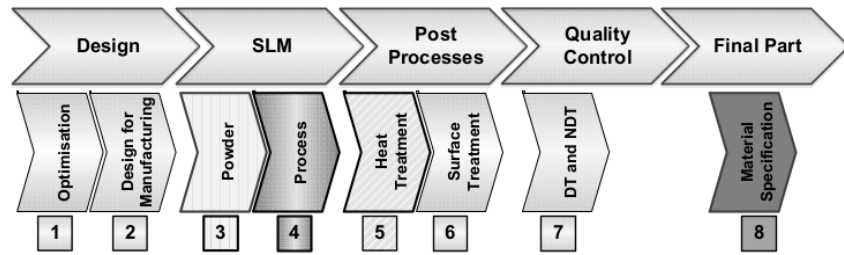


Figure 1.2.: SLM process chain for Al-alloys Scalmalloy and SilmagAl

The investigations of this thesis deepen the scholarly understanding of processing Scalmalloy and SilmagAl in SLM systems. The interaction of Steps 3 (powder), 4 (build process), 5 (heat treatment and material response) are described, analysed and discussed with regard to the feasibility of both materials for aerospace applications. A full discussion of all steps in an appropriate manner lies beyond the scope of this thesis.

2. Fundamentals

2.1. Manufacturing review

Additive Manufacturing covers a number of manufacturing techniques by which material is added layerwise to a final 3D part without any mechanical tools. Various metal and polymer based materials can be used, in most different shapes. It is in general distinguished between material and functional principle. Material feedstock come in various forms and are available either as wires, powders, sheets or liquids. The functional or baseline descriptions cover the process, whether laser or electron beam, printer technologies or others are used. Many summaries and descriptions of the classification of AM technologies in the form of standards [20, 21], guidelines [22] or books [23, 14] are available.

2.1.1. Selective laserbeam melting

The functional principle of SLM corresponds to fusion welding, especially laserbeam welding (LBW), further considered in subsequent sections. A schematic drawing in Figure 2.1 illustrates the most important SLM process steps. The first powder layer is wiped onto a platform by a machine specific recoater device. The powder layer height of the first layer corresponds to the lowering of the build plate z (often erroneously described as "layer thickness"). A scanner controlled laserbeam exposes then the pattern of the part with defined scan and process parameters. Fusion of this powder layer results in shrinkage d^* which is depended on the apparent density of the powder. The next lowering of the build plate results in a volume increase of the now applied powder compared to the first layer.

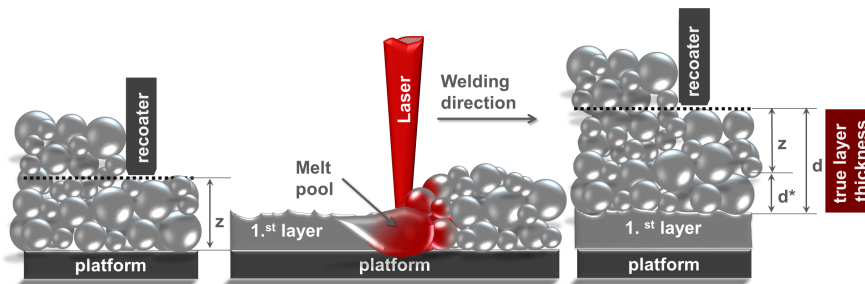


Figure 2.1.: Schematic drawing of SLM process steps

The induced laser energy leads to interdependencies with powder and bulk material and is, according to energy conservation divided into transmission T , reflection R and absorption A

2. Fundamentals

[24].

$$T + R + A = 1 \quad (2.1)$$

Meiners determined experimentally in [25] the proportion of T , R and A for Al powders. As result it was observed that the absorption A is about 45 %, reflection R about 54 % and transmission T only about 1 %. It was further determined that the absorption A in a powder layer is significantly higher than A on the surface of the same material as solid. This occurs mainly because multiple reflection, beam traps and heat increase in the bulk material are leading to a local absorption of nearly 100 %, as shown in Figure 2.2.

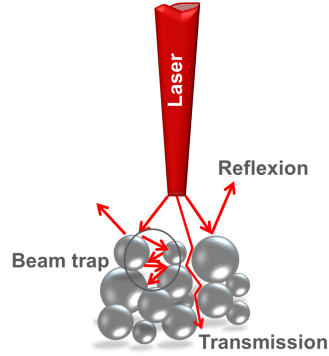


Figure 2.2.: Laser beam propagation in a powder layer according to [25], [24] and [26]

The heat transfer is furthermore divided into radiation, convection and conduction, [24, 27, 28]. Important for parameter definition is heat input by conduction. The goal is to ensure a stable heat transfer that welding in a constant welding mode can be maintained.

The basic parameters for the desired study of each new material are, according to [25, 29], the volume energy density E_V calculated by use of laser power, scan velocity, hatch distance and layer thickness. The parameters are illustrated in Figure 2.3. It is assumed that the energy density defines precisely how fast a certain amount of energy is applied. It is furthermore assumed that a certain E_V range describes a suitable parameter window and that process instabilities resulting in defects or pores occur the higher the deviation from the ideal E_V is.

In general, a complete fusion of the powder layers and the solid material is not achieved if the applied energy density is too low. Resulting porosity is called lack of fusion. Is the energy density on the other side too high, deep penetration welding can occur and the resulting keyhole formation with its metal vapour that develops around this keyhole are destabilising the process.

In both scenarios, the so called balling effect occurs; balling describes the creation of spheres during the process. Different mechanisms drive this phenomenon. On the one hand, it occurs due to low energies which cause only a limited liquid formation [30, 28]. The viscosity of the melt increases and leads to high surface tension, and this tension again leads to early melt solidification by forming spheres. Hence is a continuous formation of each weld path and a homogenous fusion with layer(s) underneath impossible. On the other hand, balling describes

2. Fundamentals

also the spattering and the formation of spheres with a size up to several hundred microns, if too much energy is used. This happens if the weld pool dynamic gets too high or if the keyhole breaks during welding.

$$E_V = \frac{P_L}{d \cdot h \cdot v_s} \quad (2.2)$$

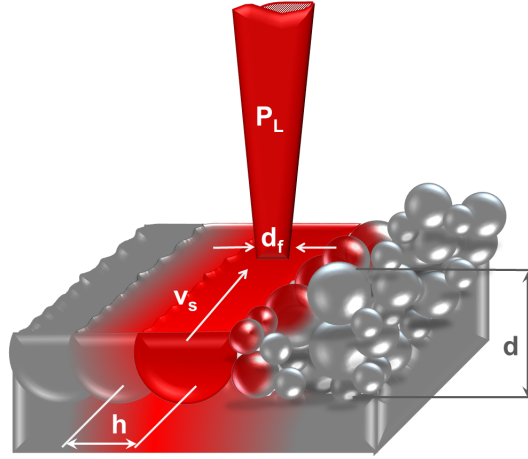


Figure 2.3.: Influencing process parameters for SLM

2.1.2. Laser beam welding of aluminium alloys

LBW is a welding technique that joins metals by use of a laserbeam as heating source which is commonly produced by either gas or solid-state lasers. Different configurations of optical devices focus the beam to allow high welding rates at high quality welds. Laser beam welding of aluminium alloys in aerospace was established in 2000, driven by the increasing demand of a cost- and weight-saving joining alternative to riveting. The main challenges of qualifying LBW for aerospace applications were related to process stability and process quality. In 1996, Rapp discussed [31] basic fundamentals and influencing parameters for LBW of Al materials in light-weight applications. Klassen [32] described weld pool dynamics for Al leading to weld imperfections due to changes in laser power, focus geometry and focus position. Schinzel [33] investigated LBW of Al-alloys with Nd:YAG lasers for automotive industries. Heimerdinger [34] analysed the influence of different process parameters on the weld quality and hot crack resistance for different Al-alloy compositions. He showed that with an increase of the ratio of laser power to focus diameter P_L/d_f (called specific power in [31]), the amount of process pores decreases.

The functional principle of SLM corresponds to conventional LBW with powder as filler material. Only the basic fundamentals of LBW that are transferable to SLM are explained in this Section. Figure 2.4 illustrates three types of welding modes that can occur in SLM. It shows graphically the differentiation between heat conduction welding, transition keyhole welding and keyhole/ deep penetration welding, which differ in their weld aspect ratio A_N of weld seam

2. Fundamentals

depth to weld seam width (see Equation 2.3) and the intensity of metal vapour formation, as indicated by the yellow or red cloud around the laser beam.

$$A_N = \frac{d_d}{d_w} \quad (2.3)$$

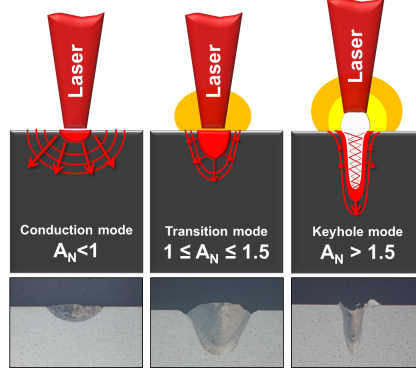


Figure 2.4.: Laser welding modes and aspect ratios according to [35]

The melt pool during heat conduction welding stays intact, and welding is only affected by the absorption capability of the material's surface (Fresnel absorption). In the keyhole welding or deep penetration welding mode is the degree of energy coupling the more dominant factor. The melt pool forms depending on the evaporation temperature of the alloying elements at high power densities rapidly a vapor capillary, the so called keyhole. The vapor is surrounded by the melt, which solidifies at the vapor's reverse side. Multiple laser reflections are the result, leading to higher local absorption. In the literature [36, 34, 33, 37, 35], the different modes are often ranged depending on the power density. Heimerdinger [34] ranges heat conductivity welding between laser intensities of $I_0 = E = 10^4 \text{ W/cm}^2$ to 10^5 W/cm^2 and keyhole welding above an intensity $I_0 = E > 10^6 \text{ W/cm}^2$. According to Birnesser in [37] keyhole welding occurs already at several 10^5 W/cm^2 and at an aspect ratio of $A > 2$. Experiments in this thesis showed that in SLM processes a classification of the laser intensity and associated welding mode is even more complex as many more interference factors appear that change locally the ratio in the energy conservation of reflection, absorption and transmission (see Equation 2.1). Beck [38] has described that the ratio of laser power to laser beam diameter ($\frac{P_L}{d_f}$) reflects the threshold conditions between heat conductivity to keyhole welding for Al-alloys. Heimerdinger proofed in [34] that this approach is valid for welding velocities between 1.5 to 31 m/min. Equation 2.4 presents this simplified approach which is also taken into account for the evaluation of the SLM process (see in Section 3.2). It includes the absorption capability A , the welding (scan) velocity v_s and material-dependent factors.

$$\frac{P_L}{d_f} \sim \frac{T_v \cdot L}{A} \sqrt{Pe_{Al} + 1} \quad (2.4)$$

2. Fundamentals

The dynamics of weld pools with a free surface are essentially influenced by convective flows because of different temperature and surface tension gradients in the weld, so called Marangoni convection, (see [39, 40, 31]). The velocity of the Marangoni convection flow is in the range of several meters per second and is therefore significantly higher than the scanning velocity v_s . The Marangoni convection flow for metal alloys usually occurs due to negative surface tension gradients $\frac{d\sigma}{dT} < 0$ [40], as illustrated in Figure 2.5. Complex melt movements in SLM processes are simulated and described for AM Scalmetalloy in the literature [7].

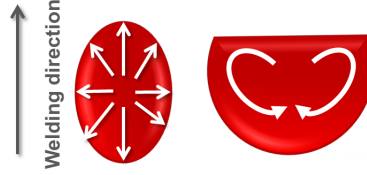


Figure 2.5.: Schematic drawing of Marangoni convection for $\frac{d\sigma}{dT} < 0$

The weld pool width d_w is depending mainly on laser focus diameter d_f and the resulting weld depth d_d is strongly dependent on the chosen scan velocity, as investigated in this thesis. The weld seam volume is very small compared to the volume of the platform, at least for the first layer in the process. The heat can therefore be transferred rapidly to the cooler platform (similar heat transfer as for laser remelting, as explained in [40]). Cooling rates between $(10^4 - 10^6)K/s$ are reported in literature, depending on SLM process parameters and alloy-dependent thermophysical properties. However, the geometry of the part and an increasing number of layers decreases the cooling rate and changes solidification processes.

During solidification of a weld, the solid and liquid interfaces play an important role and decide about the resulting solidification mode. Different zones exist in weld beads, which are in general distinguished as liquid zone (LZ), mushy zone (MZ) and partly melted zone (PMZ) (where liquid and solid coexist) and solid zone (SZ). Transferred to SLM processing, the (SZ) equals to the base material or plate (BM) or the additive manufactured zone (AMZ), which contains previous molten layers.

The solidification of an Al alloy weld follows constitutional supercooling (CS) as the weld exists for only a short time in liquid form, so convection or diffusion compensation at the solidification interface is avoided (see [40, 41]). Constitutional supercooling means that crystallisation is delayed and that the melt remains liquid although the actual temperature of the melt is below the liquidus temperature.

In general, it can be assumed that for Al-alloys, solidification during welding at high cooling rates occurs in two ways according to [42], and can be heterogeneous (columnar) dendritically at the solid interface or homogeneous equiaxed (dendritically) in the liquid weld pool. However, with increasing CS rises also equiaxed grain growth on a solid interface in the MZ as described in [41].

2. Fundamentals

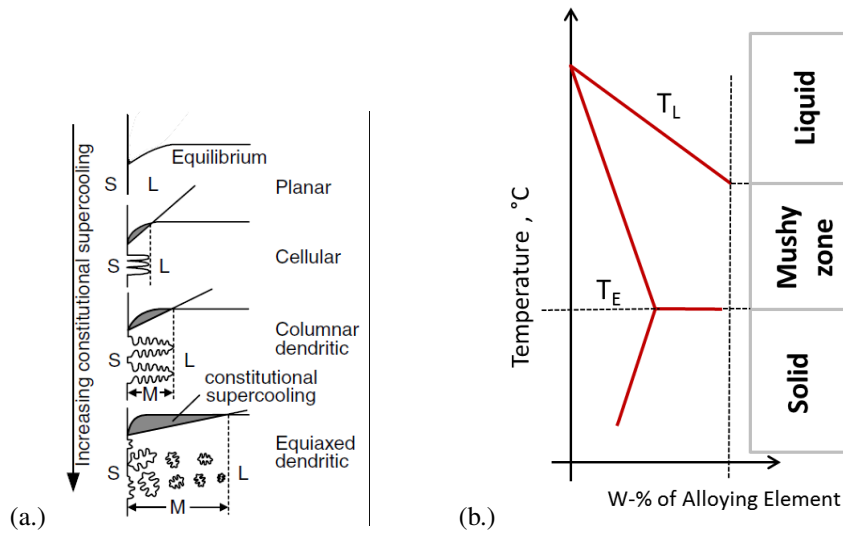


Figure 2.6.: (a.) Increasing constitutional supercooling (CS) leading to different grain growth mechanism in mushy zone (MZ) (b.) Solid zone (SZ), mushy zone (MZ), and liquid zone (LZ) in a general phase diagram; both illustrations according to [42] [39]

2.2. Material science review

2.2.1. Alloying elements in Scalmalloy and SilmagAl

The first Al-Sc alloy was filed in 1968 and finally patented already in 1971 by L.A. Willey [43]. This patent increased scientific interest all over the world, especially in Russia, where since then Al-alloys containing Sc, Zr, Mg and Mn have been extensively investigated. Scalmalloy is an Al-alloy based on non-heat treatable 5xxx series alloys, offering good welding characteristics, solid solution hardening and an improved corrosion resistance (if long-term exposure to elevated temperatures is avoided) but only limited strength [4]. Scalmalloy is to tailor 5xxx Al alloys by an addition of Sc and Zr to an age hardenable alloy of a high strength level for use in SLM processes.

However, SilmagAl material development is based on the composition of 42xxx Al-alloys containing silicon (Si) as principal alloying element and offer an intermediate strength level at low costs. Because of their excellent casting properties, 42xxx Al-alloys are widely used in the automotive industry, for example in high pressure die casting of cylinder heads or engine blocks [44].

The influence of Mg, Mn and Si as main alloying elements and of Sc and Zr as special alloying elements are described below.

- Magnesium (Mg)

The Mg content in Al generally correlates to the tensile yield strength ($R_{p0.2}$) and tensile strength (R_m) directly; the higher the Mg content the higher both $R_{p0.2}$ and R_m , but the elongation at fracture (A) decreases between 2 wt.-% Mg [45] and 3 wt.-% Mg [46] and increases slightly again. 5000-series Al-alloys like EN-AW-5083 and EN-AW-5086 contain a high content of Mg (> 3 wt.-%) and are widely used as rolled plate material for maritime applications like ship building. Al-Mg-alloys generally age soften immediately after cold work at room temperature. To achieve the well known high corrosion resistance of EN-AW-5083 or EN-AW-5086 special thermal treatments like H116 and H321 have been developed to reach and keep a stable condition.

The solubility of Mg decreases significantly with decreasing temperature and only 0.2 wt.-% Mg are soluble at room temperature in α solid solution [47], whereas the remaining Mg stays in the microstructure as β -phase (Al_8Mg_5 , see also Figure 2.7). That is technically important, as especially after sensitisation at elevated temperatures ($\approx 50 - 150^\circ C$) and extended exposure, the β phase diffuses preferentially to grain boundaries [48] and may form continuous chains [46]. This diffusion increases intergranular corrosion and stress corrosion cracking susceptibility significantly, as the β phase is anodic relative to the Al matrix [48, 49, 50]. Mg as an alloying element has a significant effect on the phase transformation in an Al-Sc system. [51]

2. Fundamentals

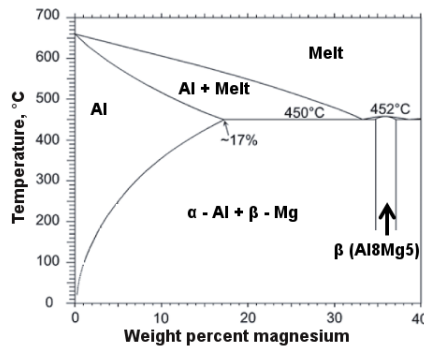


Figure 2.7.: Partial binary Al-Mg phase diagram (according to Mondolfo in [46, 45])

- Silicon (Si)

Most widely used AlSi alloys are of hypoeutectic composition, with an Si content between 5 to 12 wt.-% (see Figure 2.8). Silicon is responsible for the outstanding castability of these alloys which implies a solidification without issues because of hot cracking or shrinkage as the volume of Si increases during solidification and counteracts the shrinkage of Al [47]. Silicon additions to Al lower the melting point and simultaneously increase fluidity [52]. The solubility of Si at room temperature is almost zero and about 1.65 % at 577 °C. The microstructure of AlSi changes with decreasing cooling rates from a homogeneously distributed fine eutectic to a microstructure containing Silicon (Si) particles of different shape, size and distribution. An undercooling can be reached by addition of grain refining elements which leads to a different eutectic mixture and hence fine, soft edged Si particles, resulting in an increase of strength and ductility level [46].

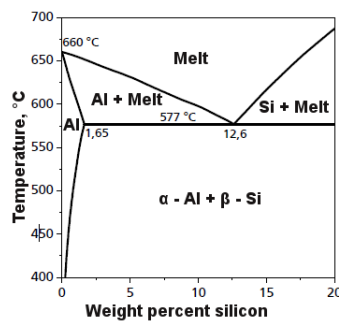


Figure 2.8.: Partial binary Al-Si phase diagram (according to Mondolfo in [46, 45])

2. Fundamentals

- Manganese (Mn)

The addition of Mn as dispersoid-forming element to AlMg alloys improves corrosion resistance and increases both strength and fatigue-resistance [46, 47]. Manganese also has only a limited solubility in α solid solution of max. 1.8 wt.-% which decreases also significantly with decreasing temperature and is negligible at room temperature. The evolution of the secondary AlMn_6 phase depends, thus, on solidification rate and the subsequent annealing temperature.

- Scandium (Sc)

Scandium is meanwhile well known for its potential to cause grain refinement and hence to improve mechanical material behaviour [53, 51, 54, 47, 55, 56]. With conventional manufacturing processes, for example casting, only a very limited Sc content of less than 0.3 wt.-% can be dissolved in Al-alloys. A supersaturated solid solution with a Sc content > 1 wt.-% can be reached according to [51] theoretically by increasing the cooling rates during solidification to at least $10^5 \frac{\text{K}}{\text{s}}$ but this level of cooling requires new improved manufacturing methods like SLM. The influential effects are based on the formation of the Al_3Sc phase. The Al_3Sc phase acts on the one hand as nuclei causing grain refinement during (eutectic) crystallization of melt of a hypereutectic alloy [57], which means precisely the more nuclei the finer the microstructure [47]. On the other hand, an additional heat treatment causes the decomposition of a supersaturated solid solution with segregation of secondary Al_3Sc particles [57]. These fine, highly and very densely dispersed precipitations are fully coherent with the Al matrix over a wide temperature range [57], as long as they are very small. The main challenge to any manufacturing and heat treatment process is to keep these precipitations small and avoid growing or coarsening and to suppress any premature precipitation of Al_3Sc .

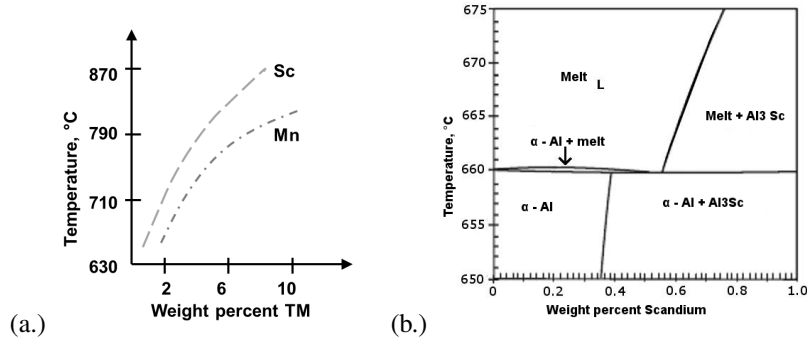


Figure 2.9.: (a.) Solubility of scandium (Sc) and magnesium (Mg) in liquid aluminium (Al) [51]; (b.) Partial binary Al-Sc phase diagram (both according to [58, 54, 51])

2. Fundamentals

- Zircon (Zr)

The solubility of Zr is reported differently and varies between 0.7 and 1 wt.-% at 660 °C [59]; nevertheless most studies agree that Zr is in general soluble in the Al_3Sc phase. Zircon is, exactly like Sc, well known for causing grain refinement [53], as Al_3Zr dispersoids can act as nuclei for uniform and fine-grained solidification. In early investigations of binary Al-Sc systems, it has been found that adding Zr is of great benefit, as it slows down coarsening of Al_3Sc precipitates [51] and stabilizes the precipitates' morphology [60]. The Al_3Zr phase can produce different structures and varies from incoherent to fully coherent within the Al solid solution [59]. Zircon forms in the Al_3Sc phase a $\text{Al}_3(\text{Zr}_x\text{Sc}_{1-x})$ phase which has even a higher coherency with Al than that of AlSc_3 [61], and Sc can even partly be replaced by Zr, resulting in the same fine microstructure. Tolley [62], Fuller [56] and Ramdmilovic [63] have described, for example, the segregation of Zr on Al_3Sc particles by forming a thin shell during ageing at 450 °C.

Scandium, Zr and Mn are also known for being transition elements which can increase the recrystallisation temperature significantly after thermo-mechanical processing. Dispersoids like Al_3Sc , Al_3Zr and AlMn_6 are thermally stable and remain insoluble at high temperatures [47]. This special characteristic is mentioned only for the sake of completeness, as recrystallisation necessarily requires a precedent recognisable plastic deformation which does not occur in any step of the SLM process chain.

2.2.2. Influence of oxygen

Aluminium and Mg as very un-noble elements have a high oxygen affinity, leading to a vast formation of insoluble oxides and a tough oxide layer in and on its melt, which can harm the products [64]. Al oxides Al_2O_3 have a melting point at 2072 °C and a higher density than Al, at around $3.75 - 3.95 \text{ g/cm}^3$. As Scalmalloy is containing a significant amount of Mg, additionally to Al_2O_3 , MgO will develop during SLM (even faster than Al_2O_3), hence contains Scalmalloy always a mixture of both oxides.

The oxygen content in an Al alloy influences significantly the mechanical and physical material properties. The strength level may increase with increasing Al_2O_3 content, but at the expense of ductility, which decreases as oxides act as impurities that suppress a highly ductile fracture. The same applies for corrosion behavior of Al alloys. The corrosion resistance decreases as impurities in the form of oxides will create weak points where corrosion might start.

In general, any Al-joining technique needs to consider and deal with possible surface oxide layers. In SLM processes, there are roughly two possible methods of oxide formation; during atomisation on the powder particles surface and during the SLM process itself on each weld path as there is always a remaining oxygen level of up to 2000ppm in the machine build chamber during processing. Quality limits on allowable oxygen impurities for Al castings are given, for example, in [47]. But if the same acceptance criteria are transferable and practicable in AM Al-alloys is not discussed in literature so far.

Powder particles are surrounded by an oxide layer [65] and the surface of weld traces might be covered by a thin oxide layer due to the remaining oxygen level in the powder bed fusion

2. Fundamentals

build chamber. These layers are in both cases potentially not of equal thickness and will influence the welding and melting process, and hence the final microstructure. The aim is to disrupt these layers and to stir them (equally, in the best case) into the microstructure to avoid joining defects which prevent a diffusion bonding, such as so called kissing bonds. In [66], it is assumed that oxides will partially vaporise during the SLM process. Louvis et al. [67] have investigated the resulting fumes when processing AA6061 by SLM, and they found predominately Mg and oxide clusters, which are assumed to be either vaporised and oxidised metal, vaporised oxides from powder particles or vaporised oxides from the surface of the melt pool. Due to the low Mg content in AA6061, it was concluded that the last option is most probable. However, Al oxides have an evaporation temperature of around 3000 °C and for Scalmalloy and SilmagAl, it is consequently assumed that the first option (vaporised and oxidised metal) is most likely, as aluminium and low-melting alloying elements like Mg evaporate earlier than the oxides.

In sum, the contamination of Al with oxygen in both steps, either powder production or SLM processes, needs to be limited to the lowest possible level to achieve high quality in AM material.

2.2.3. Hardening mechanisms

For any hardening mechanism in Al in general, it is essential to impede dislocation movements [68] through different dislocation barriers. The following three main hardening mechanisms occur in different intensities in Scalmalloy and SilmagAl.

- Solid solution hardening in Al is the effect of adding atoms of the alloying element(s) to the crystalline lattice of aluminium. These atoms go into a solid solution in the single-phase region of the corresponding phase diagram and distort the Al lattice. The resultant local non-uniformities in the lattice produce restricted dislocation movements and hence a hardening effect.
- Precipitation hardening relies on the precipitation of finely dispersed phases that act as effective barriers against dislocation slip. Rapid quenching after solution heat treatments leads to a supersaturated single α -phase microstructure, that forms the desired precipitates during the subsequent ageing treatment. Also rapid solidification of a melt can lead to phase supersaturation. SLM processes generate high cooling rates during solidification of the melt and can thus promote phase supersaturation. For example, in [51], different structural states of binary AlSc and AlZr systems are dependent on the cooling rates given. An additional heat treatment is now necessary to activate the growth of the embedded nuclei and to create the secondary precipitation phase. Only if the precipitates are fully coherently embedded in the Al matrix does peak precipitation strengthening occur. These precipitations impede also dislocation movements by acting as barriers and may increase hardness and strength levels significantly. Precipitation hardening is therefore most relevantly affected by the time and temperature of the heat treatment and the resulting precipitation morphology, size, content and distribution. Possible precipitations formed during annealing in a temperature range of 250 - 400 °C in Scalmalloy are Al₃Sc, Al₃(Zr_xSc_{1-x}), Al₆Mn, Al₃Mg₂ and Al₈Mg₅. The important

2. Fundamentals

precipitation phase that occurs in SilmagAl is Mg_2Si . Aside from these target phases, which are strength relevant, other primary phases, like $AlFeMn(Si)$, may exist due to contaminations of iron (Fe) and Si in Scalloy and Fe and Mn in SilmagAl. In Scalloy, there is also the possibility of Mg_2Si phases, due to the high Mg content and undesired Si contaminations.

- Grain size hardening pertains to the effect grain sizes have in impeding dislocation movements. The grain boundaries act as barriers for dislocation movements, as a dislocation is forced to change its slip direction from one grain orientation into another, differently orientated grain. The dislocations may also be positioned closer together, and movements may be hindered as they are interacting with each other [69]. That means that a decrease in grain size results in a higher strengthening effect without decreasing the material's ductility. Grain size hardening can be calculated by the Hall-Petch relationship [47] (see Equation 2.5).

$$R_{P02} = \sigma_0 + \frac{k_y}{\sqrt{d_g}} \quad (2.5)$$

Toropova et al. showed in [51] that the grain size depends on Sc or Zr content and the cooling rate. Increasing Zr content up to 0.8 wt.-% leads to significant grain-size reduction and a resulting grain size below $100 \mu m$, which can then only further be decreased by increasing cooling rates. The highest grain-size reduction efficiency for Sc is according to the published diagrams in [51] obtained for (0.8 - 1) wt.-% Sc at high cooling rates.

2.3. Aluminium alloy powder characteristics

Powder is the feedstock of powder bed fusion processes. The powder's characteristics have a significant effect on the quality of the parts. Each powder layer is applied to a build platform by a machine-dependent recoater device. The lowering of the build plate ranges at the time being from 20 - 90 μm for Al-alloys and, depending on the apparent density of a powder, results in powder layers between 30 - 150 μm . Uniform deposition of each layer is a necessary condition for a homogeneous build-up of the part. That is, the chosen Al powder needs to meet not only metallurgical requirements but must also display a wide range of physical characteristics.

The way in which an Al powder is manufactured correlates strongly with its physical and metallurgical properties. Characteristics such as morphology and flow rate are closely related to the chosen production method for the powder. For use in SLM processes, Al powders atomised in a gas atmosphere are most often considered, as this is the dominant technology for producing Al powders [65]. Other commercial Al powder atomisation processes used in production are the water, centrifugal, ultrasonic and soluble gas methods [65]. However, these methods play so far a minor role in Al alloy powder production in AM.

In gas atomisation, a liquid metal is nebulised by a gas jet; either gas or air can be used as the atomising medium. For AM Al powder, current methods require the use of either nitrogen (N) or argon (Ar), although Ar is used less often because of its higher price. Air atomisation of Al results in irregular nodular particle shapes and oxygen contamination and is hence not used for AM Al powders. But occasionally, a certain content of air is added to the chosen inert gas to generate even during atomisation a passivation layer on the particle's surface. Many different gas jet configurations are used to produce powder. Common nozzle designs, such as free fall or de Laval nozzles, are explained in the literature [65]. In addition, different methods exist of directing the molten metal stream. It can be directed either horizontally, vertically, up or down. A vertically upwards aspiration allows, for example, the production of a wide range of particles sizes. Each supplier uses its own techniques and own unique equipment, such as special designed nozzles that are most often treated strongly confidentially and not described or explained in the literature or patents.

In January 2017, DIN 65122 [70] called "Aerospace series – Powder for additive manufacturing with powder bed process – Technical delivery specification", was released. According to this standard, the most influential properties of powder for use in SLM are as follows:

- **Flowability**

The flowability of a powder can be determined in many different ways. The aim is simply to predict the ability of a powder to flow. Flow is induced by shear stresses in the powder due to its own (dead) weight or external forces. However, behind this general quite loosely defined characteristic, numerous physical properties are hidden. The intensity of interparticle (surface) forces has a significant influence on the flowability. Friction [65] or van der Waals forces [71] affect the cohesive strength and therefore the tendency to form agglomerates. Particle size, shape and surface roughness influences

2. Fundamentals

mechanical interlocking [72]. Oxide and moisture films on a particles surface also affect the flow characteristics. Friction is altered with the presence of oxide films on powder particles. Increasing oxide layers form an isolating shell and decrease interparticle van der Waals forces, leading to fast flow rates. By contrast, an increasing moisture level slows down flowability [65].

The most common flowability test methods are to measure, for example, angle of response, flow rate or Hausner ratio. Newer methods evaluate the flowability by avalanche angle and energy and surface fractal values. Macroscopic optical evaluation of the flowability or angle of response is subjective, but also a common procedure. Additionally powder flowability can be tested under shear loading.

According to DIN 65122 [70], the flow rate should be measured. A powder generally has a good flow rate if a pre-set weight flows freely and without any stimulation in a very short time through the orifice of a funnel.

• Bulk properties

Bulk density is the mass that fills a standardised cup with a certain volume [73]. If the powder is free flowing and filling the cup, the apparent density is obtained. After standardised compression by tapping the cup, the tap density is obtained. The ratio of tap and apparent density is called "Hausner ratio", and also assumed to be an indicator of the flowability of a powder.

In general, powder used for powder bed fusion has an apparent density of $\geq 45\%$. During the SLM process, the powder is molten, and a densification of each layer to ideally $> 99.95\%$, takes place. The densification causes shrinkage of the layer with the most influence in z-direction; a schematic is shown in [27]. Meiners [25] gives a detailed description of the relation between apparent density and SLM processes. The apparent density gives here the filling factor a [$0 < a < 1$]. Meiners shows that after manufacturing 6 - 10 layers, a constant true layer thickness d of $1.6z$ to $2z$ is achieved.

$$d^* = d(1 - a) \quad (2.6)$$

$$d = z + d^* \quad (2.7)$$

With an increasing number of layers ($n \rightarrow \infty$), a convergent geometric progression can be developed.

$$d_n \xrightarrow{n \rightarrow \infty} \frac{z}{a} \quad (2.8)$$

• Particle morphology

Aluminium powder particles vary from completely irregular to perfectly spheroidal. The atomisation process defines the shape of particles by variation of chosen gas, gas flow and jet configuration, pressure and cooling conditions. A description and corresponding image of each shape as well as the general description of particle, grain and agglomeration is given in DIN EN ISO 3252, or alternatively for example in [74]. It is

2. Fundamentals

differed between acicular, angular, dendritic, fibrous, flaky, granular, irregular, nodular and spheroidal shape.

Important for the application of Al powder in SLM is that only spheroidal particles enable closest packing and a smooth surface of the powder as bulk material. It is essential that the powder's reorganisation behaviour, after being applied or recoated to the build plate, allows the formation of a packing as close as possible to get a stable and reproducible powder bed fusion process.

The particle morphology can additionally be assessed by an optical analysis of the sphericity according to DIN EN ISO 9276-6.

- **Particle size distribution and particle size**

The particle size distribution measurements are important to investigate the powders range and mean particle size. This mainly influences all other powder characteristics, like flowability or bulk density and therefore also the processes ability of a powder in SLM systems. To describe particle size distribution the values, d10, d50 and d90 are used, of which d50 is the mean particle size. Half of all particles are below the d50 value, and similarly 10% are below d10 and 90% are below d90. This means d10 and d90 represent the range of the particle size distribution. The volume size distribution shows the percentage of each particle size. Another commonly used visual representation is the cumulative particle size distribution which follows approximately the log-normal law. Special attention should be paid during the PSD analysis to the susceptibility of the powder to form agglomerates or satellites that might be misinterpreted as coarser particles.

- **Chemical composition**

The alloying composition mainly determines all mechanical and physical material properties. For this reason, the investigation of the powder's chemical composition is crucial. The chemistry is defined in two ways; major constituents and impurities. Both need to follow a pre-set specification range for each element. Impurities can be of three different types, as shown in Figure 2.10. Exogenous impurities are extrinsic contaminations between powder particles, dissolved impurities are contaminations inside of powder particles and surface contaminations are oxide or moisture films [73].

2. Fundamentals

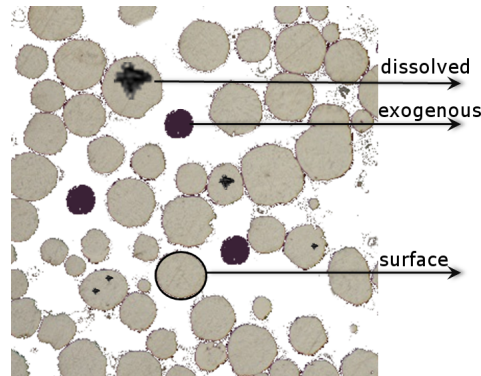


Figure 2.10.: Schematic drawing of possible impurities in powder

- **Impurities, phases and porosity**

Ideally alloyed homogenous powder particles are metallurgically desirable. However, all gas atomised Al alloys still show certain deviations from this ideal. It is therefore essential to evaluate these deviations.

Although impurities are quantitatively already revealed by chemical analysis, it remains necessary to analyse their type, distribution, size and shape. Only a microsectional analysis can reveal the powder particle's inner structure and composition. As Al has a high affinity for oxygen, it is assumed that impurities in the form of oxides, oxide layers and porosity occur on or in powder particles. Porosity can vary between intra-porosity or internal voids. Other impurities in the form of undesired phases or early precipitations can occur due to an insufficient melting or atomisation process.

Flowability and bulk density are both dependent on several variables as particle size, particle size distribution, particle shape, particle's cohesiveness, interparticle friction, and particles surface roughness, moisture and oxygen content. It is assumed that only the analysis of all characteristics allows a derivation of a powder specification for Scalmalloy and Scalmalloy.

2.4. Material characterisation

The basis for every material decision of every design engineer is a thorough knowledge of its performance and its failure behaviour. To create an aerospace material or process specification means, that a wide range of mechanical and physical material properties have to be investigated. The existence of influencing characteristics in parts even before service begins is normally assumed in aerospace engineering. These characteristics are varied, including inclusions, pores or small cracks, and they occur due to various reasons, either during the manufacturing process itself or in the assembly. A part can be designed under the assumption that the crack does not exceed a critical length during a predefined life cycle. This design principle is called "damage tolerance". A damage tolerance evaluation uses fracture-mechanics methods and values. Therefore applied loads depend on the requirements for the part and can vary from static, cyclic or creep loads, even in corrosive environments. Only a sample of typical material investigations is shown in this thesis for Scalmalloy and SilmagAl but it concentrates on the most representative properties. The characterisation of new Al alloys and their performance requires an evaluation of failure resulting from both static and variable loadings. Many mechanical investigations must be performed to get an appropriate prediction of the overall material behaviour. The validation is essential to see whether high requirements can be met to become an allowable material for structural or non-structural aerospace parts.

2.4.1. Physical properties

A fundamental characteristic value is the density. The density ρ is by definition the mass per unit volume, here $\frac{g}{cm^3}$. Aluminium alloys have a very low density of around $\rho \approx 2.7 \frac{g}{cm^3}$ and are therefore considered light weight or light metal. As such Al, along with its alloys, is the second most widely used metal in the world [75].

Corrosion means in general the destructive (electro-) chemical reaction of a material in interaction with an environment, which result in changes in the materials properties (see DIN EN ISO 8044 [76]). Pure Al has a high corrosion resistance in most environments because, like almost every metal, it spontaneously forms a protective, thin oxide layer on its surface. However, any damage of this layer, that is only a few nanometres thick, can lead to a corrosive attack. The susceptibility of an Al-alloy to corrosion depends on metallurgical aspects, mechanical aspects (loading of parts), surface roughness and corrosive agents [68, 77]. An important corrosive agent for aerospace parts is seawater, which may lead to marine corrosion. From metallurgical point of view, the dominant factors in corrosion susceptibility are grain size, structure and the distribution of a second phase [52]. The second phase, or intermetallic particles, can occur in the form of constituent particles, dispersoids or precipitations and have different electrochemical characteristics than Al and may be either anodic or cathodic relative to the matrix [52]. This phenomenon is called microgalvanic or even nanogalvanic corrosion. According to [47], the most common types of corrosion in Al are pitting, stress corrosion cracking (SCC) or intergranular-, exfoliation-, crevice-, galvanic- or tribo-corrosion.

Pitting is a form of electrochemical localised corrosion which leads to cavities from the surface extending into the material [76]; it is the most common corrosion attack for Al alloys

2. Fundamentals

and very insidious. The pit nucleation on the surface and pit growth propagation downwards into the material can lead to severe crack initiation. Pitting corrosion is rated as very critical in environments that contain quite aggressive anions, like chloride in seawater. Pitting can be analysed and provoked by an alternating dipping of a test specimen in a NaCl solution (AIC testing) and is gauged in general by optical evaluation or pit counting on a defined area.

Stress corrosion cracking relates to the susceptibility of a material subjected to tensile loading in a corrosive environment to initiate cracks along grain boundaries which may lead to the failure of the part. The combination of tensile stresses and a corrosive medium makes this form of corrosion quite dangerous as SCC can occur on susceptible Al alloys already in media which are not highly aggressive at a tensile stress level that is usually small and less significant than the macroscopic yield stress [52]. Pitting and SCC can be tested in the same environment with the same duration of exposure to a NaCl solution to analyse both, the general corrosion susceptibility and the impact of tensile loading.

Intergranular corrosion (IC) is a special type of selective corrosion that is microstructurally influenced. IC requires testing for supersaturated alloys where potentially a second phase or precipitation-enriched grain boundary region develops after exposure to elevated temperatures. Micro- or nanogalvanic corrosion is activated if these precipitations are either anodic or cathodic to the solid solution. Almost every AlMg alloy is supersaturated and can form precipitations as the solubility of Mg at room temperature is quite small (see Section 2.2.1), and the Mg content of Scalmalloy and SilmagAl leads to the formation of a supersaturated solid solution. The intensity of the intercrystalline attack depends on the presence and continuity of the un-noble second phases Al_3Mg_2 or Al_8Mg_5 , especially after sensitisation. Intergranular corrosion measurements can be performed for Scalmalloy with the use of ASTM G67 [78], a special standard for 5XXX series alloys.

Exfoliation corrosion (EXCO) is frequently a type of Intergranular corrosion (IC) that occurs in general on flattened microstructures with elongated grain boundaries in materials which were rolled, extruded or forged [52]. The attack proceeds from transverse edges parallel to the surface by forming a corrosion product of higher volume than the metal matrix [79]. This swelling leads to a peeling off in layers. Again, a special standard for wrought 5XXX series alloys containing more than 2.0 wt.-% Mg is available in ASTM G 66 [79].

But it is important to mind that a corrosive attack in an airplane is frequently a combination of these fundamental corrosive types. Environmentally assisted cracking (EAC) describes for example the corrosive attack to a material in interaction with its environment and may include SCC, liquid metal embrittlement, corrosion fatigue and hydrogen embrittlement [80, 52]. Testing of EAC is difficult on a laboratory scale, as the actual environmental conditions are part dependent and most often complicated to simulate.

2. Fundamentals

2.4.2. Mechanical properties

The standard static tensile (ST) test is the most important of all mechanical tests, as it gives a brief overview of a variety of characteristics. A test specimen is uni axially to the cross section quasi-statically loaded, while the resulting strains and loads are recorded and referred to the cross-section or gauge length. Test results are usually plotted in a stress-strain-diagram, which demonstrates the proportional limit that allows the calculation of E , the young's modulus, the offset yield strength ($R_{p0.2}$), the ultimate strength (R_m) and elongation at final fracture (A) [81]. Although values from a tensile test are supposed to be independent from the specimen shape, ideally cylindrical bars should be tested for new materials to limit geometrical influence to a minimum, as the stress ratio is here comparably simple.

Parts in airplanes are in reality often cyclically loaded at different amplitudes and unexpected vibrations during take off, cruise or landing can occur. Hence sustainability against cyclic loads should be proofed in the qualification process, even if designer only consider static loads for dimensioning the part. A typical approach to assess the safe life of a part is to determine the constant amplitude fatigue data, the high cycle fatigue (HCF) and the Wöhler curve at different load ratios (R) for uniaxial loading. Cylindrical specimens with a continuous radius between ends or a notch factor close to 1 are preferable in material investigations to avoid again any geometrical influence. The load level, for a minimum of ten test specimens, shall be regularly distributed and shall lead to failure between 10^4 and at least 3×10^6 cycles (N) according to DIN 6072 [82].

Another frequently used characteristic value is fracture toughness (K_{IC}), which is the resistance of a material to unstable fracture [83]. K_{IC} is more precisely the critical stress intensity factor for the crack tip opening mode I under tensile loading and the assumption that linear elastic plane strain conditions prevail. Traditional strength Al-alloys usually reveal a decrease in fracture toughness with increasing yield strength [84, 85]. It seems to be a conflicting goal for new Al-alloy investigations to secure both, high strength values and a high ductility.

2. Fundamentals

Additionally, important to the estimation of K_{IC} is the determination of the stress intensity threshold value (ΔK_{th}) and the fatigue crack growth rate ($\frac{da}{dN}$), as both together describe the limit at which crack growth starts or stops, the crack propagates and finally fractures. The results of both measurements are generally summarised in a curve that is again mainly defined by the theory of linear elasticity [86] and shows the stress intensity factor range (ΔK) plotted against the ratio of crack length per cycle $\frac{da}{dN}$. An exemplary fatigue crack growth $\frac{da}{dN}/\Delta K$ curve is illustrated in Figure 2.11 and highlights the four different regions. In Region 0, no crack initiation is expected, as the crack initiation starts in Region I and propagates according to the Paris law in Region II, leading to the nonlinear final fracture in Region III.

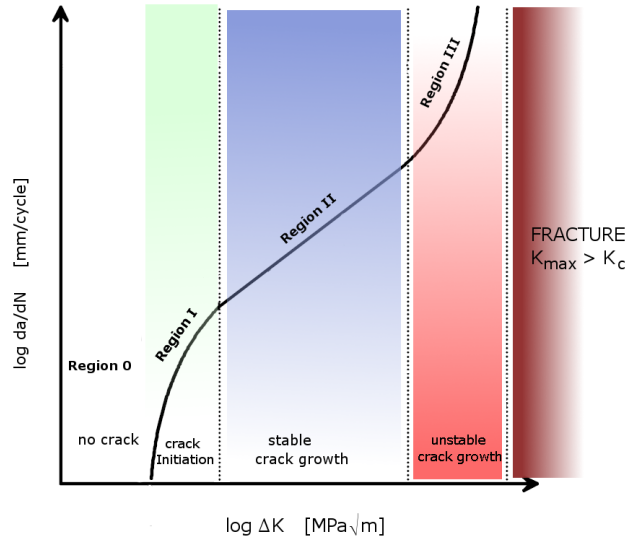


Figure 2.11.: Schematic fatigue crack growth with different regions from no crack to unstable crack growth

3. Experimental Procedure

3.1. Powder identification

Four powder suppliers with different atomising techniques were tested in order to evaluate the characteristics of the atomised Scalmetalloy and SilmagAl powders.

As atomising techniques, inert gas atomisation (IGA), electrode induction melting gas atomisation (EIGA) and one non-disclosed method were used. The core principles of IGA and typical influencing parameters are shown and described in [74]. The EIGA atomisation with its core parameters is depicted in [72]. The inert gas used for both, IGA and EIGA trials, is N₂. Feedstock for IGA is the molten Al-alloy, either by melting a pre-alloyed master or melting Al and adding alloying elements directly. The liquid Al-alloy is held for a certain time in the liquid state in a tank, ideally under an inert gas atmosphere. It streams or is pushed afterwards horizontally or vertically, upwards or downwards, through a gas nozzle configuration into an inert-gas-filled chamber. Here the gas to metal ratio is the dominant factor in controlling particle size [65]. Gas-atomising units are available in most different designs.

Feedstock for the EIGA process is the final Al-alloy chemistry in rod shape. A rotating rod serves as an electrode and is non-contacting directed into a ring-shaped induction coil. The surface of the rod melts uniformly, due to the rotation. The molten metal is then atomised, similar to conventional gas atomisation systems by individual gas nozzle configurations.

No information is available about the manufacturing of the two powder batches as the patent of this atomising technique is currently pending. Different possibilities are anticipated. One option might be ultrasonic or vibrational atomisation (recently known only on a laboratory scale) or the melt drop vibrating orifice technique, as explained in [65].

3. Experimental Procedure

Table 3.1.: Scalmalloy and SilmagAl powders and supplier

| Batch I | Batch II | Batch III | Batch IV | Batch V |
|------------|------------|--|------------|------------|
| Scalmalloy | | | | |
| supplier 1 | supplier 2 | supplier 3 (Lot a.) supplier 3 (Lot b.) | supplier 2 | supplier 4 |
| IGA | | | Eiga | unknown |
| SilmagAl | | | | |
| supplier 3 | supplier 4 | | | |
| IGA | unknown | | | |

3.1.1. Flowability

Standard test methods for measuring the flow rate of metal powders are using preferably a funnel flowmeter with an orifice of 2.5 mm (Hall) or 5.0 mm (Carney) as explained in ASTM B213 and ASTM B964. If a powder is non-free flowing through a Hall funnel, a Carney funnel can be used alternatively. Three of the eight tested powder batches were non-free flowing through a Hall funnel. For this reason, the flow rate of all used powder batches were measured by use of a Carney funnel similar to ASTM B964 [87]. The test procedure was as follows: A finger was placed on the orifice of the Carney funnel, and afterwards 50g of a powder was poured into the funnel and timed by a stopwatch, starting as soon as the finger is removed and stopped when the last powder particle flows through the orifice of the funnel. Three measurements per powder were done under same test conditions. The flow rate FR_C is reported as follows:

$$FR_C = \frac{t}{m} \quad (3.1)$$

Dynamical flowability is measured by means of the avalanche angle (α_P), avalanche energy (E_{av}) and surface fractal (ψ_P) with the Revolution Powder Analyzer (RPA) of manufacturer Mercury Scientific Inc., Newton. A schematic drawing of the RPA drum, α_P and ψ_P is given in Figure 3.1. For the measurements, 100ml powder filled a rotating drum with glass panes on two sides. A digital camera took images of the powder and the resulting avalanche angle during the rotation process. The rotation is adapted to each powder after a pre-run with 315 avalanches and set to 0.2 - 0.5 rotations per minute (rpm). A total of five measurements per powder batch, consisting of 115 avalanches per measurement, were analyzed. According to a patent-pending algorithm, a resulting avalanche angle α_P is calculated. The α_P is the angle of the slope right before an avalanche starts [88] and hence an indirect measurement of the powder's cohesiveness. The amount of energy released by an avalanche is represented as E_{av} and assumed to be a direct measurement of a powder's cohesiveness. The fractal ψ_P

3. Experimental Procedure

is a mathematical description of a convoluted curve that analyses the powders bulk surface roughness after each avalanche. A surface fractal equal to 2 is supposed to correspond to a perfectly smooth surface. If the surface of the powder gets a surface fractal value ψ_P greater than 5, it is assumed that the powder is not suitable for SLM processes [89].

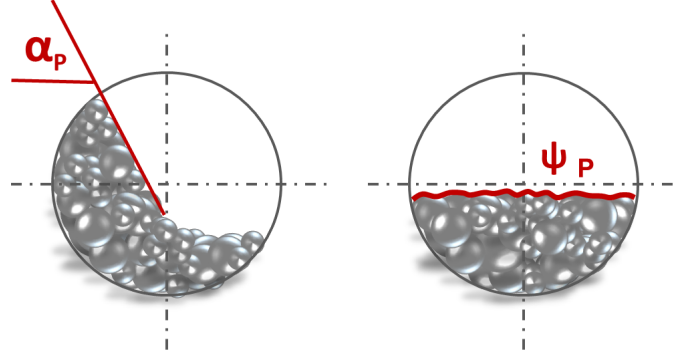


Figure 3.1.: Schematic drawing of a revolution powder analyser (RPA): Left side: Avalanche angle α_P right before an avalanche starts; Right side: Surface fractale ψ_P describing powders reorganised surface after an avalanche

The flowability analysis according to Hausner uses the ratio of tap and apparent density. The variable H is classified in accordance to [90] in Group A ($H < 1.25$), B ($1.25 < H < 1.4$) and Group C ($H > 1.4$). Group A is considered free flowing, B shows behaviour of A and C, and C is considered as non-free flowing.

$$H = \frac{\rho_t}{\rho_{ac}} \quad (3.2)$$

3.1.2. Bulk properties

The determination of the apparent density is described in DIN EN ISO 3923 as a funnel method for free-flowing metallic powders by use of a 2.5 mm or 5 mm diameter orifice, equivalent to Hall or Carney funnels. As such, the same flowmeter device as for flow rate measurements (in Section 3.1.1) was used to take measurements here. The cylindrical cup had a volume of $V = 24.84 \text{ cm}^3$, slightly different from the stipulated $V = 25 \text{ cm}^3 \pm 0.03 \text{ cm}^3$ of [91]. A powder test portion with a volume $V \geq 100 \text{ cm}^3$ was poured into the Carney funnel and from that directly into the cup until it was filled and the powder flowed over [91]. Spare powder on the top of the cup was wiped off with a knife similar device. The mass of the powder, filling exactly the cup volume $V = 24.84 \text{ cm}^3$, is determined to the nearest 0.01g. Three measurements per powder were done under the same test conditions. The apparent density is given as follows:

$$\rho_{ac} = \frac{m[\text{g}]}{V[\text{cm}^3]} \quad (3.3)$$

The tap density is measured at IFAM Dresden in accordance to DIN EN ISO3953. A cylindrical glass cup with an overall volume of $V = 25 \text{ cm}^3$ and a graduation of 0.2 cm^3 was filled with

3. Experimental Procedure

$m = 20 \pm 0.1$ g powder. Spare powder on the cup's surface was wiped off. Afterwards the cup was set into a tap device and tapped 3000 times until no further reduction of the powder took place. The tap density is calculated as follows:

$$\rho_t = \frac{m[g]}{V[cm^3]} \quad (3.4)$$

3.1.3. Particle morphology

The morphology of the powder particles was investigated in two different ways. Scanning electron microscope (SEM) pictures were analysed at different magnifications as were microsections at different magnifications for each powder batch. The evaluation of the particle morphology follows the qualitative description of [92].

3.1.4. Particle size distribution and particle size

A test method determining the particle size distribution by light scattering or laser diffraction is according to [70] described in standard ASTM B822 or ISO 13320.

The particle size distribution was measured by use of a FRITSCH analysette 22 COMPACT (laser diffraction instrument) according to [93] or [94]. Powder samples are dispersed in water and circulated through a converging laser beam. The light of the laser is deflected depending on the particles' properties. Three background measurements were done to exclude any possible contamination of the water and are eliminated from the current result. Powder samples were added to the dispersing unit until a beam absorption between 7% and 15% was reached. The dispersing unit is an ultrasonic bath with a stirrer to ensure an optimal dispersion, a homogenisation of the powder samples and dissipation of agglomerations. Three scans, or alternatively three measurements were done per powder sample. Afterwards the PSD is calculated in accordance with the standards of the Fraunhofer or Mie theory [95]. For all samples, the mean values are analysed in d10, d50, d90 and the cumulative particle size distribution. The range, also represented by d10 and d90, is also given by a non-dimensional coefficient called *Span* (see Equation 3.5). Powder of identical particle sizes correlates to $Span = 0$, which means the lower the *Span* the narrower the PSD.

$$Span = \frac{d90 - d10}{d50} \quad (3.5)$$

Single particle sizes were measured by use of SEM images and analysed for whether their size was in accordance with diameters d10, d90 and the mean particle diameter d50. These images were also analysed regarding the powder's tendency to form agglomerations. These agglomerations would distort the results of the particle size distribution analysis if they were not completely dissipated during the PSD measurement.

3.1.5. Chemical composition

Major constituents and main influencing alloying elements in Scalmalloy are Mg, Sc, Zr, and Mn and for SilmagAl Si and Mg. In a preliminary powder specification, the range for each al-

3. Experimental Procedure

loying element was defined. Chemical analysis was completed to evaluate the deviation from this specification. If an element corresponds to its pre-set range, it is accounted as "SC - spec conform". Otherwise, the deviation to the mean specification value is given in percent.

The chemical compositions of Scalmalloy and SilmagAl Batches I and II were analysed externally at the Revierlabor Essen and IFAM Dresden by use of inductively coupled plasma optical emission spectrometry (ICP-OES). Scalmalloy Batch IV analysis was split element-wise. Magnesium and Mn were detected by flame atomic absorption spectrometry (F-AAS), and Sc and Zr by ICP-OES. The supplier of both Scalmalloy Batch III and V provided the chemical composition in their delivery sheet.

ICP-OES uses an inductively coupled plasma to produce excited atoms that emit electromagnetic radiation at wavelengths characteristic of a particular element and F-AAS uses absorption spectrometry to determine an element content.

Oxygen, as non-metal material, was determined by carrier gas hot extraction (HE) Scalmalloy Batch I, IIIa, b, V and SilmagAl Batch I. Samples for oxygen analysis by HE are heated, molten and transmitted from the gaseous phase to the carrier gas. Oxygen escapes in form of CO or CO₂ and is analysed by infrared spectroscopy.

3.1.6. Micro structural impurities, phases and porosity

Different types of impurities are explained in Section 2.3. To detect all types of impurities, two different methods of analysis were used. On the one hand energy dispersive X-ray spectroscopy (EDS) analysis on different particles was completed to determine qualitatively possible extrinsic impurities (quantitative classification was already done in chemical composition analysis). On the other hand, the existence and intensity of dissolved impurities, phases and porosity was evaluated by an analysis of microsections of the powder.

All microsections in this thesis were prepared with the following procedure. The samples were hot or cold mounted, ground in a grinding machine of either Struers or Buehler with SiC paper with a grit of 80 to 2400 and afterwards polished by use of different cloths and diamond suspension. After investigating the microstructure at different light microscopes in the polished condition followed an additional etching step. Conventional etching of Aluminium for 10 - 60s was used to quickly provide an overview of the microstructure, and the Barkers method of electrolytic etching was chosen as an efficient technique for both Al alloys to highlight grains, dendritical structures or any other microstructural zones.

3.2. Process parameter identification

The basis for every aerospace qualification is a stable manufacturing process that enables a production of multiple blanks or parts at consistently high quality. Aim of the parameters definition is the detection of the most influential process parameters, on the one hand, and to detect the most significant powder characteristics for getting high-quality microstructure after SLM, on the other hand.

The main influencing process parameters and powder characteristics for Scalmalloy and SilmagAl are seen in the Ishikawa diagram, presented in Figure 3.2. Both, process and powder, are closely related to each other and must always be considered simultaneously. Slight differences in powder characteristics may lead to a significantly different SLM process response. Suitable process parameters for one powder batch do not necessarily work for another batch, even though both are manufactured under the so far existing specification and considered to have the same quality. The following investigations show that generally used powder characteristics, for example, flow rate (FR_C) are more likely to describe a sufficient rather than necessary condition of powder behaviour in powder bed fusion processes.

Lasers in all used machines (P1 - P5) offer a high beam quality $TEM_{00} - Mode, M^2 < 1.1$ and use either F-theta lense or a 3D optical system. Laser quality as an influencing parameter was ruled out. The chosen inert gas on platform P1, 2, 4, 5 for both alloys was Ar. Nitrogen (N) was used in the industrial environment for Scalmalloy powder Batch II on platform P3 and Parameter Set 4 (see further explanation for parameter sets in Section 4.2 and Table 4.9).

The process parameters investigation for Scalmalloy followed two different approaches; the laser welding approach that based on the P_L/d_f ratio (Equation 2.4) and associated aspect ratio A_N (Equation 2.3) and the common method in SLM AM, which is based on volume energy density E_V (see Equation 2.2). Single weld traces, multi-weld traces, cubes and static tensile test bars were manufactured with different parameters for metallographical investigations (see explanation given in Section 3.1.6) or mechanical testing (as in Section 3.4.4).

The experiences of the extensive parameters study for Scalmalloy allowed a simplified approach for SilmagAl by investigating cubes metallographically and testing coupons regarding static strength. SilmagAl parameters investigations were completed only by investigating the influence of the scanning velocity v_s and the hatch distance h for a constant P_L/d_f ratio (Equation 2.4) on the porosity and static strength.

3. Experimental Procedure

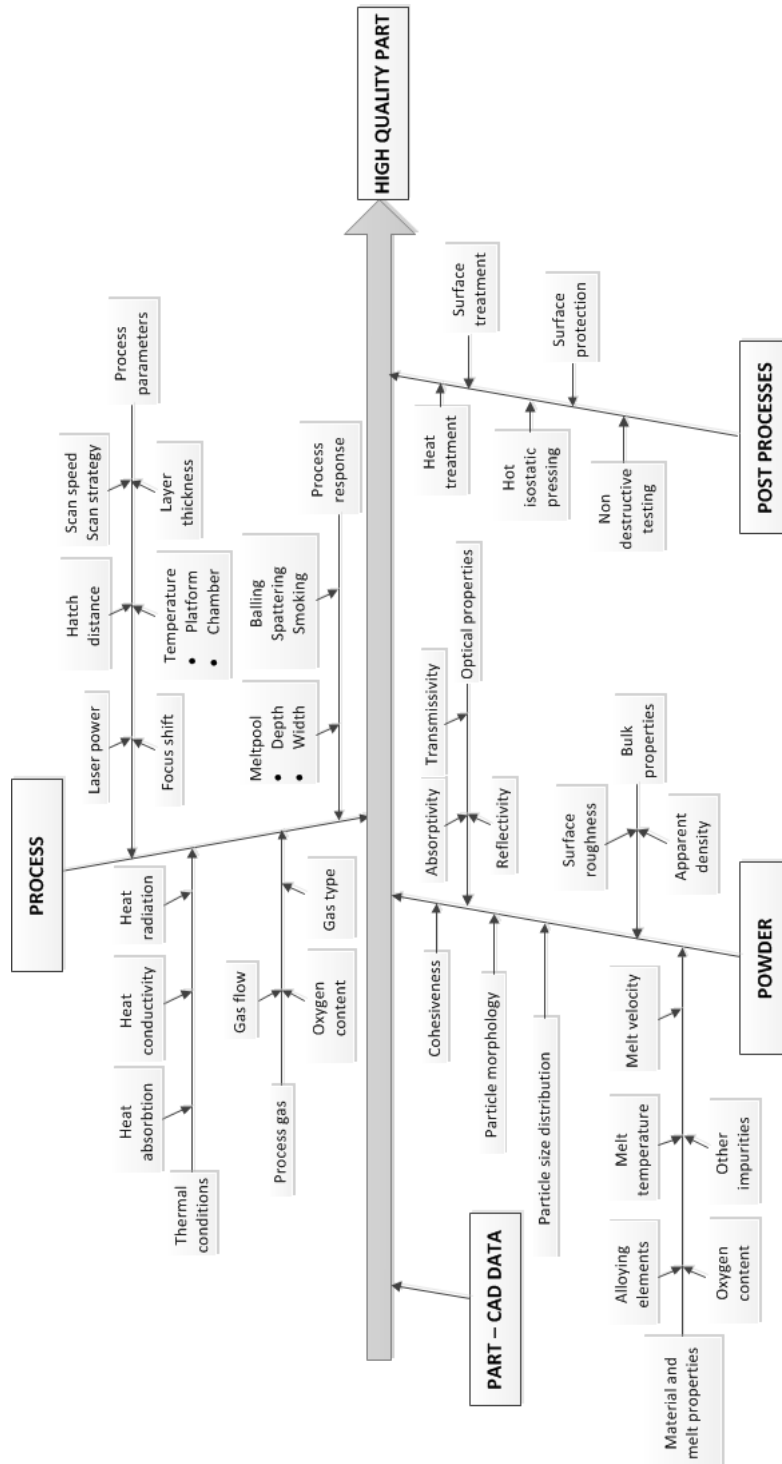


Figure 3.2.: Principle powder characteristics, parameters and post-processing steps for SLM of Scalmalloy and SilmagAl in an Ishikawa diagram in accordance with [96, 97, 29, 27]

3.3. Post-build temper conditions

3.3.1. "As built" condition

The SLM process is a welding process of up to several thousand layers over one another where each layer is molten several times and mainly influenced by the HAZ of superior layers and welding paths. The heat that results from the process does not completely dissipate, which also leads to an increase of the build chamber temperature up to 100 °C. In terms of reduction of residual stresses, it is often even necessary to keep a certain temperature in the part and chamber. Hence a preheating of up to 200 °C is most probable for industrial applications. However, this all means that a part or blank out of an SLM process has already a certain temper condition which is generally neither constant over the part nor easily describable. This condition is referred to as "as built".

3.3.2. Heat treatment

Both Al alloys, Scalmalloy and SilmagAl, are age-hardenable and tested in different temper conditions. The only possible post heat treatment for Scalmalloy to reach its full strength potential caused by the addition of Sc and Zr is a heat treatment that causes precipitation hardening. The established cycle for Sc modified Al alloys in Airbus ranges temperatures from 300 °C up to 325 °C and a duration of 4 - 8 hours.

However for AlSiMg alloying systems, more heat treatment options are useful. Normally, in structural applications for casting alloys like A356, a T6 heat treatment is required. The T6 treatment is a combination of solution annealing at around 525 - 550 °C, water quenching and an ageing step at 150 - 180 °C. Solution annealing brings both alloying elements Mg and Si into solution. Any segregations are removed, the eutectic Si phase is spherodised and the alloy's ductility is increased [98, 47]. Water quenching creates a supersaturated solid solution and a subsequent ageing step leads to the formation of Mg₂Si precipitations which further increases strength. Annealing is conventionally done in the range of 8 - 24 h and ageing for 3 - 10 h. However, the microstructure of AM SilmagAl differs significantly from the established and well understood cast microstructure, as a very fine eutectic microstructure is obtained.

Li shows in [99] that for AM AlSi10Mg a solution heat treatment is sufficient already at very short durations. The T6 condition for SilmagAl corresponds therefore to a solution heat treatment step at 550 °C / 1 h, water quenching and an additional age hardening step. The duration of ageing was investigated in more detail by analysing the static strength response in dependence of ageing time (0 - 7 h) at 165 °C.

Whether the removal of any segregation or the spherodisation is beneficial for the material behaviour was tested by comparing mechanical properties of both conditions, direct ageing at 165 °C for 7 h and T6. All heat treatments were undertaken by use of several different in-house furnaces.

3.3.3. Hot isostatic pressing

It is generally assumed that porosity occurs in AM parts or blanks. An additional compacting step at different temperature levels was realised by hot isostatic pressing (HIP) for both

3. Experimental Procedure

Al alloy options. HIP, according to [92], is the activation of diffusion and creep processes at elevated temperatures under pressure, transmitted by a gas. It can further be assumed that if the porosity is mainly of a spherical shape in a low diameter range, an additional HIP process can reduce this porosity to a minimum by compressing pores.

All HIP runs were undertaken at the Forschungsinstitut für anorganische Werkstoffe-Glas/Keramik GmbH, in Höhr-Grenzhausen, at the company Bodycote in Saint Nicolas d'Algermont or in-house. Scalmalloy was hot isostatic pressed at 325 °C / 4 h / 1000 - 2000 bar and SilmagAl at 540 °C / 2 h / 1000 bar, both under Ar atmosphere. Creep processes were assumed to occur in both alloys; however, it is only possible in SilmagAl at 540 °C to activate diffusion processes.

3.4. Material characterisation: physical and mechanical testing

For monitoring reasons, each platform was divided into four quadrants, as seen in Figure 3.3, to describe precisely each sample position. Test coupons for the material characterisation were built as cubes, blocks, cylinders or as net shape samples. Blocks and cylinders were milled to the final shape for the mechanical testing. Anisotropic material behaviour in z- and xy- directions is assumed according to previous investigations of Scalmalloy and AlSi10Mg in SLM processes within the frame of the nationally funded project AluGenerativ [1]. As the scan parameters for both materials were chosen to alternate randomly in xy-direction, no distinction between xy or yx is made. Additionally to z and xy direction, a number of samples built at 45 degrees were investigated for Scalmalloy.

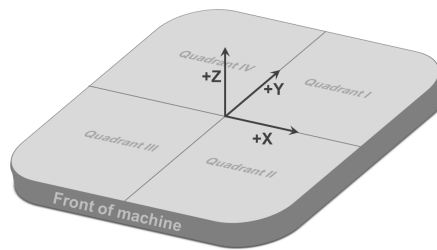


Figure 3.3.: Typical SLM platform; axis according to standard terminology according to [100]

Samples, built of Scalmalloy powder Batch I and SilmagAl powder Batch I, were used for a comprehensive characterisation. However, Scalmalloy Batch II, III b and V and SilmagAl Batch II were tested only in extracts. The overall material characterisation test matrix for both alloys is shown in Table 3.2. The detailed procedure for each test and corresponding specimens are given in Sections 3.4.1 to 3.4.6.

3. Experimental Procedure

Table 3.2.: Material characterisation test matrix of Scalmalloy and SilmagAl

| Scalmalloy | | | | | | | | | |
|--------------|----|-----|--------------|--------------------------|-----------------|-----|-----|----|------|
| Powder Batch | ST | HCF | K_{IC}/K_q | $\frac{da}{dN}/\Delta K$ | ΔK_{th} | SCC | AIC | IC | EXCO |
| I | x | x | x | x | x | x | x | x | x |
| II | x | x | x | — | — | x | x | — | — |
| IIIb | x | — | — | — | — | — | — | — | — |
| SilmagAl | | | | | | | | | |
| Powder Batch | ST | HCF | K_{IC}/K_q | $\frac{da}{dN}/\Delta K$ | ΔK_{th} | SCC | AIC | IC | EXCO |
| I | x | x | x | x | x | x | x | — | — |
| II | x | x | x | — | — | — | — | — | — |

3.4.1. Microstructural response

The analysis of the additive manufactured microstructure of Scalmalloy was effected by means of light microscopy, SEM or transmission electron microscopy (TEM). Microsectional preparation was done as described in Section 3.1.6. The light microscopic and SEM analysis was done in-house, however, TEM investigations were contracted and performed in cooperation with the Department of Physics of Materials at Charles University in Prague. The TEM was equipped with a selected area electron diffraction apparatus (SAED) to allow the determination of certain phases. However, SilmagAl was analysed less comprehensively, with the use of only light microscopy.

3.4.2. Density

Density was measured by the computation method proposed by the Aluminum Association (AA) which uses the chemical composition of Al alloys as basis for the density estimation. The concentration of each alloying element is multiplied by an element-specific factor. The products of all occurring elements are added together, and the number 100 is divided by the total [101]. The quotient is the density of the alloy and rounded to five decimal places. Another approach is to determine the density by use of the Archimedean principle similar to DIN-EN 993-1 or by optical evaluation of microsections. Both alternatives are discussed.

3.4.3. Corrosion analysis

The following different tests were chosen to get initial information about the corrosion behaviour of both alloys. Scalmalloy was analysed regarding AIC, IC, EXCO and SCC, however SilmagAl was tested regarding susceptibility of AIC and SCC. Scalmalloy specimens were, in addition to the ageing heat treatment, sensitised to analyse the risk of potential β -phase diffusion to grain boundaries, as explained in Section 2.2.1. Hence, samples were exposed to

3. Experimental Procedure

a temperature of 120 °C for 165 h.

Both alloys' susceptibility to AIC or pitting was tested by use of ASTM G44 for milled specimens in the unstressed condition. The test followed an 1 h cycle which included a 10 min period when the test specimens were dipped into a 3.5% NaCl solution and a 50 min period out of the solution, during which the specimens were allowed to dry [102]. This cycle was continued over 24 h per day over 30 days. Optical, SEM and microsectional evaluations followed to analyse the corrosive attack by evaluation the criticality of the pits and their growth.

Table 3.3.: Overview test samples and heat treatment for alternate immersion test (AIC) test

| Scalmalloy | | | | | | |
|--------------|-----------------|--------------------------|----------|---|------------------------|-------------------|
| Powder Batch | Number of parts | Dimension (X - Y) Z [mm] | Platform | Heat treatment [h / °C / bar] | Sensitisation [h / °C] | Test duration [d] |
| I | 2 | (3 - 60) 30 | P1 | 300 / 4 | 168 / 120 | 30 |
| I | 2 | (3 - 30) 60 | P1 | 300 / 4 | 168 / 120 | 30 |
| II | 3 | (3 - 40) 25 | P5 | 325 / 4 / 2000 325 / 4 | 168 / 1 20 | 30 |
| SilmagAl | | | | | | |
| I | 3 | (40 - 3) 25 | P5 | 540 / 2 / 1000 550 / 1 / WQ 165 / 7 | | 30 |

Stress corrosion cracking (SCC) was tested according to standard ASTM G49 in a stressing frame under constant load and the same test conditions of AIC in ASTM G44. An axial load of 90% of R_m was applied by tightening a nut of one bolt and was determined by measuring the change in the rig. Shortly after loading followed the exposure to the 3.5% NaCl solution. Samples were dimensioned referring to DIN 50125 [103] to cylindrical test coupons B6 x 40 with extended test length and B6 x 30.

3. Experimental Procedure

Table 3.4.: Overview test samples and heat treatment for stress corrosion cracking (SCC) test

| Scalmalloy | | | | | | | |
|--------------|-----------------|-----------------|-----------|-----------|--|---------------------------|----------------------|
| Powder Batch | Number of parts | Build direction | Dimension | Plat-form | Heat treatment [h/ °C / bar] | Sensitisation [h / °C] | Test duration [d] |
| I | 3 | xy | B6 x 40 | P1 | 300/ 4/ - | 168/ 120 | 30 |
| I | 3 | z | B6 x 40 | P1 | 300/ 4/ - | 168/ 120 | 30 |
| II | 4 | xy | B6 x 30 | P5 | 325/ 4/ 2000 | 168/ 120 | 30 |
| II | 4 | z | B6 x 30 | P5 | 325/ 4/ 2000 325/ 4 | 168/ 120 | 30 |
| SilmagAl | | | | | | | |
| I | 5 | z | B6 x 30 | P5 | 540/ 2/ 1000 550/ 1/ WQ 165/ 7 | – | 30 |
| I | 4 | xy | B6 x 30 | P5 | 540/ 2/ 1000 550/ 1/ WQ 165/ 7 | – | 30 |

Intergranular corrosion (IC) was tested according to the standard ASTM G67 that describes a procedure for constant-immersion IC for wrought products of Al alloys of the 5xxx series [78]. The resistance against a corrosive attack in nitric acid is determined by the mass loss resulting after exposure to the HNO₃ test solution for 24 h. Additional microsectional investigations were done after testing to evaluate the attack in the test samples.

3. Experimental Procedure

Table 3.5.: Overview test samples and heat treatment for intergranular corrosion (IC) test

| Scalmalloy | | | | | | |
|--------------|-----------------|--------------------------|----------|---------------------------------|------------------------|-------------------|
| Powder batch | Number of parts | Dimension (X - Y) Z [mm] | Platform | Heat treatment [h / °C / (bar)] | Sensitisation [h / °C] | Test duration [d] |
| I | 3 | (6-3) 50 | P4 | 300 / 4 / – | 168 / 120 | 1 |
| I | 3 | (50-3) 6 | P4 | 300 / 4 / – | 168 / 120 | 1 |

The exfoliation corrosion (EXCO) behavior of Scalmalloy was determined by visual inspection according to ASTM G66 after exposure for 24 h at 65 °C to a test solution contained ammonium chloride, ammonium nitrate, ammonium tartrate, hydrogen peroxide and water. The ratings of the corroded specimens distinguished between no appreciable attack and pitting or exfoliation at different intensity levels.

Table 3.6.: Overview test samples and heat treatment for exfoliation corrosion (EXCO) test

| Scalmalloy | | | | | | |
|--------------|-----------------|--------------------------|----------|---------------------------------|------------------------|-------------------|
| Powder batch | Number of parts | Dimension (X - Y) Z [mm] | Platform | Heat treatment [h / °C / (bar)] | Sensitisation [h / °C] | Test duration [d] |
| I | 2 | (40 - 5) 100 | P1 | 300 / 4 / – | 168 / 120 | 1 |
| I | 2 | (100 - 5) 40 | P1 | 300 / 4 / – | 168 / 120 | 1 |

3.4.4. Static tensile testing

Static tensile (ST) tests were performed according to DIN EN 2002-001 [104] or DIN EN ISO 6892 [105] at room temperature on the different universal testing frames of Zwick (1474 and Z250) and Instron (1185) with a test velocity of 1 mm/s until $R_{p0.2}$ and 1 - 5 mm/s until R_m . Samples were dimensioned according to DIN 50125 [103] to only cylindrical B4 x 20, B5 x 25 or B6 x 30 test coupons. Samples made of Scalmalloy powder Batches I, II, IIIb and both Batches of SilmagAl were tested in different heat treatment conditions.

3. Experimental Procedure

Table 3.7.: Overview test matrix for static tensile (ST) test of Scalmalloy



|  | | | | | |
|---|-------------------------------|-----------------|------------|--------------------------|---------------------------|
| Scalmalloy | | | | | |
| Powder batch | Dimension | Build direction | Platform | Heat treatment [h / °C] | HIP cycle [h / °C /bar] |
| I | B6 x 30 B5 x 25 B4 x 20 | xy; z; 45° | P1, P2, P4 | 4 / 300 - 325 | 4/ 300 - 325/ 2000 |
| II | B6 x 30 B5 x 25 | xy; z; 45° | P3, P5 | 0 - 4 / 325 | 4 / 325 / 1000 or 2000 |
| III | B6 x 30 | xy; z | P2 | 2 - 4 / 300 - 325 | 4 / 325 / 2000 |

Table 3.8.: Overview test matrix for static tensile (ST) test for SilmagAl

|  | | | | | |
|---|--------------------|-----------------|----------|-----------------------------|-------------------------|
| SilmagAl | | | | | |
| Powder batch | Dimension | Build direction | Platform | Heat treatment [h / °C] | HIP cycle [h / °C /bar] |
| I | B6 x 30 B5 x 25 | xy; z | P5 | 1 / 550 / WQ 0 - 7 / 165 | 2 / 540 / 1000 |
| II | B6 x 30 B4 x 20 | xy; z | P5 | 1 / 550 / WQ 7 / 165 | 2 / 540 / 1000 |

3.4.5. High cycle fatigue

HCF was tested according to DIN EN 6072 [82] and ASTM E466 [106] at specimens FCE typ A [82] with a notch factor $K_t = 1.035$ subjected to a constant amplitude in air at room temperature. Samples made out of both alloys for Batches I and II were milled to the final shape with a test diameter of 4 mm and a total length of 60 mm. The tests were performed for a load ratio $R = 0.1$ on a resonance tester (Rumul Microtron 654) at frequencies between 100 Hz and 150 Hz or on a servo-hydraulic test machine (Zwick) with a frequency of 15 Hz.

3. Experimental Procedure

Table 3.9.: Overview test matrix for HCF test of Scalmalloy



|  | | | | |
|---|-----------------|----------|--------------------------|--------------------|
| Scalmalloy | | | | |
| Powder batch | Build direction | Platform | Heat treatment [h / °C] | HIP [h / °C / bar] |
| I | xy, z | P4 | 4 / 300 | 4 / 300 / 2000 |
| II | xy, z | P5 | 4 / 325 | – |
| II | xy, z | P5 | 4 / 325 | 4 / 325 / 2000 |
| II | z | P3 | 4 / 325 | 4 / 325 / 1000 |

Table 3.10.: Overview test matrix for HCF test of SilmagAl

|  | | | | |
|---|-----------------|----------|--------------------------|--------------------|
| SilmagAl | | | | |
| Powder batch | Build direction | Platform | Heat treatment [h / °C] | HIP [h / °C / bar] |
| I | xy, z | P5 | 7 / 165 | – |
| | xy, z | P5 | 1 / 550 / WQ 7 / 165 | – |
| | xy, z | P5 | 1 / 550 / WQ 7 / 165 | 2 / 540 / 1000 |
| II | z | P5 | 7 / 165 | – |

3.4.6. Fracture mechanic testing

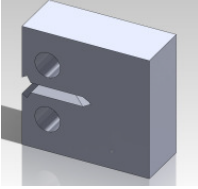
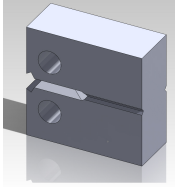
The plane strain fracture toughness (K_{IC}) tests were performed according to ASTM E399 [83] on compact tension specimens. The specimens contained a chevron notch with an angle of 120° to ensure a stable and straight fatigue pre-cracking that was realised in the low cycle fatigue range. Load application on different testing frames of the company Schenk (10 - 100kN) followed the requirements of [83], leading to a load rate between $(0.55 - 2.75) \text{ MPa}\sqrt{m}/s$. An

3. Experimental Procedure

estimation for specimens dimension was done according to the criteria for the specimen thickness $B = 2.5 \left(\frac{K_{IC}}{R_{p0.2}} \right)$ [107], which ensures the validity of linear elastic fracture mechanics. The therefore needed K_{IC} value for Scalmalloy is so far unknown, but was estimated to be around $K_{IC} < 35 \text{ MPa}\sqrt{m}$ as the static tensile testings revealed rather ductile than brittle material behavior. That revelation led to a minimum samples thickness of $B = 15 \text{ mm}$ which corresponds to a CT30.

An intrinsic fracture toughness estimation for AlSi7Mg alloys can be done with the approach estimated by Speidel [108] and discussed by Tiryakioglu [109] with $K_{Ic(intr)} = 37.50 - 0.058 \sigma_y$. Transferred to SilmagAl with $\sigma_y = R_{p0.2} = 300 \text{ MPa}$ a fracture toughness K_{IC} of $\approx 20 \text{ MPa}\sqrt{m}$ is estimated, and that leads to a specimen minimum thickness of 6mm which is fulfilled by the chosen CT18.

Table 3.11.: Overview test matrix for K_{IC} test

| <div style="display: flex; justify-content: space-around; align-items: center;">   </div> | | | | |
|---|-----------------|----------|--------------------------|-------------------|
| Scalmalloy | | | | |
| Powder batch | Build direction | Platform | Heat treatment [h / °C] | HIP [h / °C /bar] |
| I | xy, z | P4 | 4 / 300 | 4 / 325 / 2000 |
| II | z | P3 | – | 4 / 325 / 1000 |
| II | xy, z | P5 | 4 / 325 | 4 / 325 / 2000 |
| SilmagAl | | | | |
| I | xy, z | P5 | 1 / 550 / WQ 7 / 165 | 2 / 540 / 1000 |

In ASTM E647 [86], several test procedures are provided for measuring fatigue crack growth rates for different scenarios. Crack propagation growth $\frac{da}{dN}$ was determined with a constant load-amplitude and hence increasing ΔK ; however, ΔK_{th} by a reduction of load and a resulting decrease of ΔK . For both alloys were $\frac{da}{dN}$ and ΔK measured on C(T) specimens with a crack growth either parallel to the layer in xy-direction or perpendicular to the layer in z-direction for two different load ratios ($R = 0.1$ and $R = 0.7$) on an Instron test frame under frequencies between 10 and 30 Hz.

The starting load chosen for a $\frac{da}{dN}/\Delta K$ test, corresponded to a $\Delta K = 8 - 10 \text{ MPa}\sqrt{m}$ for a load

3. Experimental Procedure

ratio $R = 0.1$ and approximately $\Delta K = 4 \text{ MPa}\sqrt{m}$ for a load ratio $R = 0.7$. The aim is to choose a ΔK within the Paris regime (cf. Figure 2.11) to ensure a stable crack growth in region II.

Fatigue crack propagation threshold measurements for both alloys were also started with loads corresponding to a ΔK of the Paris regime around $\Delta K = 9 - 12 \text{ MPa}\sqrt{m}$ for load ratio $R = 0.1$ and $\Delta K = 3 - 4 \text{ MPa}\sqrt{m}$ for an load ratio of $R = 0.7$. The load reduction followed a certain sequence of steps and was reduced by about six percent if the crack lengthened about one-tenth of a millimeter. A threshold ΔK_{th} was obtained if either no crack growth was visible anymore or if crack growth rates decreased below 10^{-8} mm/cycle .

Table 3.12.: Overview test matrix for $\frac{da}{dN}/\Delta K$ und ΔK_{th} test

| Scalmalloy | | | | |
|--------------|-----------------|----------|------------------------|----------------|
| Powder batch | Build direction | Platform | Heat treatment | HIP |
| I | xy, z | P4 | 4 / 300 | 4 / 325 / 2000 |
| SilmagAl | | | | |
| I | xy, z | P5 | 1 / 550 / WQ + 7 / 165 | 2 / 540 / 1000 |

4. Results and discussion

4.1. Results: powder analysis

In this section, the results of the powder analysis of Scalmalloy and SilmagAl are presented and discussed. The focus is on the usefulness of these powders in SLM processes. Each powder batch was sieved under gas atmosphere before being analysed. Significant differences between the sieved and non-sieved (as delivered) condition were noted, especially for Scalmalloy powder Batch II, which contained many coarse particles. Because the powder was sieved as a standard procedure before being processed, the non-sieved condition was not investigated further.

Scalmalloy Batch IV was not equally comprehensively investigated like all other powder batches, as the chemical and microsectional analysis had already revealed significant deviations from the pre-set specification.

The flowability results highlighted the complex relation with several powder characteristics. Bulk densities were, as expected, within an acceptable range. Particle morphology revealed that all tested atomisation processes had produced mainly spheroidal particles. The particle size distribution analysis showed, that a broad PSD range of $0.46 \leq \text{Span} \leq 1.65$, was captured for Scalmalloy, whereas the investigations on SilmagAl concentrated on a medium PSD range of $0.52 \leq \text{Span} \leq 0.85$ only. Single particle size measurements yielded by SEM correlated in all cases with the optically measured PSD. Chemical analysis showed that deviations from the pre-set specification occurred for different Scalmalloy powders. Both SilmagAl powders conform with pre-set specifications for chemical composition. Microsectional analysis highlights specific challenges for each atomising method, as inner-particle porosity and undesired phases were noted.

4.1.1. Results: flowability

The flow behaviour characteristics (FR_C , H , α_p , E_{av} and ψ_p) of Scalmalloy and SilmagAl powder batches are summarised in Table 4.1.

4. Results and discussion

Table 4.1.: Flow rate of Scalmalloy and SilmagAl powders

| | Batch I | Batch II | Batch III | Batch IV | Batch V |
|--------------------------|---------|----------|--------------------|----------|---------|
| Scalmalloy | | | | | |
| $FR_C [\frac{s}{50g}]$ | 45.4 | 13.3 | a. 10.2 b. 9.4 | — | 9.2 |
| $\alpha_P [^\circ]$ | 46.6 | 52.3 | a. 38.4 b. 44.1 | — | 33.8 |
| $E_{av} [\frac{kJ}{kg}]$ | 12.4 | 30.6 | a. 11.5 b. 18.9 | — | 15.5 |
| $\psi_P [-]$ | 1.9 | 2.8 | a. 2.5 b. 2.4 | — | 2.9 |
| $H [-]$ | 1.24 | 1.26 | a. 1.16 b. — | — | 1.14 |
| SilmagAl | | | | | |
| $FR_C [\frac{s}{g}]$ | 8.8 | 7.3 | | | |
| $\alpha_P [^\circ]$ | 43.9 | 33.4 | | | |
| $E_{av} [\frac{kJ}{kg}]$ | 17.7 | 10.6 | | | |
| $\psi_P [-]$ | 2.4 | 4.4 | | | |
| $H [-]$ | 1.15 | 1.08 | | | |

All powder batches were free flowing through a Carney funnel, without stimulation by e.g. a wire (suggested in [87]) being necessary. Nevertheless, significant differences in each powder's flow behaviour were noted.

Scalmalloy Batch I displayed the slowest flow rate at $FR_C = 45.4 \text{ s/50g}$; Batches IIIa, IIIb and V flowed at $FR_C = 9.7 \pm 0.5 \text{ s/50g}$; and Batch II showed an intermediate flow rate of $FR_C = 13.3 \text{ s/50g}$. SilmagAl Batch I flowed at $FR_C = 8.8 \text{ s/50g}$ and Batch II revealed the highest flow rate of all tested powders, at $FR_C = 7.3 \text{ s/50g}$.

The measured dynamic flow characteristics α_P , E_{av} and ψ_P indicated significant differences in the amount of interparticle forces. The α_P value ranged between $33^\circ < \alpha_P < 53^\circ$, and the avalanche energy E_{av} ranged between $10 \text{ kJ/kg} < E_{av} < 31 \text{ kJ/kg}$. A general assumption is that both values measure the cohesiveness of a powder. Regarding the evaluation of the intensity of interparticle forces, it is furthermore assumed that the released energy outweighs the avalanche angle. When applied to Scalmalloy powder batches, this logic means that Scalmalloy Batch II has the highest interparticle forces at $E_{av} = 30.6 \text{ kJ/kg}$ ($\alpha_P = 52.3^\circ$); and Scalmalloy Batch IIIa has the lowest, at $E_{av} = 11.5 \text{ kJ/kg}$ ($\alpha_P = 38.4^\circ$). SilmagAl Batch II displayed lower

4. Results and discussion

interparticle forces at a lower avalanche energy level and angle than Batch I. Additionally, the measured surface fractal ψ_P revealed differences between $1.9 \leq \psi_P \leq 2.9$ for Scalmalloy and $2.4 \leq \psi_P \leq 4.4$ for SilmagAl. Another assumption is that the surface fractal ψ_P indicates the cohesiveness of a powder as well. The more visible the interparticle forces are, in the form of agglomerations, the more jagged a powder's surface will be. A surface fractal of $\psi_P = 2$ correlates with a perfectly smooth surface, and the $\psi \geq 5$ condition is assumed to be an upper limit for a powders flowability or processability according to [110]. Spierings [89] showed that this assumption might have been valid in his study of Ni and Fe powders. Among the Scalmalloy and SilmagAl batches, the smoothest surface was noted in Scalmalloy Batch I ($\psi_P = 1.9$) and the roughest surface was measured for Scalmalloy Batch V ($\psi_P = 2.9$) and SilmagAl Batch II ($\psi_P = 4.4$).

The Hausner ratio (Equation 3.2) is the ratio of tap to apparent density. According to the classification of [90], all investigated powder batches except Scalmalloy Batch II are free flowing. Scalmalloy Batch II is classified as Group B, which shows both free-flowing and non-free-flowing behaviour.

All investigated Al powder batches in this study showed that the evaluation of flowability and hence later on processability, is complex and depends on several factors. Estimating a powders suitability by evaluating only its flow behaviour with one of the used test methods could lead to faulty conclusions. The relationships between flow behaviour and other powder characteristics are discussed in detail in Section 4.1.7.

FINDINGS:

- The flowability characteristics FR_C and H correlated qualitatively.
- There was no bijective (one-to-one) correlation between FR_C , H and α_P , E_{av} .
 - Fast flow rate values $FR_C \leq 10.5$ s/50g for Scalmalloy Batch IIIa, b and Batch V, as well as SilmagAl Batches I and II correlated very well with a low avalanche angle α_P and low energy values E_{av} .
 - Scalmalloy Batch II had an intermediate flow rate value of $FR_C = 13.3$ s/50g, which resulted in the highest measured avalanche angle α_P and the highest measured avalanche energy level E_{av} .
 - The slow flow rate value of Scalmalloy Batch I, $FR_C = 45.4$ s/50g, did not result in an extraordinary high α_P and E_{av} . Both results, the avalanche angle of $\alpha_P = 46.6^\circ$ and the high energy level $E_{av} = 12.4$ kJ/kg are comparable to Batch IIIa and b with fast flow rates FR_C .
- There was no bijective (one-to-one) correlation between ψ_P and any other flow characteristic (FR_C , H , α_P and E_{av}).
 - The smoothest surface was noted for Scalmalloy Batch I, at $\psi_P = 1.9$, but revealed also the slowest flow rate of $FR_C = 45.4$ s/50g, an intermediate avalanche angle $\alpha_P = 46.6^\circ$ and a low avalanche energy level of $E_{av} = 12.4$ kJ/kg.
 - The highest surface roughness was measured for Scalmalloy Batch V, $\psi = 2.9$, and SilmagAl Batch II, $\psi = 4.4$, with fast flow rates of $FR_C = 9.2$ and 7.3 s/50g,

4. Results and discussion

low avalanche angles $\alpha_P \approx 33^\circ - 34^\circ$ and low avalanche energy levels of $E_{av} = 10.6$ and 15.5 kJ/kg respectively.

- The best process-ability according to RPA is estimated for Scalmalloy Batch I, and the least for Scalmalloy Batch V and SilmagAl Batch II.
- Significant inconsistencies were noted between conventionally measured flow characteristics FR_C and H versus the RPA values α_P , E_{av} , ψ_P . These discrepancies suggest that further studies on powder characteristics are necessary to draw conclusions concerning the processability in SLM processes of Scalmalloy and SilmagAl powders.

4.1.2. Results: bulk density

The apparent density ρ_{ac} in g/cm^3 was determined as described in Section 3.1.1 and is given in the analysis also as a percentage. All values reflect the arithmetic mean of three measurements with a standard deviation of less than 0.05g/cm^3 , and are shown in Table 4.2. The reference densities of Scalmalloy and SilmagAl refer to density of the AM material and are given in Section 4.4.1 by Equations 4.1 and 4.2. All powders used in this study had an apparent density of $\rho_{ac} \geq 49.5\%$. Therefore, the ratio of powder particles to cavities in the packing was almost equal ($= 0.98$) in the worst case scenario (Scalmalloy Batch II); in best-case scenario (SilmagAl Batch II) the ratio is almost 1.3 with more solid powder particles in the same volume.

The tap density was determined according to the description in Section 3.1.1 at IFAM in Dresden. The results clearly showed that Scalmalloy Batches I and II displayed the highest potential for compression during stimulation. The apparent density was increased in both batches by $\approx 13\%$ by tapping. SilmagAl Batch II displayed the lowest compressibility with an increase less than 5% relative to the apparent density. Many factors influenced the tap density, as discussed in Section 4.1.7.

FINDINGS:

- The apparent density of all investigated powder batches was $\rho_{ac} \geq 49.5\%$, which is estimated to be sufficient for use in SLM processes.
- Tap density investigations showed that for comparable apparent densities, widely different tap densities could be obtained.

4. Results and discussion

Table 4.2.: Apparent and tap density of Scalmalloy and SilmagAl powders

| | Batch I | Batch II | Batch III | Batch IV | Batch V |
|------------------------------|---------|----------|------------------|----------|---------|
| Scalmalloy | | | | | |
| $\rho_{ac} [\frac{g}{cm^3}]$ | 1.43 | 1.32 | a. 1.49 b. — | — | 1.42 |
| $\rho_{ac} [\%]$ | 53.75 | 49.63 | a. 56.02 b. — | — | 53.38 |
| $\rho_t [\frac{g}{cm^3}]$ | 1.77 | 1.66 | 1.73 b. — | — | 1.62 |
| $\rho_t [\%]$ | 66.54 | 62.41 | 65.04 b. — | — | 60.90 |
| SilmagAl | | | | | |
| $\rho_{ac} [\frac{g}{cm^3}]$ | 1.50 | 1.53 | | | |
| $\rho_{ac} [\%]$ | 55.56 | 56.67 | | | |
| $\rho_t [\frac{g}{cm^3}]$ | 1.72 | 1.66 | | | |
| $\rho_t [\%]$ | 63.70 | 61.48 | | | |

4.1.3. Results: particle morphology

The morphology of the powder particles were investigated qualitatively by SEM and microsectional images. An SEM image summary is shown in Tables 4.4 and 4.3, and exemplary microsections for Scalmalloy Batch I and II are shown in the Appendix A.1.1.

The particle shapes of all tested powder batches were either nodular or spheroidal, according to DIN 3252 [92]; however, each batch showed distinct features.

Scalmalloy Batch I contains a few coarse nodular particles. Scalmalloy Batches III a and b and SilmagAl Batch I show that during atomisation collision of droplets and already-solidified particles took place. Such collision results in particles that are partly coated or in particles that are merged to one nodular particle.

Scalmalloy Batches IV and V reveal mechanical impacts in the form of dented areas (see also Appendix A.1.1). As the intensity of these dented spots differs significantly between both batches, it is assumed that this occurred during solidification in Batch V by particles that flow against each other, or particles that flow against the walls of the cyclone, and during a post process like blasting in Batch IV.

Scalmalloy Batch II has a high number of nodular particles. It is estimated that half of all particles are spheroidal and the other half nodular shaped. The particle shape is mainly controlled by the oxygen content in an IGA process. An oxygen level of 2 % is estimated as a threshold where the shape changes significantly [65]. It is therefore assumed that the oxygen level was higher than 2 % during atomisation. Spheroidal particles also reveal a mechanical impact,

4. Results and discussion

equal to the mechanical impact seen on particles in Scalmaalloy Batch IV, hence is concluded that the same post process was used for both powder batches.

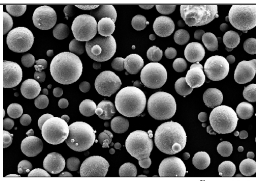
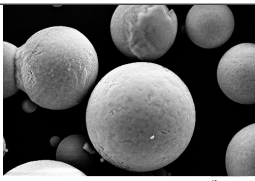

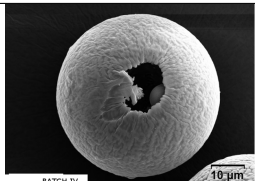
The surface of all powder batch particles reveal solidification in the form of dendritic crystals with varying intensity. Scalmaalloy Batch V and SilmagAl Batch II shows a very fine homogenous dendritic structures on perfectly spherical particles. The fewest dendritic structures among all batches appeared in Scalmaalloy Batch II. This result fits to the assumption that the atomising process contained too much oxygen. Oxygen prevents the earliest solidification in form of dendrites by a pinning effect of oxide nuclei on the droplets. If there are no such oxide nuclei on the droplet, surface tension forces would be able to maintain the spheroidal shape until solidification [73].

Scanning electron microscope pictures also reveal huge differences in PSD between the investigated powder batches. These differences are further explained in the Section 4.1.4.

FINDINGS:

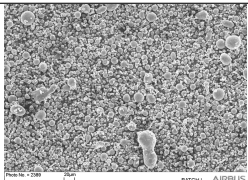
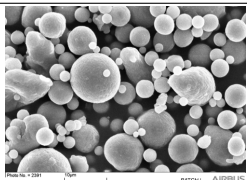

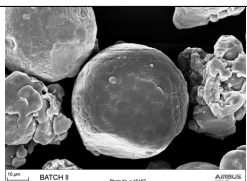
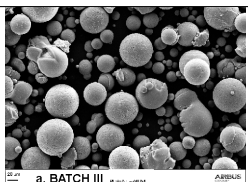
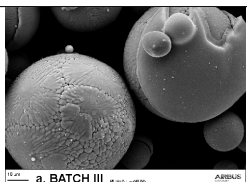
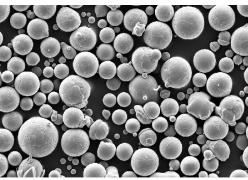
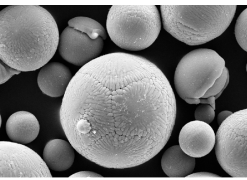
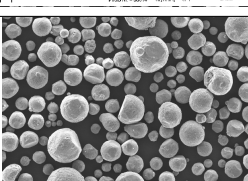

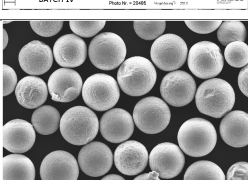

- All powder batches, except Scalmaalloy Batch II, are mainly of spheroidal shape.
- Scalmaalloy Batch V and SilmagAl Batch II reveal phenomenologically the highest sphericity.
- Homogeneously dendritic structures on the surface of Scalmaalloy Batch I, IIIa and b, IV, V and SilmagAl I and II correspond to an ideal gas and oxygen level during atomisation.

Table 4.3.: Scanning electron microscope (SEM) pictures of SilmagAl powders batches

| Batch | Magnification | |
|-------|---|---|
| | 250x | 1000x |
| I |  |  |
| II |  |  |

4. Results and discussion

Table 4.4.: Scanning electron microscope (SEM) pictures of Scalmaalloy powder batches

| Batch | Magnification | |
|-------|---|---|
| | 250x | 1000x |
| I |  |  |
| II |  |  |
| IIIa. |  |  |
| IIIb. |  |  |
| IV |  |  |
| V |  |  |

4.1.4. Results: particle size distribution and particle size

The particle size distribution is given in common representative diameters d10, d50 and d90 (see Table 4.5). The closer d10 and d90 are to each other, the narrower the particle size distribution, reflected in very different Span values from 0.46 to 1.65 for Scalmaalloy and 0.52 to 0.85 for SilmagAl powder batches. Scalmaalloy powder Batch I has by far the widest PS range, at Span = 1.65 with a large number of fine particles below 20 μm and also below 10 μm . Images from SEM even reveal nano sized ($<1 \mu\text{m}$) particles in the powder. A narrow PSD was measured for Scalmaalloy Batch V with Span = 0.46 and for SilmagAl Batch II with Span = 0.52. Remaining powder batches have a medium PSD range between $0.8 \leq \text{Span} \leq 1.15$. The cumulative volume distribution diagrams 4.1 and 4.2 show graphically the differences in PSD range. The amount (10 - 20) % of large particles $> 60 \mu\text{m}$ measured for mainly all powders batches are not necessarily large particles, it can also be likely that the Al powders were not dispersed equally and agglomerations were formed during the measurement. Hence, the optical analysis of SEM pictures is mandatory to evaluate the PSD measurement by laser diffraction. Measured particle sizes are consistent to the respective measured PSD, large particles are most probably agglomerations provoked in the laser diffraction instrument FRITSCH analysette 22 COMPACT and not likely to occur in the SLM process. Images from SEM only reveal very slight, negligible agglomerations in Scalmaalloy Batch I, II a, b and SilmagAl Batch I. Analysed SEM images can be found in Appendix A.1.2.

FINDINGS:

- Scalmaalloy powder batches cover a broad range of different PSD's ($0.46 \leq \text{Span} \leq 1.65$), however SilmagAl powders reveal a narrower range of ($0.52 \leq \text{Span} \leq 0.85$).
- Agglomerations are anticipated by PSD analysis with laser diffraction methods but were not confirmed by optical assessment of SEM pictures of the powder particles.
- It is estimated that there are significant differences in the powder's processability.

Table 4.5.: Particle size distribution (PSD) of Scalmaalloy and Scalmaalloy given in d(x)

| Powder Batch | d10 [μm] | d50 [μm] | d90 [μm] | Span [-] |
|-------------------------|--------------------------|--------------------------|--------------------------|-------------|
| Scalmaalloy Batch I | 9.4 | 29.9 | 58.9 | 1.65 |
| Scalmaalloy Batch II | 23.2 | 39.2 | 6.0 | 0.99 |
| Scalmaalloy Batch IIIa. | 21.8 | 39.4 | 66.7 | 1.14 |
| Scalmaalloy Batch IIIb. | 19.0 | 45.0 | 65.0 | 1.02 |
| Scalmaalloy Batch V | 52.1 | 65.4 | 81.9 | 0.46 |
| SilmagAl Batch I | 24.3 | 43.3 | 61.0 | 0.85 |
| SilmagAl Batch II | 42.0 | 53.0 | 69.5 | 0.52 |

4. Results and discussion

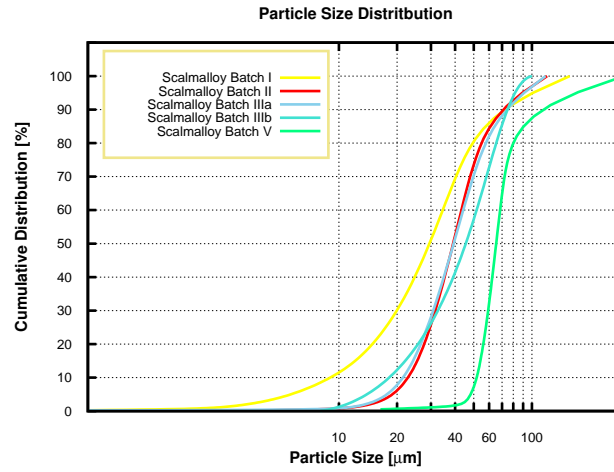


Figure 4.1.: Cumulative particle size distribution (PSD) of Scalmaalloy powder Batches I-III, V

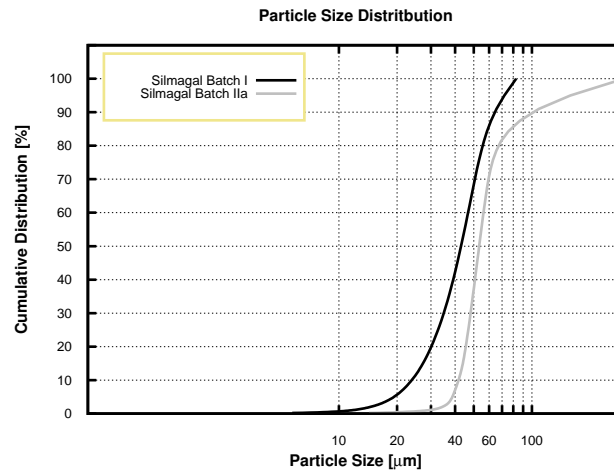


Figure 4.2.: Cumulative particle size distribution (PSD) of SilmagAl powder Batches I-II

4.1.5. Results: chemical composition

The chemical analysis revealed that the composition of Scalmaalloy Batches I, II and SilmagAl Batch I are specification conform regarding major alloying elements. Scalmaalloy Batch III a and b's composition deviates significantly in Mg-content. Batch III b has additionally a higher Sc-content (+ 17 wt.-%) than intended. Both, Mg and Sc are the elements that most influence material properties in the Scalmaalloy composition. A higher Sc content is considered

4. Results and discussion

rather non-critical, as Sc strengthens the material. A level of 0.1 wt.-% Sc leads roughly to an increase in R_m of 50 MPa compared to the alloying composition without Sc. However, this means on the other hand, that a lower Sc content will result in an unacceptable decrease in strength. Scalmalloy Batches IV and V revealed a deviation of - 18 wt.-% and -23 wt.-% in Sc content. The microsectional analysis is here important to analyse whether Sc is dissolved in particles or not (see influence of Sc precipitations in Section 2.2.1). Scalmalloy Batch V also showed a significant deviation of -73 wt.-% in Zr-content (see also influence of Zr as alloying element in Section 2.2.1), which is rated critical.

A higher Mg-content in Scalmalloy is considered very critical because in general an Mg content higher than already 3 wt.-% can decrease the corrosion persistence. The precipitation of the β -Phase Al_8Mg_5 tends to form lines on grain boundaries, especially after sensitisation above 100 °C [46] (see also Section 2.2.1). A lower Mg content, found in Scalmalloy Batches III a and b, results in slightly lower strength values but was nevertheless tested in further analysis. SilmagAl Batch II also revealed a higher Mg content, but the deviation is not rated critical for SilmagAl, as the overall Mg content is far below 3 wt.-%. The deviation in Si content (+12 wt.-%) of SilmagAl Batch II is also not rated critical.

The oxygen content was only partly measured. Scalmalloy Batch I has a 60 % higher oxygen content than intended. Scalmalloy Batches III a, b, IV and SilmagAl Batch I are SC. It is assumed that also Scalmalloy Batch II reveal a deviation in oxygen content, as the particles are 50 % of nodular shape, which is a strong indicator that too much oxygen was present in the gas during the atomisation (cf. Section 4.1.3).

Impurities (either exogenous or intrinsic) like Fe, Cu, Zn and others were also determined and resulted in no deviation to the preliminary specification. All ICP-OES results, however, need to be interpreted with caution, as especially the Scandium content revealed measurements deviations of up to ± 0.05 wt.-%.

FINDINGS:

- The content of major constituents is SC in Scalmalloy Batches I, II and SilmagAl Batch II.
- Scalmalloy Batch IIIa and b are not SC regarding Sc and Mg content. However, their deviation is not considered critical.
- Scalmalloy Batch IV and V are not SC and reveal a lower SC content; they are therefore rated critical.
- Scalmalloy Batch V contains almost no Zr, which is also rated critical.
- SilmagAl Batch II deviates in higher Mg and Si content, but the proportion of neither is rated critical.

4. Results and discussion

Table 4.6.: Chemical composition of Scalmalloy and SilmagAl powder batches in relation to a pre-set specification

| Element | Batch I | Batch II | Batch III | Batch IV | Batch V |
|------------|---------|----------|--------------------|----------|---------|
| Scalmalloy | | | | | |
| Mg | SC | SC | a. -38% b. -15% | SC | SC |
| Sc | SC | SC | a. SC b. +17% | -18% | -23% |
| Zr | SC | SC | a. SC b. SC | SC | -73.3% |
| Mn | SC | SC | a. SC b. SC | SC | SC |
| O | +60% | — | a. SC b. SC | SC | — |
| SilmagAl | | | | | |
| Si | SC | +12% | | | |
| Mg | SC | +38% | | | |
| O | SC | — | | | |

4.1.6. Results: impurities, phases and porosity

Microsectional analysis revealed impurities, undesired phases and porosity in almost every tested powder batch. Only SilmagAl Batch I is free of these features. Scalmalloy Batch I particles have a very low intra- and inner-particle porosity. In the whole microsection, only in one particle is the preliminary Al_3Sc -phase found. The size of this Al_3Sc precipitation is less than $5\ \mu\text{m}$. The etched microsection confirms dendritic solidification, also seen on particles surfaces in particle shape SEM analysis.

Scalmalloy Batch II has a quite similar amount of intra- and inner-particle porosity to Batch I. Intra-particle porosity is mainly found on nodular particles. Some Al_3Sc precipitations are also found, but somewhat coarser ($\approx 15 - 20\ \mu\text{m}$) than in Batch I. Spheroidal particles also reveal solidification by dendritic structures. Scalmalloy Batches III a and b are very similar in microsectional analysis. Hence is only a microsection of Batches III a shown, exhibiting internal voids in less than five particles over the complete microsection. Perfectly spheroidal particles are solidified in fine homogeneous dendritical structures, as already seen on the particles' surface in SEM analysis. Scalmalloy Batch IV also displayed a minor intra- and inner

4. Results and discussion

particle porosity, but coarse preliminary Al_3Sc phases ($> 20 \mu\text{m}$). It is estimated that these coarse precipitations will not be solved during the SLM process, and if they remain as primary precipitations in the AM material, they will not have a strengthening effect. They are moreover intrinsic impurities leading to a decrease in mechanical properties. Scalmalloy Batch V has the highest intra- and inner-particle porosity of all tested Scalmalloy powder batches. There were $\text{Al}_3(\text{Zr}_x\text{Sc}_{1-x})$ phases or precipitations found in almost every particle with a size of $< 5 \mu\text{m}$. It is assumed that these precipitations will be solved during SLM process and do not act as impurities. Again dendritic structures were found.

Both SilmagAl powder batches manifested perfect solidification in fine homogeneous dendritic structures. No impurities in the form of coarse phases were found. A microsection of SilmagAl Batch II revealed, in contrast to Batch I, in very few particles only, spheroidal internal voids. Intra-particle porosity was not found. SilmagAl Batch I is, according to the microsectional analysis, completely free of any impurities.

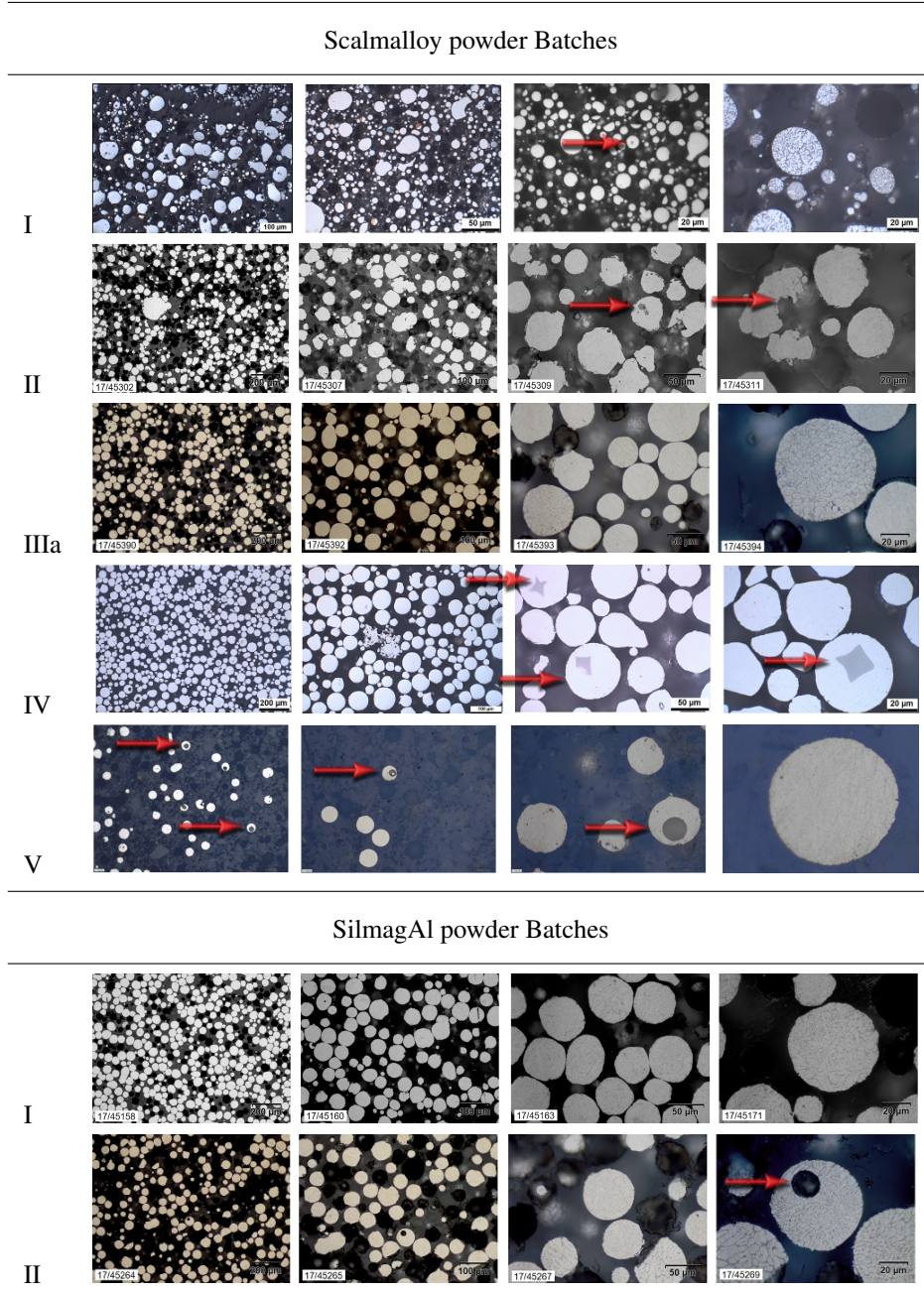
Analysis via SEM and EDS do not find exogenous or dissolved impurities in the form of contaminative elements and confirmed qualitatively the analysis of chemical composition for all Scalmalloy and SilmagAl batches (see Appendix A.1.3).

FINDINGS:

- All Scalmalloy powder batches contained impurities, but with different intensities.
- Scalmalloy Batches I and III a and b contain particles of high microstructural quality. Only few impurities were found.
- Scalmalloy Batches II and V feature a slightly higher proportion of impurities in particles. Both Batches are hence rated as powder of average microstructural quality.
- Scalmalloy Batch IV is excluded from further analysis because of its high number of coarse primary Al_3Sc precipitations in particles.
- Both SilmagAl powder batch particles are of high-quality microstructure.
- SilmagAl Batch I particles are completely free of impurities.

4. Results and discussion

Table 4.7.: Microsections of Scalmalloy and SilmagAl powders



4. Results and discussion

4.1.7. Discussion powder analysis

A broad range of analytical investigations have been made to characterise each powder batch appropriately. Looking at each investigation individually, inconsistent results may be derived. However, an evaluation of all results together creates a better understanding and allows derivations regarding suitability for SLM processes.

Flow behaviour was investigated under very different conditions. Conventional Carney funnel measurements create values that are hardly interpretable with regard to concluding the suitability of a powder in SLM processes. All tested powder batches were free flowing, whereas significant differences occur. Scalmalloy powder batches revealed fast (Batch III a and b and V), intermediate (Batch II) and slow (Batch I) FR_C flow rates. SilmagAl powders showed very fast flow rates.

However, the interpretation of these results with regard to conclude a processability is difficult. Linear extrapolation is not valid. Slight differences, for example in the chosen powder mass, change the results, and a former free-flowing powder may become non free flowing as inter-particle forces change. So, the most significant disadvantage of FR_C is, that it demonstrates only the flowability of 50 g of a powder in a funnel with an angle of 60° . No extrapolation from the test environment to the flow behaviour in a SLM process can be made. Furthermore, if a powder does not flow through a Carney funnel, no estimations can be determined at all. In no used SLM machine does the powder application in the process correspond to a free flow through a funnel. Powder is in every machine dynamically applied with different recoater device configurations. However, they all have in common that a blade straightens the applied powder. As such, only an appropriate reorganisation behaviour of the powder has to be fulfilled.

Flowability, according to Hausner, is based on the ratio of tap and apparent density. Tap density indicates indirectly a certain reorganisation behaviour in form of compressibility. However, tapping the powder is far away from the real process. No used platform provides a stimulation of the applied powder layer to compress it. Investigations of H showed that, except Scalmalloy Batch II, all powders are considered as free flowing. Scalmalloy Batch II is classified Group B showing both effects, flowing and non free flowing behaviour. No further differentiation is made. That means this measurement also does not give enough information to derive a powder's processability. Measurements of H are used mainly in powder metallurgy, and a transfer of this analysis to AM does not seem appropriate.

Dynamically measured values α_P , E_{av} and ψ_P capture the real process conditions much better, even though they are also limited to a predefined powder mass corresponding to 120 ml. Avalanche angle α_P and E_{av} are assumed to measure interparticle forces and correspond in a certain way with FR_C values. It was further assumed that ψ_P is mainly dependent on the powder's susceptibility to form agglomerations. The more agglomerations are formed, the rougher the bulk surface becomes.

However, the results lead to a more complex conclusion.

4. Results and discussion

Fast flow rates of Scalmalloy Batch III a and b, and V and SilmagAl Batch I and II correlate well with intermediate avalanche angles between $38^\circ < \alpha_P < 47^\circ$ and low energy values $E_{av} < 20 \frac{kJ}{kg}$. According to the pre-set estimation, low surface fractal values are estimated. This estimation is correct for Scalmalloy Batch III a and b and SilmagAl Batch I at a medium PSD range, with surface fractal values of $\psi_P = 2.4 - 2.5$. However, Scalmalloy Batch V and SilmagAl Batch II suggest that this conclusion is not generally valid. Both powder batches may indicate low interparticle forces, but interestingly also a high bulk surface roughness ψ_P . The explanation for that is given by the particle shape and particle size distribution evaluation. Both powder batches reveal in the PSD a high d50 value and a low Span. Although the particle shape is in both cases perfectly spheroidal, the rather monomodal PSD does not allow a reorganisation of the powder by forming a smooth bulk surface. Scalmalloy Batch II furthermore reveals a high ψ_P value with an intermediate d50 and a multi-modal PSD. Even if the PSD is rated appropriate, the particle shape is not ideal, though, leading to a rougher bulk surface. The particle shape of Scalmalloy Batch II is 50 % nodular. This result leads, on the one hand, to higher interparticle forces like friction or van der Waals forces that are reflected by an high α_P and an high E_{av} level, and on the other hand, it creates a more jagged bulk surface, simply because single particle surfaces are already jagged and rough. Scalmalloy Batch I exhibited, surprisingly, a low α_P and a low E_{av} level and the best surface fractal value of all tested powder batches of $\psi_P = 1.91$, although the PSD yielded the highest Span = 1.65 with a low d50 value. It was assumed that this constellation demonstrate the highest interparticle forces, as it is well known that such a high amount of fine particles leads to a greater tendency to form agglomerations and satellites. But the opposite was noted. One explanation gives the chemical analysis which showed that the oxygen content exceeds the allowed preset specification value about 60 %. Microsections of Scalmalloy Batch I do not show a high amount of inner porosity. It is therefore assumed that oxygen is mainly on the particles' surface by forming an isolation shell which reduces significantly interparticle forces.

All these results lead to the conclusion that the surface fractal value ψ_P of Scalmalloy and SilmagAl powders represents a reorganisation behaviour that is clearly dependent on particle shape, particle size distribution, surface oxide content and cohesiveness. This conclusion was also assumed, but not shown by Spierings in [89] for Fe and Ni based powders. It is also shown by these investigations, that Scalmalloy and SilmagAl powders flow behaviour is strongly dependent on used test environment. This outcome is in line with Seyda [111], who showed that Ti64 powders also flow very differently under various test methods.

Of all the completed analyses, the RPA delivers for Scalmalloy and SilmagAl the most informative value α_P , E_{av} , ψ_P of a powder to draw conclusions regarding suitability in SLM processes. For plastic powders, it is also assumed in [112] that a smooth bulk surface indicates a good intrinsic reorganisation behaviour of the powder, and here it is further concluded, that the better the powder rearranges itself after an avalanche, the better the powder behaves in the selective laser sintering process.

Bulk densities represent also a powder's reorganisation behaviour after free flowing or tapping. The apparent densities of Scalmalloy and SilmagAl batches vary between $49.5 \% \leq \rho_{ac} \leq 57 \%$. However, it indicates only the packing of the powder in cup with a volume of $V = 24.84 \text{ cm}^3$ after flowing through the Carney funnel. This method again does not capture the actual

4. Results and discussion

process close enough. The transferability of a powder's suitability for the SLM process is also invalid. A powder with a high apparent density, a high flowability and low interparticle forces rearranges completely differently if it is not surrounded by a cup. It simply flows easily in every direction on the platform during the process, and it rearranges far away from the measured high apparent density. The same applies for the tap density. Compressibility is only shown in the test environment. Moreover, no tapping or stimulation takes place during the powder application in used SLM processes, as mentioned above. However, the results of tap density analysis confirm qualitatively the cohesiveness estimations of E_{av} . Scalmalloy Batch I with a broad PSD leads to the highest tap density of 66.5 %. Low interparticle forces are measured ($E_{av} = 12.4$ kJ/kg), and the high Span = 1.65 with $d_{50} = 30$ μm allows a very high compression. Scalmalloy and SilmagAl batches with a medium PSD allow a higher compression to 62 % $\leq \rho_t \leq 65$ % compared to a narrower PSD at the same low avalanche energy level $E_{av} < 20$ kJ/kg because of their higher Span. The bulk densities of Scalmalloy and SilmagAl powders mirror well the different particle size distributions broad, medium and narrow regarding the morphology and interparticle forces.

Several publications have reported that the most commonly used PSD's for SLM processes have a range of 15 - 45 μm (e.g. in [113]). This study of Scalmalloy and SilmagAl powders widens the generally understood range, and the following conclusion can be made.

PS and PSD significantly influences the reorganisation and flow behaviour and therefore the processability. The lowest true layer thickness (see Equation: 2.7) should be limited by the coarsest particle. A multi-modal PSD and only spheroidal particle shapes should be aimed to get a smooth bulk surface. A broad PSD also needs to have an oxygen content high enough to prevent agglomerations. However, beyond its possibly good process-ability, a broad PSD with very low d_{10} values is rated as critical regarding industrial safety. Aluminium powder forms an explosive mixture of a wide range of metal-to-air ratios [65]. Static build-up and sparking during powder handling has to be avoided, which is more challenging the higher the content of fine particles ($PS < 20$ μm).

In general, it became obvious that numerous analyses are essential to understand and evaluating powder, and each characteristic is strongly dependent on the chosen atomising technique. Microstructural analysis showed, regarding suitability of the chosen atomising technique the following: Atomising processes used for Scalmalloy Batches I, IIIa and b are suitable regarding impurities, phases and porosity. The atomising technique used for Scalmalloy Batch II needs more modification to ensure a greater presence of spheroidal particles, most probably by reducing the oxygen content during atomising. Process of Scalmalloy Batch IV is definitely not suited as the atomising temperature is obviously lower than 600 °C, which creates a dissolution of coarse Al_3Sc primary particles (due to their size assumed to be already in the feedstock) impossible, also shown in [114]. The atomising process of Scalmalloy Batch V also needs more modification to reach the intended Sc and Zr content and to reduce the inner porosity.

It seems that atomising SilmagAl powders is much easier than atomising Scalmalloy. Microsections of SilmagAl Batch I do not exhibit the necessity of any modification, as they are

4. Results and discussion

free of any impurities, phases or porosity. The chemical analysis showed that minor modifications have to be made to reach the intended content of the major constituents and to reduce the small amount of inner porosity in SilmagAl Batch II. It is assumed that this goal is easily reachable.

Standard DIN 65122 mainly refers to test methods used in classic powder metallurgy press and sinter processes, but especially the flowability characterisation needs to be changed in this standard. The necessary flowability of a powder for the use in all available SLM processes is not yet defined. All flowability measurements only capture the flowability of the powder in their respective test environment. Also, for Al alloys, the oxygen content is supposed to be analysed more intensely than has been suggested.

FINDINGS:

- The most informative powder characteristics are anticipated to be morphology (particle shape), PSD, Span and chemical composition.
- PSD has to be validated by optical SEM analysis to exclude the misinterpretation of agglomerations as coarse powder particles.
- Dynamical flowability characteristics like ψ_p and α_p seem to reflect the powders morphology, PSD, interparticle forces and surface oxide content.
- It is also necessary to examine the powder for impurities.

4.2. Results and discussion of process analysis

An important step in any qualification is the definition of a robust and reliable process with appropriate parameters. The influence of process parameters on the ensuing material quality derived from AM of Scalmalloy and SilmagAl is presented and discussed. Fundamental investigations on single and multi-layer and weld traces for Scalmalloy Batch I gave important information about the microstructure of Scalmalloy. To evaluate the microstructure appropriately, the theoretical microstructural zones of Al weld beads out of SLM processes are resumed and explained with reference to the investigations. In principle, zones can be usefully differentiated as illustrated in Figure 4.3 useful.

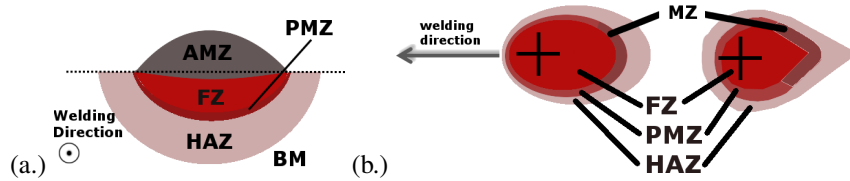


Figure 4.3.: Theoretical weld seam zones (a.) Side view and (b.) Top view of resulting microstructural zones at low (left side) and high (right side) scan speeds

The basis material (BM) is the area of the substrate plate which stays unaffected by the heat input of the laser. Typically chosen for processing Scalmalloy and SilmagAl are AlMg4.5Mn cast plates with a thickness of 10 to 25 mm. For the initial Scalmalloy single and multiple layer(s) scan test matrix on Platform P4, however KO8242 sheet material was used to allow welding between similarly composed Al alloys. Both AlMg4.5Mn cast and KO8242 sheet material have a significantly different grain size and structure than the AM material, which allows in the microseccional analysis an easy distinction between the two. Nevertheless, the microstructure of the base plate material is not further investigated in this thesis.

In the heat affected zone (HAZ), the peak temperature is $T < T_S$ and hence too low to melt the material but still high enough to affect the grains and microstructure significantly. Usually, the HAZ is considered as the zone that weakens the microstructure of Al alloys after welding due to a leap in hardness or strength in either way. Depending on composition, an embrittlement and hardness increase ensues, or the opposite is possible. Additional heat treatments may equalise the effect.

The partly melted zone (PMZ) is the area immediately outside the weld [39] where both liquidated and solidified material coexist. Aluminium alloys do not only melt above T_L , the onset melting already begins in between equilibrium T_S and T_L . The so called freezing range $\Delta T = (T_L - T_S)$ for Sc modified Al alloys increases significantly at a hyper-eutectic composition, as seen in the partial binary phase diagram in Figure 2.9. Magnesium as alloying component additionally influences Scalmalloy's melting point and hence T_S and T_L . Differences in solidus temperatures of binary AlSc ($\approx 665^\circ\text{C}$) and AlMg ($\approx 450^\circ\text{C}$) diagrams reveal a significant gap, which may lead to a large freezing range ΔT for the composition of Scalmalloy. A ternary system AlSiMg is investigated in [45] which leads to an estimation of $\Delta T \approx 60^\circ\text{C}$

4. Results and discussion

for SilmagAl. The PMZ is generally characterised by changes in grain size, orientation and morphology, and their formation is based on several different liquidation mechanism, as explained in the literature [39].

The mushy zone (MZ) is also a zone of coexisting already-solidified and still liquid areas. It is the region behind the melt pool where the solidification occurs. Its dimension and shape correspond to the viscosity of the melt and chosen scan speed. An increase in P_L/d_f ratio and scan speed leads to a tear drop rather than elliptically shaped melt pool and MZ, as to be seen on the right side in Figure 4.3. After solidification the MZ corresponds to the additive manufactured zone (AMZ) and -or the fusion zone (FZ).

The FZ describes the solidified zone of the melt pool where fusion to previous layers or scan traces takes place. The FZ transitions into the AMZ, which denotes the zone of the solidified and newly added material. The AMZ is only clearly detectable in the very last layer of a part or in single-layer investigations. In all other layers, the AMZ mixes with the FZ, PMZ or HAZ.

4.2.1. Single and multi-layer weld traces of Scalmalloy Batch I

Fundamental investigations of the melt and each weld seam formation were done on single and multi-layer welds out of Scalmalloy Batch I in a SLM environment. Microsectional analysis was carried out, and the aspect ratio A_N in Equation 2.3 was determined depending on different laser intensities and scan velocities.

The weld seam formation with their corresponding zones was initially investigated on Platform P4 with a laser power limit of 200W. It was investigated how the microstructure develops on a base plate at single and multiple layers on one single and multiple line scan paths. A 10 x 10 test matrix consisting of one line scan and one layer up to 10 line scans and 10 layers was analysed phenomenological and regarding aspect ratio. Chosen parameters are laser power $P_L = 195$ W, scan velocity of $v_s = 300$ mm/s, hatch distance of $h = 100$ μm and spot size $d_f = 100$ μm , which is resulting in a P_L/d_f ratio of 1.95 kW/mm. The high content of very fine particles and a $d_{50} = 29.90$ μm in Scalmalloy Batch I allows processing at very thin layer thicknesses. The layer thickness corresponds for single-layer investigations to the lowering of the built plate and was set to $z = 20$ μm . For multi-layer investigations, the powder filling factor is the important driver that defines the true layer thickness (see Equation 2.7 and 2.8). That factor leads to an increasing true layer thickness, d , over the first 10 layers from $z = 20$ $\mu\text{m} \leq d \leq d_i = 37$ μm .

Following cross-sections in Figures 4.4 - 4.6 are representative microsections of the test matrix and illustrate the formations of weld paths. They all reveal a very fine grain-structure after processing. Seven scans at one layer are displayed in Figure 4.5 and seven scans at five layers in 4.6. Both microsections are etched according to Barker to highlight the resulting fine grain structure and possibly areas of AMZ, FZ, PMZ or HAZ.

4. Results and discussion

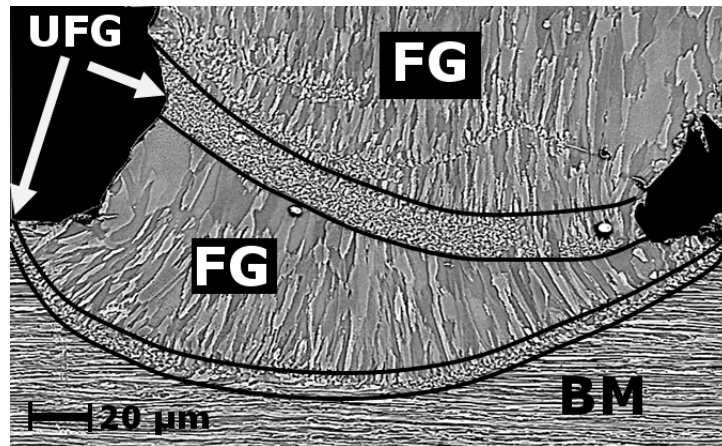


Figure 4.4.: Scanning electron microscope (SEM) analysis of Scalmalloy Batch I single trace and multi-layer weld seam formation

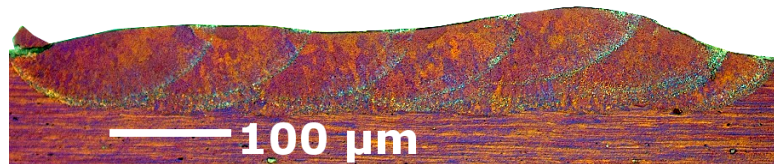


Figure 4.5.: Scalmalloy Batch I multi-traces and single layer weld seam formation

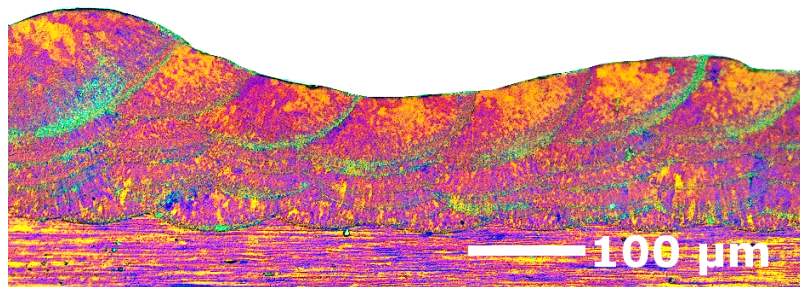


Figure 4.6.: Scalmalloy Batch I multi-traces and multi-layer weld seam formation

The grains in each weld developed in alternating bands of different grain sizes. These bands can be divided into equiaxed ultra-fine grains (UFG) in the FZ and/or PMZ and rather columnar fine grain (FG) areas in the FZ and/or AMZ (see microsection of one scan at multiple layers in Figure 4.4). A pronounced HAZ cannot be observed by microscopical analyses, but the zone must exist. As the grain size formation turned out to be more complex than initially assumed, further microsectional analyses of the grain size distribution and development were done and are given in Section 4.2.3. However, in a nutshell, the overall appearance of the weld

4. Results and discussion

formation is uniform, with an equal distribution of grains in the above-mentioned bands. No significant lack of fusion or hydrogen porosity was noticed in any of the 100 welds of the layer and scan traces test matrix. The transition to the base material is clearly visible in all three Figures 4.4 - 4.6 by a sudden change in grain size and orientation with no pronounced PMZ. Different important findings are drawn from these observations. Firstly, Scalmetal powder Batch I is processable. The melt's viscosity and the chosen scan speed of $v_s = 300$ mm/s at $P_L/d_f = 1.95$ kW/mm leads to a weld seam width range of $d_w = 150 \pm 20$ μ m. A resulting weld seam depth range of about $d_d = 65 \pm 15$ μ m leads to an aspect ratio $A_N = 0.44 \pm 0.06$ (see equation 2.3). This aspect ratio is significantly lower than 1 and hence corresponds to heat conduction welding mode.

And secondly, a consistent fusion between consecutive layers is realised and the estimated hatch of $h = 100$ μ m leads to an overlap which is sufficient to fuse single scan traces. The heat conductivity welding mode obviously creates a stable welding that leads to a dense microsection. Small dense and steady builds of only few scan traces and layers allow the conclusion that a high process stability is achievable by use of this parameter set.

FINDINGS:

- A suitable parameter set for Scalmetal Batches I that creates a homogenous fusion between scan traces and layers is given by $v_s = 300$ mm/s, $P_L = 195$ W, $h = 100$ μ m and $z = 20$ μ m and causes heat conductivity welding.
- Scalmetal Batch I solidifies in SLM by developing two alternating bands of UFG and rather columnar FG.

The tested parameters combination of 195 W and 300 mm/s cannot be transferred to an industrial environment as the resulting build rate of roughly 2.3 cm³/h is far too low. A resulting volume energy density is calculated at $d_i = 37$ μ m to $E_v = 167$ J/mm³.

To investigate the potential to increase the build rate significantly, additional tests on machine P2 were executed. Platform P2 is equipped with a higher laser power range up to 400 W at a spot diameter of $d_f = 100$ μ m but a stable use of only 370 W is guaranteed by the machine manufacturer. The tests on P2 followed two routes. On the one hand, it was tested whether the initial results out of P4 could be reproduced, and on the other hand, the direct influence of the increase of laser power and scan speed on the aspect ratio and phenomenological weld bead formation was investigated.

A total of eight builds were produced, four builds at $P_L/d_f = 1.95$ W and four at $P_L/d_f = 3.7$ kW/mm. The scan velocity was increased in four steps starting from $v_s = 300$ mm/s up to $v_s = 1200$ mm/s. Also, the lowering of the build plate was increased about 10 μ m to $z = 30$ μ m, whereas the hatch remained at $h = 100$ μ m. A lowering of $z = 30$ μ m leads over the first 10 layers to a processing layer thickness of $z = 30$ μ m $\leq d \leq d_i = 56$ μ m. As experienced in the previous tests, small dimensions of builds are enough to estimate the process performance; that is why five layers and five scan traces were chosen for the builds.

Eisen [29] describes an approach regarding the analysis of the formation of weld paths for the parameters identification of any new material. It is generally assumed that balling effects, described in Section 2.1.1, and any deviation from a homogenous clear weld path leads to

4. Results and discussion

non-suitable process parameters. The evaluation according to this approach was made with reference to the SEM pictures analysis of all eight weld paths before microsectional analysis. Figure 4.7 summarises all weld paths and highlights that except parameter combination $v_s = 300$ mm/s, $P_L = 370$ W all line scans reveal spattering and inherent spherical particles on the side and on the top surface of the weld seam. However, they are of different nature for either laser power stream $P_L = 195$ W or $P_L = 370$ W, as the welding mode differs.

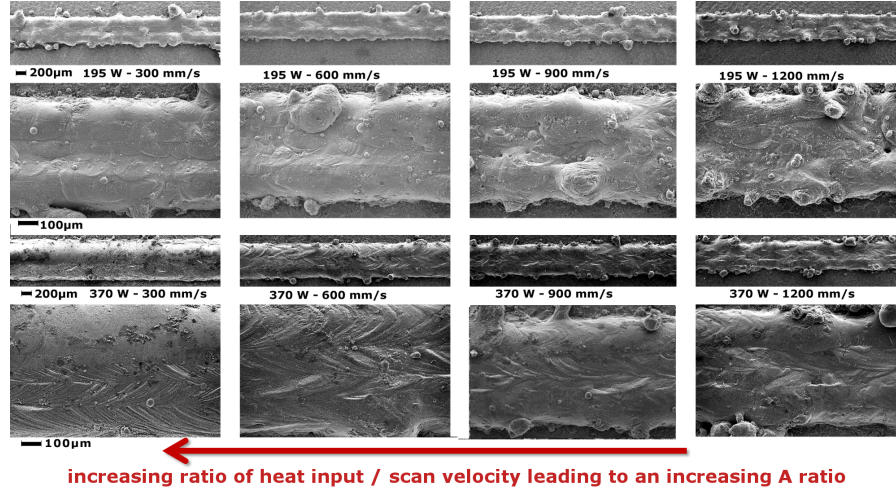


Figure 4.7.: Scalmaalloy multi-traces samples build out of Batch I

At $P_L = 195$ W a heat conductivity welding, which creates a shallow weld pool, is again assumed for all four tested scan velocities. A high thermal and surface gradient is created that leads to the Marangoni convection, as explained in Section 2.1.2. The so-induced turbulent flow can result further in ejection and spattering. The inherent spheres on the weld paths at $P_L = 195$ W and $v_s = 300$ and 600 mm/s are for this reason assumed to be spattering coming from the weld pool dynamics on the one hand and partly molten powder particles on the other hand.

Higher scan speeds $v_s = 900$ and 1200 mm/s decrease the heat input and cause balling effects due to an too early solidification of the melt. A continuous liquid formation of the weld path is furthermore not guaranteed, as the viscosity of the melt increases. That increased viscosity leads to high surface tension which results in a discontinuous solidification of the weld path. The more turbulent weld seam appearance with a higher weld surface roughness may confirm that an interrupted solidification process has taken place. A reduced energy input at $v_s = 900$ and 1200 mm/s leads, as expected, additionally to the rough weld seam appearance, to a visible decrease in weld seam width.

The welding mode at $P_L = 370$ W varies in dependency on the scan speed probably between all three modes; heat conductivity, transition or keyhole welding. The best visual appearance of all eight welds is seen at a low scan speed of $v_s = 300$ mm/s. Only very few fine, partly molten powder particles are visible.

4. Results and discussion

Balling phenomena, inherent spheres and partly molten powder particles on the weld seam sides increase with increasing scan velocity, however, and the overall weld seam appearance changes to more turbulent. That is an indication that the weld mode changes to either transition or conductivity welding and the same balling mechanism occurs as in for $P_L = 195\text{ W}$. Another finding is, that for both power levels, different weld morphologies develop. Examples are presented in Figure 4.8 of two builds at either 195 W and 300 mm/s or 370 W and 1200 mm/s. This figure highlights the scan paths, welding direction and hatch distance of all five scans and their resulting difference in the shape of the melt pool. At 370 W the weld seam track is teardrop formed and representative for all tested velocity configurations (300 mm/s, 600 mm/s, 900 mm/s and 1200 mm/s) as the shape does not change macroscopically. However, the weld track is at 195 W and 300 mm/s elliptically formed and changes with increased scan speed to no visible weld track morphology. This finding additionally confirms that for parameter sets, that contain higher scan speeds, the weld path is not equal and stretches in interrupted sequences. An interpretation regarding a suitable parameter set seems difficult with only an inspection of the weld paths. A microsectional analysis needs to confirm the assumptions about welding modes and weld quality.

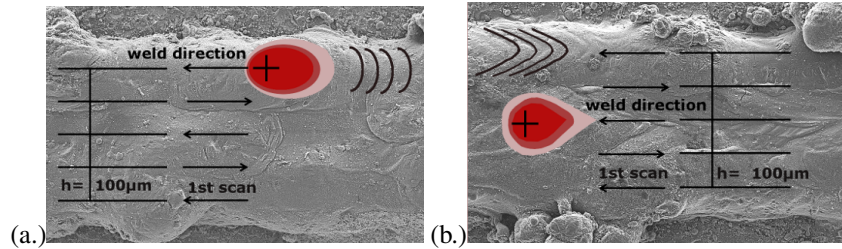


Figure 4.8.: Scanning electron microscope (SEM) images of Scalmaalloy Batch I multi-traces samples (a.) Weld seam track is elliptical shaped at 200 W and 300 mm/s and (b.) Weld seam track is teardrop shaped at 370 W and 1200 mm/s

FINDINGS:

- The top view weld pool analysis revealed that the weld pool is differently shaped at 370 W and 195 W and the influence of the scan velocity at 370W seems less significant than at 195W.
- The weld trace analysis showed at 370W and 300 mm/s the most homogenous formation of the scan paths, with low amount of inherent particles or spatter.

Cross-sections of all eight builds are seen in Figure 4.9, which reflects the observed macroscopically significant differences in the weld seam morphology. Firstly, the welding mode at 195 W on P2 is most obviously again conductivity mode, and the resulting build at 300 mm/s is very consistent to the initial builds on P4 in Figure 4.6.

However, a laser power of 370 W leads to a significant deeper penetration welding in the transition or keyhole mode. An increase of scan speed at both power levels leads to a decrease in weld seam depth. The weld seam widths are at 195 W in the range of $d_w = 150 \pm 25$

4. Results and discussion

μm for low scan speeds and around $d_w = 125 \pm 25 \mu\text{m}$ at high scan velocities. At 370 W is the range of d_w approximately between $d_w = 175 \pm 25 \mu\text{m}$ for high v_s values and roughly $d_w = 200 - 300 \mu\text{m}$ for lower scan speeds. The aspect ratio of the final scan tracks of the last layer are measurable on these etched microsections and a conclusion to the corresponding welding mode can be made. Determined weld seam depths are depicted as in Figure 4.10. The trendline shows that the deep penetration welding mode at 370 W and 300 mm/s leads to an aspect ratio $A_N > 2$ which corresponds to keyhole welding mode and decreases over the transition mode with $1 \leq A_N \leq 1.5$ to finally conduction mode at scan velocity of 1200 mm/s with an aspect ratio $A_N < 1$. A deep cavity is created during keyhole welding, and an excessive remelting of previous layers is the result. Beam traps as illustrated in Figure 2.2, lead to a higher absorption of the energy input and a long-lasting deep weld pool. Such a weld pool increases the possibility of evaporation of low melting alloying elements, which results in high weld pool dynamics. The emerging vapour and plasma prevent a constant and equal heat input and the keyhole may become unstable. If the keyhole collapses, the solidification becomes interrupted over the weld pool height, and gas filled pores develop at the bottom of the keyhole. Such a keyhole collapsed and a pore is seen on the microsection at 370 W and 300 mm/s. Such an unpredictable solidification of the weld pool is not desirable, as the aim of a suitable parameter set is to generate a microsection with the lowest possible porosity. Laser power of 195 W leads in the investigated scan speed range to no change in the welding mode. It is in any case conductivity welding with an aspect ratio of $A_N < 1$ which increases with decreasing scan speed but never exceeds $A_N = 1$. The increase of z and therefore increased true layer thickness of $z = 30 \mu\text{m} \leq d \leq d_i = 56 \mu\text{m}$ does not majorly influence the conductivity mode and resulting d_d . Builds at 195 W and 300 mm/s and 370 W and 1200 mm/s result both in conductivity welding mode and a very similar microsection. It can be assumed that both parameters combinations will lead to a stable process.

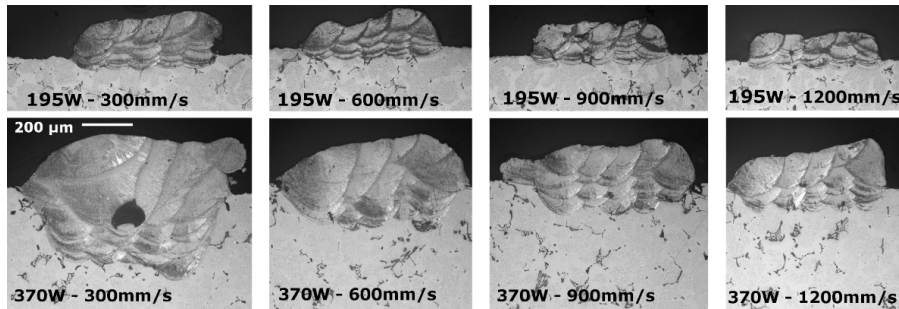


Figure 4.9.: Cross-section of multi-layer and scan traces builds for different parameters

4. Results and discussion

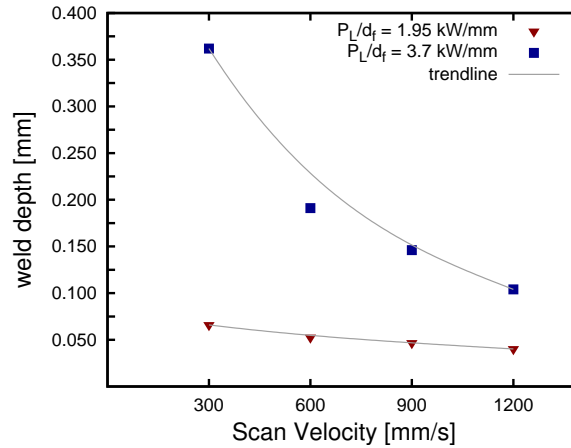


Figure 4.10.: Dependency of laser power to focus diameter ratio P_L/d_f on weld depth d_d at different scan velocities v_s on single and multi-layer welds of AM Scalmetalloy Batch I

All volume energy densities (see equations 2.2), for the investigated eight parameter sets, are given in Table 4.8. For the sake of convenience, the true layer thickness is set in the calculation to $d_i = 56 \mu\text{m}$. If the conclusion out of the microsectional analysis is that parameter combinations 195 W and 300 mm/s and 370 W and 1200 mm/s are leading to a stable process, the operating window according to E_V is quite broad, from 55 J/mm^3 to 116 J/mm^3 . If E_V of initial tests on Platform P4 with an $d_i = 37 \mu\text{m}$ enters into these considerations, the window even broadens from 55 J/mm^3 to 167 J/mm^3 . However, the upper limit of $E_V = 167 \text{ J/mm}^3$ corresponds for $d_i = 56 \mu\text{m}$ and $P_L = 370 \text{ W}$ to a scan velocity of $v_s \approx 400 \text{ mm/s}$, and this result again leads to a welding mode that is either transition or keyhole welding, as shown by the trendline in resulting weld seam depth in diagram 4.10. But especially keyhole welding does not seem desirable according to these fundamental investigations to manufacture a high quality and homogenous microstructure. Of course, the parameter combination can obviously be adapted to reach for an equal E_V level always heat conductivity welding, but the general conclusion that a single volume energy density value leads to a stable process cannot be made. The welding mode is decisive, and can be most reliably estimated by a simple evaluation of the P_L/d_f ratio, dependent on v_s and resulting d_d and d_w , as proved by these investigations or as already done for years in conventional LBW of Al alloys, reported in [34].

4. Results and discussion

Table 4.8.: Volume energy density E_v comparison for different laser power levels

| E_v [J/mm ³] | | v_s | | | |
|----------------------------|-------|----------|----------|----------|-----------|
| | | 300 mm/s | 600 mm/s | 900 mm/s | 1200 mm/s |
| P_L | 195 W | 116 | 58 | 39 | 29 |
| | 370 W | 220 | 110 | 73 | 55 |

FINDINGS:

- Initial builds on Platform P4 were successfully reproduced on Platform P2.
- Builds at 195 W are welded in the heat conductivity mode for all tested scan velocities.
- The microsectional analysis of builds at 370 W indicate the progression of heat conductivity to deeper penetration welding with decreasing scan speed.
- Both parameter sets, 195 W at 300 mm/s and 370 W at 1200 mm/s result in a similar and dense microstructure.
- The keyhole welding mode at 370 W and 300 mm/s leads to an excessive remelting of previous layers and a turbulent weld pool formation that may lead to porosity as the keyhole can collapse.
- The microsectional analysis is inconsistent with the weld trace morphology analysis. The best process parameter combination to exhibit a sufficient fusion to previous layers and scan paths is not 370 W at 300 mm/s but both combinations 195 W at 300 mm/s and 370 W at 1200 mm/s.
- An increase of lowering the build plate from $z = 20 \mu\text{m}$ to $z = 30 \mu\text{m}$ also leads to a conductivity welding mode and a very similar build morphology and microstructure at the same v_s and P_L .
- An operating window for Scalmetalloy cannot be described by E_v , as important information about the welding mode is missing.

4.2.2. Influence of process parameters on porosity

Scalmetalloy Batch I

Section 4.2.1 demonstrates that each welding mode can lead to spattering, inherent, partly molten powder particles and insufficient solidification. As heat conductivity welding was identified to be the most promising welding mode for processing Scalmetalloy, the influence of hatch distance and scan speed was analysed in more detail in that mode. Cubes with a dimension of $(10 \times 10 \times 10) \text{ mm}^3$ were built for microsectional analysis on Platform P1 at $P_L = 195$

4. Results and discussion

W and $z = 30 \mu\text{m}$ with an increasing hatch $h = 50 \mu\text{m}$ to $200 \mu\text{m}$ at increasing scan speeds from $v_s = 200 \text{ mm/s}$ to 400 mm/s . Polished cross sections of the cubes in figure 4.11 were analysed regarding porosity over the full height of 10 mm . The results of this test matrix were also reported in [4]. An increase of the hatch leads to an increasing porosity, which rises even more if v_s is simultaneously increased. The increase of v_s from 200 mm/s to 400 mm/s solely at one h level does not have a major influence on porosity as an increasing or decreasing hatch distance. Porosity increases indeed with a rising v_s but not in the same range as shown for an increasing hatch distance. Although the chosen scan velocity range of 200 to 400 mm/s was quite narrow, a trend was nevertheless noted. Porosity morphology changes from tiny spherical pores at $h = 50 \mu\text{m}$ and low scan speed of $v_s = 200 \text{ mm/s}$ to an irregular formed lack of fusion porosity at $h = 200 \mu\text{m}$ and $v_s = 400 \text{ mm/s}$. The reason for that change is on the one hand that at a low hatch distance, more heat is transferred into each single weld path (as the overlap to the previous scan becomes higher), an excessive remelting of previous scan traces increases emerging vapour, and solidification occurs by gas porosity formation. On the other hand, it leads a too low heat input at high hatches $h = 200 \mu\text{m}$ to an early solidification of each scan path, and no sufficient overlap with previous weld traces is achieved which produces the noticed lack of fusion porosity. The best parameter combination which reveals the lowest porosity is again found at $h = 100 \mu\text{m}$ and $v_s = 300 \text{ mm/s}$.

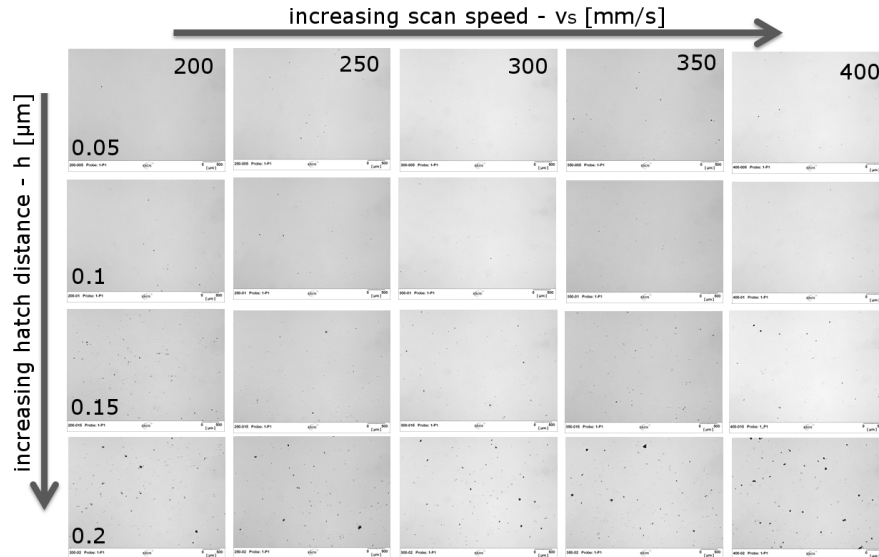


Figure 4.11.: Influence of hatch distance and scan speed on Scalmalloy powder Batch I, processed at 195 W and $z = 30 \mu\text{m}$

Another test program was set up on Platform P2 to investigate the limits of heat conductivity welding at an laser power level of $P_L = 370 \text{ W}$. The only changing variable here was the scan velocity v_s , which was increased from 600 to 2100 mm/s for the build-up of tensile test coupons. Exemplary microsections are show in Figure 4.12 and reveal that at 370 W

4. Results and discussion

and 1200 mm/s a higher amount of porosity occurs than at 195 W and 300 mm/s. The whole microsection at each shown v_s is honeycombed with very small gas filled pores. At higher scan speeds of $v_s > 1700$ mm/s, again a significant increase in lack of fusion porosity is noticed. Although the chosen parameters lead to conductivity welding, the process is obviously more vigorous at 370 W than at 195 W.

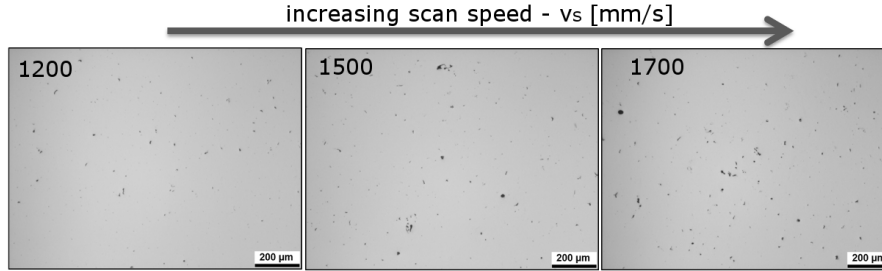


Figure 4.12.: Influence of increasing scan speed on Scalmalloy powder Batch I, processed at $P_L = 370$ W, $h = 100$ μm and $z = 30$ μm

Scalmalloy Batch II

Identified suitable process parameters for Scalmalloy Batch I were tested to see whether they are transferable to a second powder batch, Scalmalloy Batch II, and another Platform P5. This platform also offers the option of a laser focus diameter of $d_f = 100$ μm . Again, cubes were built and equally analysed as Scalmalloy Batch I cubes. A severe lack of fusion porosity was found for both parameter options 195 W at 300 mm/s and 370 W at 1200 mm/s. Etched microsection of the cube manufactured at 195 W at 300 mm/s in Figure 4.13 on the right-hand side, highlights, in examples for both parameter options, the highly turbulent welding process, which results in non-homogenous uniform scan paths. Spatter at a diameter of 200 μm occurred and remained unmolten in the microsection. The P_L/d_f ratios for both scan speeds do not offer an energy input that is sufficient for Scalmalloy powder Batch II.

An additional test matrix containing again cubic builds at different v_s and P_L variations, leads to a more suitable parameter combination of $P_L = 400$ W at 800 mm/s as shown on the left side in Figure 4.13. A uniform weld track formation was reached, and only two inconsistencies in the form of lack of fusion were found over the whole microsection of the cube. An increase of the P_L/d_f from 1.95 to 4 kW/mm and simultaneously decrease of v_s (1200 to 800 mm/s) offered an energy input that is high enough to create a fusion to the layers below and previous scan tracks. The final scan trace of the last layer on the top surface of each cube reveal that this parameter combination still leads to a heat conductivity welding mode with an aspect ratio $A_N < 1$. This observation leads consequently to the conclusion that the differences of the powder characteristics between Scalmalloy Batch I and II causes a complete different energy transfer in the process.

4. Results and discussion

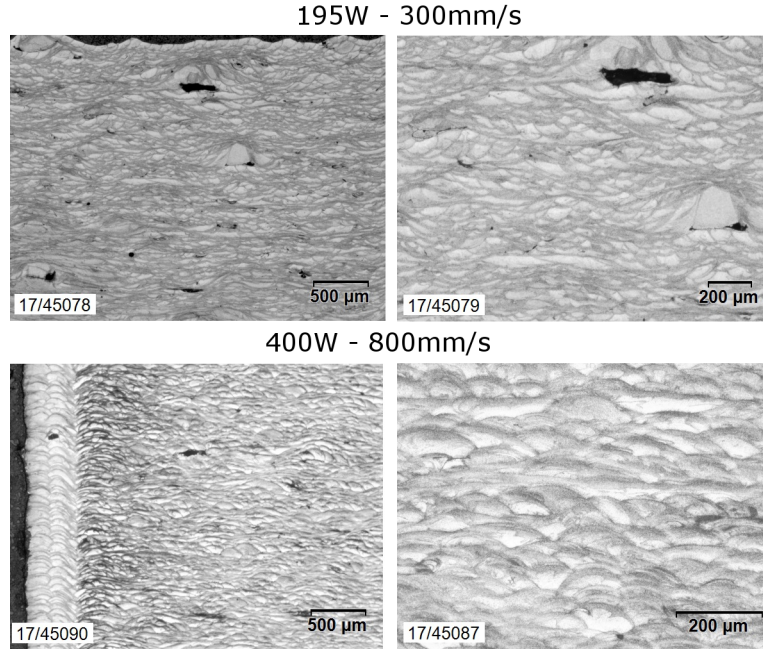


Figure 4.13.: Resulting microstructures of processed Scalmalloy Batch II powder at $h = 100 \mu\text{m}$ and $z = 30 \mu\text{m}$ but different P_L and v_s levels

Scalmalloy Batch IIIb

An initial test for Scalmalloy Batch IIIb was done on Platform P2 to check whether one of the suitable parameter combinations for Batch I ($h = 100 \mu\text{m}$, $z = 30 \mu\text{m}$, $P_L = 370 \text{ W}$ and $v_s = 1600 \text{ mm/s}$), is also applicable for Batch IIIb. The microsectional analysis showed that only a fine and equally distributed porosity is formed, leading to the conclusion that the energy transfer while processing Scalmalloy Batch III b, seems similar to that of Scalmalloy Batch I. In consequence, the transfer of this parameter set to Batch III b is possible. Several powder characteristics of both powder batches also match very well, as discussed in Section 4.1.7, which also supports this argument.

Scalmalloy Batch V

The processibility of the fifth Scalmalloy powder batch was tested again on cubes on Platform P5 at $h = 100 \mu\text{m}$, $z = 30 \mu\text{m}$ and varying P_L and v_s . Figure 4.14 contains an abstract of all tested microsections of the cubes. No tested parameter combination led to a sufficient fusion-welding process and a high density. Every cube, except cube additive manufactured at 400 W and 650 mm/s, features severe cracks perpendicular to the layers. Solidification occurs in non-connected sequences and a penetration and fusion to previous scan traces and layers could not be realised. Only at ratio $P_L/d_f = 4.0$ and 650 mm/s is the energy input more suf-

4. Results and discussion

ficient to create a fusion to subsequent layers. Nevertheless, in this cube, high porosity was also noticed that did not allow the use of this parameter for further material-characterising investigations. A welding mode cannot be associated to any of the used parameter set, as it is mainly a mixture of all three modes that makes the resulting microstructure this turbulent. Again, it is concluded that the powder characteristics of Scalmalloy Batch V influences the process response significantly, as also experienced for Batch II.

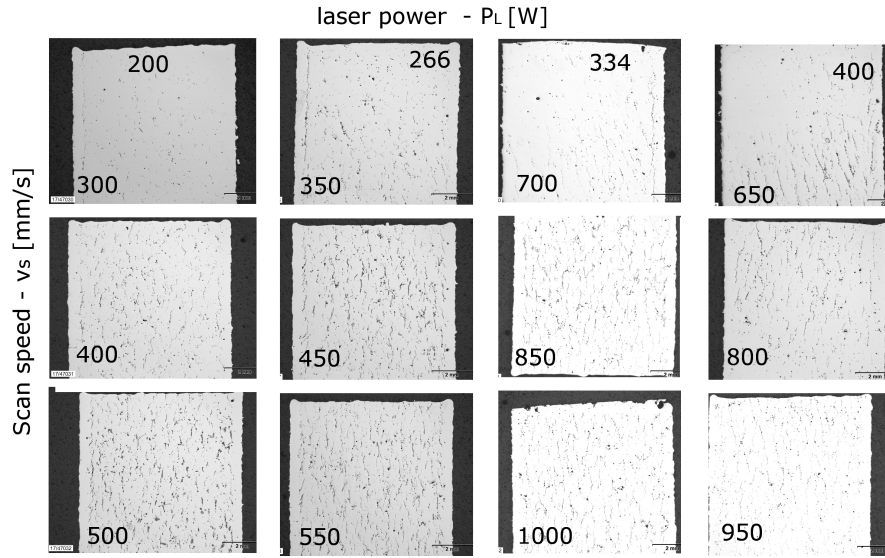


Figure 4.14.: Resulting microstructures of processed Scalmalloy Batch II powder at $h = 100 \mu\text{m}$ and $z = 30 \mu\text{m}$ but different P_L and v_s levels

SilmagAl Batch I and II

Different test matrices with varying P_L , v_s and h have been built and investigated for both batches. An operating window was narrowed down to $z = 50 \mu\text{m}$, $P_L = 400 \text{ W}$ at $v_s = 1320 \text{ mm/s}$ to obtain the highest build rates at a sufficient high quality of the microstructure. The melt pool development differs compared to Scalmalloy and creates a weld path width of $350 \mu\text{m} \leq d_w \leq 450 \mu\text{m}$ which allows to broaden the hatch. Figure 4.15 illustrates an etched example out of these test matrices for SilmagAl Batch I. SilmagAl Batch I and II were manufactured in a heat conductivity welding mode which results in a uniform microstructure. Both powder batches obviously formed after recoating on the platform a very smooth and even bulk surface. Only very few laserbeam traps were generated and observed which caused few gaseous pores. The generated broad weld bead allowed to increase the hatch distance to $h = 150 \mu\text{m}$.

4. Results and discussion

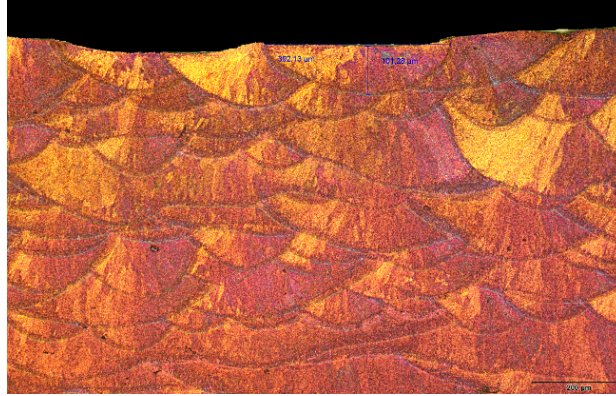


Figure 4.15.: Resulting microstructures of processed SilmagAl powder Batch I at $h = 150 \mu\text{m}$, $z = 50 \mu\text{m}$, $P_L = 400 \text{ W}$ and $v_s = 1320 \text{ mm/s}$ forming a weld bead width of $d_w \approx 400 \mu\text{m}$

FINDINGS:

- It was shown that for Scalmalloy Batches I, II and III b and SilmagAl Batches I and II an operating parameter set was developed that is sufficient in reaching a high microstructural density.
- Scalmallo powder Batch I was processable at different P_L and scan speed v_s levels.
- Scalmalloy powder Batch II is very sensitive to small deviation from the identified process parameter window; process pores are likely to occur in complex builds.
- No suitable parameter window was identified for Scalmalloy powder Batch V as severe cracking in z-direction was obtained.
- Both SilmagAl Batches I and II were processable in the same process parameter window.

4.2.3. Microstructural response

Scalmalloy Batch I

A scanning electron microscope image in Figure 4.4 of additive manufactured Scalmalloy, showing multiple AM layers on one scan trace, demonstrates that the microstructure develops in areas that differ in grain size, as reported in [9, 10]. An UFG band alternates a FG band with a periodicity of 10 to 15 μm . Cubic builds from Platform P4, manufactured at $h = 100 \mu\text{m}$, $z = 20 \mu\text{m}$, $P_L = 195 \text{ W}$ and $v_s = 300 \text{ mm/s}$, were investigated by use of TEM to investigate these bands in more detail. No additional heat treatment was performed, the investigated condition corresponds to as-built. The TEM image in Figure 4.16 a. highlights a clear differentiation between both bands, as reported in [10]. The UFG's are equiaxed at a size of around 500 - 1000 nm, FG's are more columnar formed at a longest axis of around 10 μm . The formation of alternating bands are in line with the analysis of Spierings in [7] for AM material build with another different Scalmalloy powder batch.

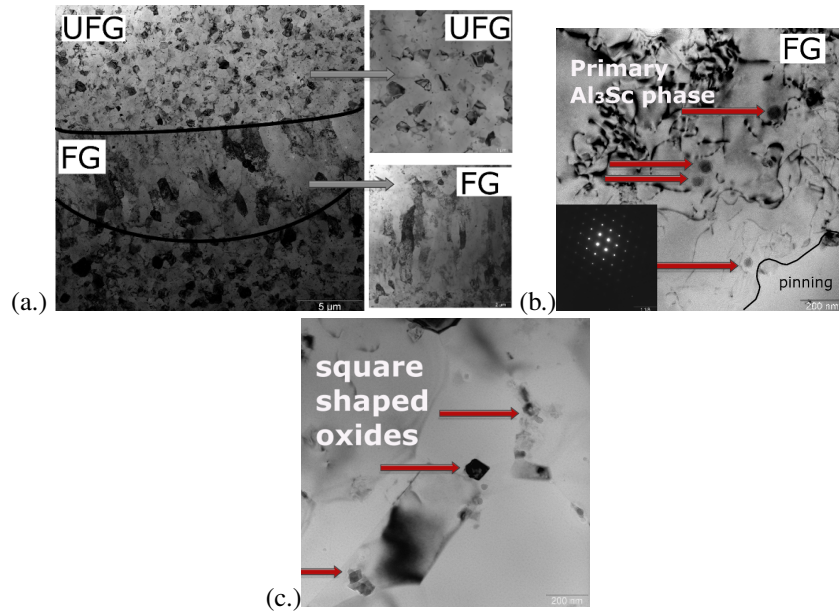


Figure 4.16.: (a.) Bright field TEM images of Scalmalloy manufactured at $h = 100 \mu\text{m}$, $z = 20 \mu\text{m}$, $P_L = 195 \text{ W}$ and $v_s = 300 \text{ mm/s}$ in as-built condition; (b.) primary Al_3Sc phase and partly high distribution of dislocations (c.) shaped oxides on grain boundaries and within grains

The microstructural analysis did not reveal an obvious distinction between HAZ, PMZ and FZ, as known from conventional LBW of Sc modified Al alloys, for example in [115]. A HAZ, as described in weld metallurgy, leads to a coarsening and grain growth [116] but there is no

4. Results and discussion

sign of such conventional HAZ or PMZ with detectable grain morphology changes around the FZ to the BM. However, a sharp separation between the UFG and FG zone is noticed without any indication of transformation from band to the other by continuously increasing grain sizes. If a PMZ between layers or scan paths exists, cannot be identified, since the overall microstructure of Scalmalloy consists of only the two alternating UFG and FG bands. Hence it can be assumed, that the solidification process develops in two stages. The first stage is the heterogeneous nucleation of grains at the interface of the melt to the build plate or previous solidified layers. The melt is here exposed to the highest cooling rates. A high thermal gradient and a high undercooling lead to the UFG zone of equiaxed grains in either MZ, PMZ or FZ. Initiator for grain growth are impurities in the melt which act as nucleation points. $\text{Al}_3\text{Sc}_{(1-x)}\text{Zr}_x$ nuclei, for example, have a perfect match to the aluminium matrix and can act as initiators for grain growth and even encourage the growth of equiaxed grains. It is assumed that this first stage can be described as some kind of "Big Bang" solidification, as assumed as one possible mechanism for the equiaxed grain growth in castings in [117]. However, contrary to casting, the grains do not float into the remaining melt, as the melt does not stay liquid long enough. The solidification time is too short for any grain movements which could lead to the formation of the observed FG zone.

When the undercooling and temperature gradient decrease, columnar grain growth starts in the direction of the thermal gradient and then the FG zone develops. The welding of the following layers and consequently certain amount of remelting leads to a new PMZ, MZ and FZ. In the PMZ the freezing range and the cooling rate are at this stage important. If the cooling rate remains high enough to keep a solid solution supersaturated by Sc, no change in strength will be noticed. However, a significantly decreasing cooling rate will cause the loss of coherency of Al_3Sc and increases the possibility of coarsening and an early segregation of primary Al_3Sc particles. A drop in strength or ductility will be noticed. Primary Al_3Sc particles do not lead to any strengthening effect; moreover, they weaken the microstructure and act like impurities, [118, 117, 119]. Any subsequent layer scanning, exposes the AMZ to an intrinsic heat treatment according to [8, 120]. This heat input has a duration of approximately less than one second. However, $\text{Al}_3\text{Sc}_{(1-x)}\text{Zr}_x$ and AlSi precipitations are strongly temperature and time dependent (see [117]). It is therefore assumed, that although the cooling rates indeed decrease, they are still high enough to prevent an early segregation of undesired primary phases in Scalmalloy. It is furthermore estimated, that no significant effect of the intrinsic heat treatment (by subsequent layer scanning) is noticeable in SLM of Scalmalloy and SilmagAl.

In both areas, UFG and FG, particles and precipitations are present, that differ in composition, size and shape. They are located as either intra or intergranular in both zones but a slightly higher amount is found in the FG zone. These particles, especially on the grain boundaries are assumed to prevent grain growth by the Zener pinning effect, as indicated in Figure 4.16 b. This effect describes how particles counteract grain boundary movements. Small particles may prevent the grain boundary motion by exerting a pinning pressure [121]. In [122] was shown that the particles shape and distribution strongly influence grain growth behaviour due to the Zener drag. These particles or intermetallic phases that may occur in Scalmalloy are either $\text{Al}_3(\text{Sc}, \text{Zr})$, Al_6Mn , Al_3Mg_2 , Al_5Mg_8 or oxides of different compositions, as highlighted in Figure 4.16c. An exact determination of the oxides and phases is complicated, as they are often embedded in a particle of a different phase. Hyde [119] has shown, for example, that below T_L primary Al_3Sc particles nucleate heterogeneously on oxides within the melt.

4. Results and discussion

In general influences a high content of oxides in a material the material properties significantly. The strength level increases, but at the expense of ductility. Oxides in an AM microstructure occur for two reasons. Oxygen layers on either powder particles or subjacent scan paths are broken into pieces during welding and due to Marangoni forces stirred into the material, according to [7] not homogeneously and preferably closer to the UFG band. All used platforms process at a remaining oxygen content of 500 to 2000 ppm which is fairly enough for Al alloys to form thin oxygen layers on the top surface of each weld path during the process. However, temperatures in the process are assumed to exceed 2500 °C [7] which is high enough to disrupt these oxygen layers. However probably not high enough to partly evaporate them (assumed in [66]), as Spierings [120] has shown by simulation that the peak heat input duration is very short of only a few 10^{-4} seconds.

Another important finding is, that coarse particles of the equilibrium $\text{Al}_3(\text{Sc,Zr})$ phase do exist in both bands of the analysed microstructural extract, at a size range of 20 - 80 nm, as can be seen in Figure 4.16b. However, no signs of nonequilibrium $\text{L}_{12}\text{Al}_3(\text{Sc,Zr})$ particles were determined, neither in the diffraction patterns nor in the bright field images. The image also reveals that partly a high distribution of dislocations was detectable in both bands.

The frequency of the $\text{Al}_3(\text{Sc,Zr})$ primary phase tends to occur in the FG rather than in the UFG zone, contrary to the observations of Spierings in [7]. This phase is either a remaining primary phase that was already present in the powder particles or is newly developed during the process. In [7] is shown by Scheil simulation, that the $\text{Al}_3(\text{Sc,Zr})$ phase dissolves at ≈ 800 °C. This finding leads to the assumption that these $\text{Al}_3(\text{Sc,Zr})$ particles were developed during the SLM process.

As no signs of the secondary $\text{L}_{12}\text{Al}_3(\text{Sc,Zr})$ phase were found, one can furthermore confirm the assumption that an intrinsic heat treatment, which leads to a notable in situ ageing process, does not occur at the chosen parameter combination for Scalmetalloy Batch I. In [123], the solidification for a powder metallurgical manufactured Sc modified Al alloy is explained. The same effects are observed for these test cases.

A general interaction of scan speed and cooling rate on the grain size development is made in [34] which showed, that the competitive grain growth is faster the higher the scan speed is.

SilmagAl

Test cubes of SilmagAl Batch I were built at $z = 50 \mu\text{m}$, $P_L = 400 \text{ W}$, $v_s = 1320 \text{ mm/s}$ and $h = 150 \mu\text{m}$ on Platform P5. Microsection are presented in Figure 4.17 with top view of the scan traces and side view of the weld seams. Both microsections were analysed in the as-built condition and etched according to Barker to highlight the grain structure, the formation and fusion of weld paths or layers. Solidification occurred obviously similar to the above mentioned mechanism for Scalmetalloy. The CS leads to the a very fine eutectic microstructure, which is quite contrary to conventional AlSiMg castings with an α dendritic matrix that includes large eutectic Si particles. However, as CS is dependent on the concentration of minor constituents, which are de facto reduced in SilmagAl, a less significant effect is noticed compared to Scalmetalloys microstructure. Columnar grain growth is noted, as seen in Figure 4.17, however, no pronounced alternating bands as observed in AM Scalmetalloy were detected.

Vilaro [124] has shown, that the microstructure of as built AlSi10Mg is very heterogeneous with segregations in the HAZ that are very rich of Mg and Si. Such segregations are also

4. Results and discussion

assumed to be seen in the etched microsection in Figure 4.18 but not confirmed by EDX mapping. Next to such enriched zones, a HAZ is noted at higher magnifications, but no further analysis and precise grain size measurements were done for SilmagAl.

It can nevertheless be summarised, that the chosen parameters form an appropriate fusion between scan paths and layers. Occasionally, deeper penetration welding effects are noticed, which lead to minor porosity. The dominant welding mode is also heat conductivity welding, with an aspect ratio $A_N < 1$ as measured for Scalmalloy. The melt of SilmagAl distributes homogeneously and a very uniform microsection can be achieved by SLM of SilmagAl.

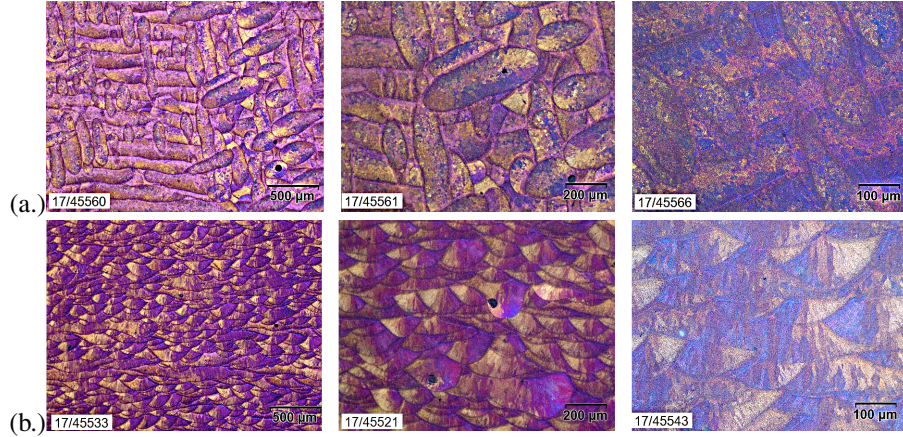


Figure 4.17.: SilmagAl microsections of test cubes built at $z = 50 \mu\text{m}$, $P_L = 400 \text{ W}$, $v_s = 1320 \text{ mm/s}$, $h = 150 \mu\text{m}$ etched according to Barker (a.) top view highlighting scan traces and (b.) side view highlighting weld seam and grain formation

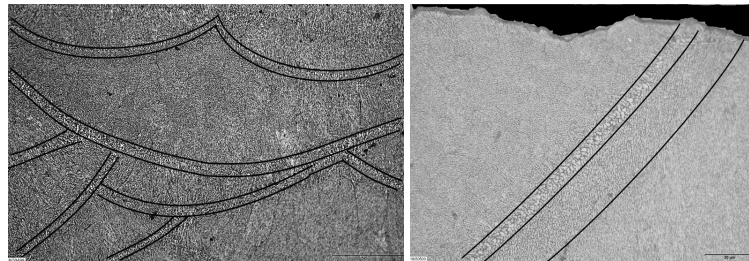


Figure 4.18.: Conventional etched microsection of SilmagAl test cubes, built at $z = 50 \mu\text{m}$, $P_L = 400 \text{ W}$, $v_s = 1320 \text{ mm/s}$, $h = 150 \mu\text{m}$ revealing particle enriched zones between eutectic Al-cells

FINDINGS:

- Scalmalloy forms during SLM a microstructure which consists of alternating equiaxed UFG and columnar FG bands.

4. Results and discussion

- Coarse particles of the equilibrium $\text{Al}_3(\text{Sc}, \text{Zr})$ phase do exist in both bands.
- SilmagAl forms a very fine eutectic microstructure of columnar grains with segregations in the HAZ.

4.2.4. Influence of process parameter on static tensile strength

In addition to the microsectional analysis, the evaluation of the evolution of the static tensile strength behavior is necessary. The aim is to proof whether the parameters which lead microscopically to a sufficient microstructure also lead to the desired ST strength. Tests for Scalmalloy Batch I and II and SilmagAl Batch I were performed as described in section 3.4.4 on additive manufactured cylinders that were milled to the shape of B4 x 20, B5 x 25 or B6 x 30.

Scalmalloy Batch I

Cylinders were built at constant $P_L = 370 \text{ W}$, $h = 100 \text{ }\mu\text{m}$, $z = 30 \text{ }\mu\text{m}$ and varying $v_s = 600 - 2100 \text{ mm/s}$ on P2. Each data point in Figure 4.19 represents the average value of three or five specimens tested in z-direction. All specimen were equally heat treated at $325 \text{ }^\circ\text{C}$. Arrows in that diagram mark the gradient of the strength evolution over the increasing scan speed. Distinct areas are enclosed, highlighting the v_s level at which the strength or elongation plateaus, respectively.

The trend until $v_s = 900 \text{ mm/s}$ corresponds, according to the microsectional analysis, to parameters that lead to deep penetration and the keyhole welding mode. Excessive remelting of previous layers strongly influences the microstructure by a mixture of gas porosity and possible in situ over ageing. Scan velocities between $v_s = 900 - 1300 \text{ mm/s}$ lead to a transition welding mode with again turbulent microstructures. A stable energy transfer leading to heat conductivity welding mode is reached between $1300 - 1700 \text{ mm/s}$. In the region of this plateau a maximum average value of $R_m = 522 \text{ MPa}$, $R_{p0.2} = 499 \text{ MPa}$ and $A = 11\%$ is reached. After this plateau, the heat input decreases and results in a lack of fusion between scan paths and layers, and these defects again cause a drop in strength and elongation to failure.

A direct comparison of the static strength of additive manufactured Scalmalloy Batch I in heat conductivity welding mode at different laser powers and scan speeds, is given in Figure 4.20. The data points correspond to the average value of five milled and heat-treated ($325 \text{ }^\circ\text{C}$) specimens tested in z- direction. Parameter combinations are $h = 100 \text{ }\mu\text{m}$, $z = 30 \text{ }\mu\text{m}$ and either $P_L = 195 \text{ W}$ and $v_s = 1300 \text{ mm/s}$ or $P_L = 370 \text{ W}$ and $v_s = 1600 \text{ mm/s}$. Both R_m and $R_{p0.2}$ are on the same strength level of $R_m = 520 \pm 2 \text{ MPa}$ and $R_{p0.2} = 499 \pm 0.5 \text{ MPa}$ but a decreases in elongation about 3% is noticed at $P_L = 370 \text{ W}$ and $v_s = 1600 \text{ mm/s}$ compared to $P_L = 195 \text{ W}$ and $v_s = 1300 \text{ mm/s}$.

It is therewith shown, that the build rate can be increased for Scalmalloy Batch I by a factor of 5 at a constant strength level, see Figure 4.20. That is crucial for the industrialisation of this Al alloy, admittedly at the expense of ductility.

4. Results and discussion

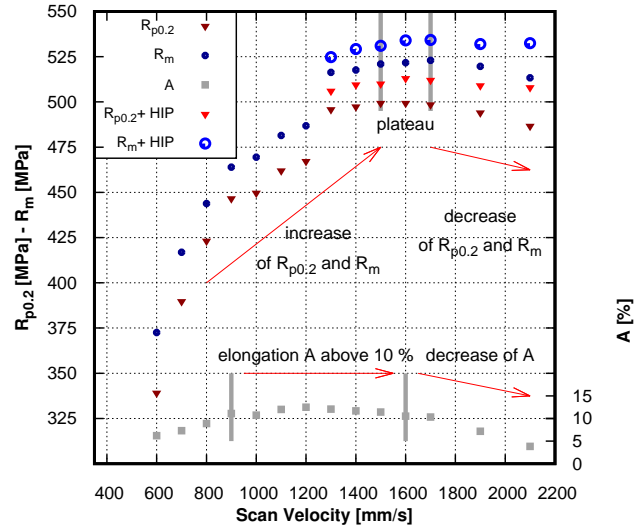


Figure 4.19.: Influence of parameter set and heat treatment on Scalmaalloy samples build out of Batch I

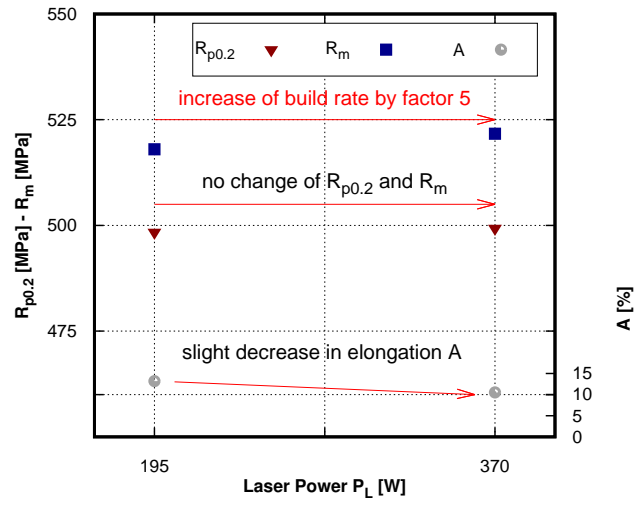


Figure 4.20.: Comparison of parameter set $h = 100 \mu\text{m}$, $z = 30 \mu\text{m}$ and either $P_L = 195 \text{ W}$ and $v_s = 300 \text{ mm/s}$ or $P_L = 370 \text{ W}$ and $v_s = 1600 \text{ mm/s}$ regarding static strength response for Scalmaalloy Batch I

4. Results and discussion

Scalmalloy Batch II

Two parameter options for processing Scalmalloy Batch II are compared to each other regarding static strength response in heat treated and heat treated and HIP'ed condition in Figure 4.21. Data points correlate to average values of three milled specimens that were manufactured either at 195 W and 300 mm/s (B4 x 20), referred to as 1 - HT and 1 - HT + HIP, or $P_L = 400$ W at 800 mm/s (B6 x 30), referred to as 2 - HT and 2- HT + HIP. A non-homogenous microstructure resulting from parameter set 1 with high lack of fusion porosity and balling effects, as displayed in Figure 4.13, leads to lower strength levels than the microstructure out of parameter set 2. However, both parameter options lead to the same elongation level at $A = 10$ %. The build rate difference between both sets is approximately a factor of 2.7. An influence of the additional HIP step is discussed in section 4.3.

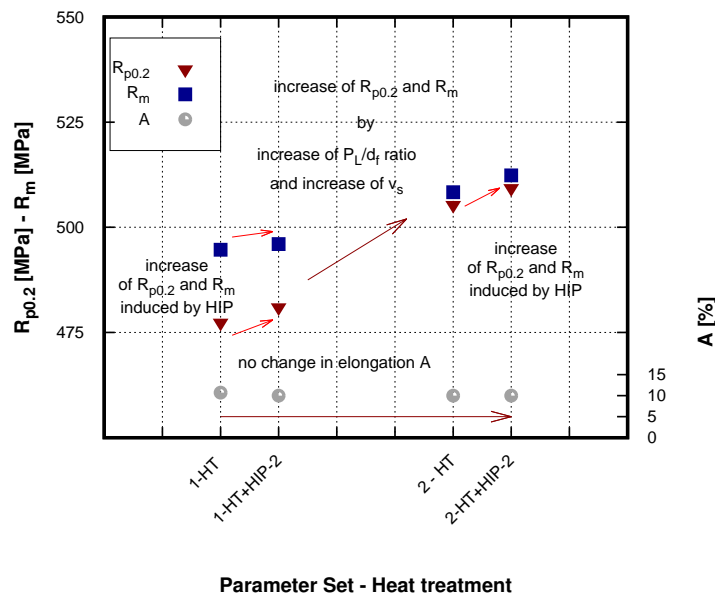


Figure 4.21.: Comparison of parameter set $h = 100 \mu\text{m}$, $z = 30 \mu\text{m}$ and either $P_L = 195 \text{ W}$ and $v_s = 300 \text{ mm/s}$ or $P_L = 400 \text{ W}$ and $v_s = 800 \text{ mm/s}$ regarding static strength response for Scalmalloy Batch II

SilmagAl Batch I

Microsectional analysis (see Figure 4.15) determines that the most influencing parameter for processing SilmagAl is the hatch distance. For this reason, seven different hatches, h , were used to build three test coupons, respectively, at constant $z = 50 \mu\text{m}$, $P_L = 400 \text{ W}$ and $v_s = 1320 \text{ mm/s}$. All specimens were milled to the final shape of B6 x 30 and tested in z -direction after additional ageing at 165°C for 7h.

4. Results and discussion

A R_m level of 447 MPa, $R_{p0.2} = 287$ MPa at an elongation of $A = 8\%$ was reached at a hatch distance of $h = 160 \mu\text{m}$. The significant decrease in strength indicates that the best working hatch distance is $h \leq 160 \mu\text{m}$. A hatch distance level $h = 150 \mu\text{m}$ was added to the parameter test, as the drop in strength at $h = 0.147 \mu\text{m}$ of the initial test campaign was caused by severe porosity that became visible on the fracture surface. The second tests revealed that at $h = 150$ and $160 \mu\text{m}$, the same strength level is reached, which corresponds to the observed dense microstructure in figure 4.15.

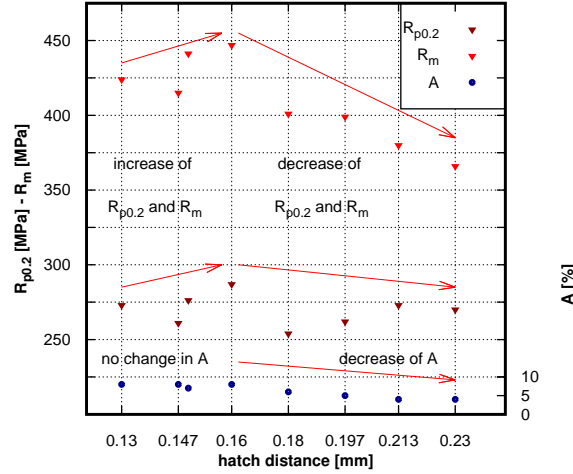


Figure 4.22.: Influence of hatch distance on $R_{p0.2}$, R_m and A for samples build with SilmagAl Batch I at 1370 mm/s

FINDINGS:

- The static tensile response after processing Scalmaalloy Batch I resulted after heat treatment of 325°C in high strength values above $R_m = 500$ MPa.
- A significant change in build rate for Scalmaalloy Batch I led to the same static strength level with a slight decrease of A .
- Scalmaalloy Batch II led in the same heat treatment condition on a different parameter set to a comparable static strength level as Scalmaalloy Batch I.
- The static tensile response after processing SilmagAl Batch I resulted in strength values above $R_m = 400$ MPa in aged condition.
- The static strength response of processing SilmagAl is mainly driven by the hatch distance h .
- A close dependency between processability and different powder characteristics became obvious.

4. Results and discussion

In the following Table 4.9 all parameters used for each alloy and powder batch are summarised, respectively, for the material characterising builds in Section 4.4.

Table 4.9.: Fixed process Parameter Sets 1-5 with corresponding Scalmalloy and SilmagAl powder Batch

| Set | Powder Batch | z [μm] | P_L [W] | v_s [mm/s] | h [μm] |
|-----|-------------------|-----------------------|-----------|-------------------------|-----------------------|
| 1 | Scalmalloy I | 20 or 30 | 195-200 | 300 | 100 |
| 2 | Scalmalloy II | 30 | 400 | 800 | 100 |
| 3 | Scalmalloy I, IIb | 30 | 370 | 1600 | 100 |
| 4 | Scalmalloy II | 60 | — | — | 100 |
| 5 | SilmagAl I, II | 50 | 375-400 | 1320-1370 | 150 |

4.3. Results and discussion of post process heat treatments

Scalmalloy

The test specimen used in Section 4.2.3, analysed by TEM, were additionally heat treated at 300 °C for 4 hours and then analysed again by use of TEM. The grain structure did not change after annealing and reveal still alternating UFG and FG bands, as displayed in Figure 4.23 a. Even the distribution of dislocations in both zones remains unaffected. Intermetallic phases (like equilibrium $\text{Al}_3(\text{Sc,Zr})$ phase), precipitations and oxides containing Sc, Zr or Mg, are still present in the microstructure. However, a very recognisable difference was seen on their distribution and location. They are no longer homogeneously distributed; moreover, the grain boundaries are now decorated in both zones, UFG and FG, by these coarser particles. The widely spread detected β phase is in some cases even organised in chains along the grain boundaries. This arrangement of the β phase is not desirable regarding corrosion resistance, (see explanation for influence of Mg as alloying element in Section 2.2.1). Nonetheless, the exact identification of the β phase, particles or oxides by EDS on the grain boundary was not completed.

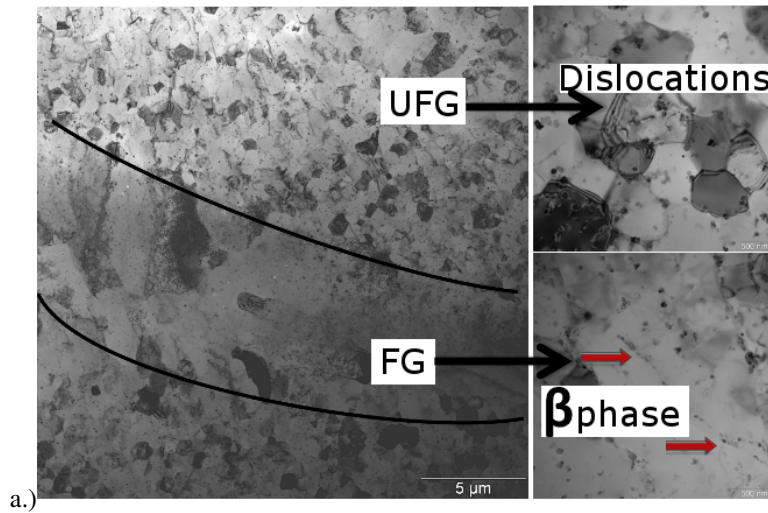


Figure 4.23.: Bright field TEM images of Scalmalloy Batch I manufactured at $P_L = 195$ W, $h = 100$ μm, $z = 20$ μm and $v_s = 300$ mm/s after ageing at 325 °C/4; Dislocations in UFG band and β phase on grain boundaries in FG band

The focus of this TEM analysis was to find precipitations that lead to the observed higher strength values between the as-built and aged conditions, (see section 4.4.3). Very small, homogeneously distributed precipitations were found in both bands in bright field and dark field images in Figure 4.24. Reflections in the SAED pattern correspond to the nonequilib-

4. Results and discussion

rium particles of the ordered L_{12} crystal structure $Al_3(Sc_{(1-x)},Zr_x)$ and proof that the desired precipitations do exist. Their size is very small and of only a few nanometres. It was not possible to determine their dimensions precisely, but they are assumed to have a mean diameter of around 1 - 5 nm. Although in both conditions, as-built and after ageing, the equilibrium $Al_3(Sc,Zr)$ phase exists, remained an important fraction of Sc and Zr in the supersaturated solid solution and precipitated during ageing. Their uniform distribution leads to the noticed high strength increase after heat treatment.

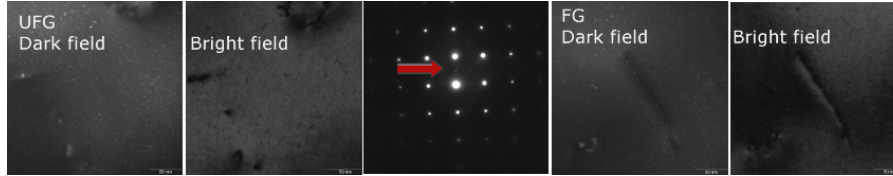


Figure 4.24.: Four bright and dark field images of $Al_3(Sc_{(1-x)},Zr_x)$ precipitations in UFG and FG band - approved by SAED pattern in between all four images

It would be interesting to detect the volume fraction of primary and secondary precipitations to estimate how much Sc leads to the precipitation strengthening effect, but these investigations lie beyond the scope of this thesis. Only an estimation what the overall Sc content is given by a comparison of ST strengths in both conditions: as-built and after ageing. Figure 4.25 illustrates this effect by analysing specimen in as-built condition, after ageing $325\text{ }^{\circ}\text{C} / 4\text{h}$ and $325\text{ }^{\circ}\text{C} / 4\text{h} + 325\text{ }^{\circ}\text{C} / 4\text{h} / 2000\text{bar}$. Each data point corresponds to the mean value of three specimens, tested in z-direction, manufactured out of Scalmetalloy Batch II on Platform P5 at $P_L = 40\text{ OW}$, $h = 100\text{ }\mu\text{m}$, $z = 30\text{ }\mu\text{m}$ and $v_s = 800\text{ mm/s}$. The elongation decreases about 5 % from 15 % to 10 % with an increase of $R_{p0.2}$ of about 185 MPa and R_m of about 142 MPa. A HIP step at $325\text{ }^{\circ}\text{C} / 4\text{h} / 2000\text{bar}$ in addition to $325\text{ }^{\circ}\text{C} / 4\text{h}$, leads to another slight increase of 5 MPa in $R_{p0.2}$ and 4 MPa in R_m . It is possible that this minor increase occurs because of the increased overall ageing time of 8 h, compared to simple ageing for 4h. It has been shown in [6] that peak age hardening for a different AM Scalmetalloy is reached at $325\text{ }^{\circ}\text{C}$ after 5 h and that no overageing could be noticed until an ageing duration of 20 hours. However, AM test specimens out of powder Batch III b reveal for the same overall ageing time of 6 h at either $320\text{ }^{\circ}\text{C} / 2\text{h}$ and $325\text{ }^{\circ}\text{C} / 4\text{h}$ or $320\text{ }^{\circ}\text{C} / 2\text{h}$ and $325\text{ }^{\circ}\text{C} / 4\text{h} / 1000\text{bar}$ a difference of 8MPa in $R_{p0.2}$ and 12 MPa in R_m . Obviously, is this increase very small, and due to the low number of tested specimens, it is statistically not covered; nevertheless, this slight increase can be traced back to the added pressure of 1000bar at $325\text{ }^{\circ}\text{C}$ over 4 h.

4. Results and discussion

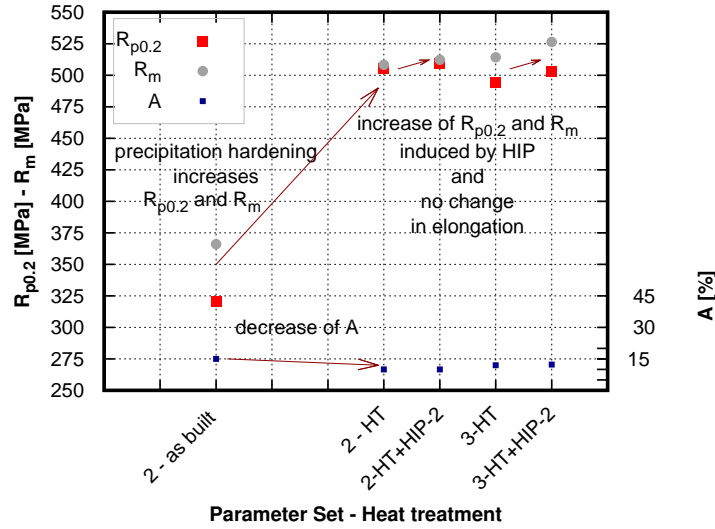


Figure 4.25.: Static strength response of Scalmalloy Batch II manufactured on Platform P5 at $P_L = 400$ W, $h = 100$ μ m, $z = 30$ μ m and $v_s = 800$ mm/s for the as-built condition, aged at 325 $^{\circ}$ C / 4 and aged at 325 $^{\circ}$ C / 4 + 325 $^{\circ}$ C / 4 / 2000bar

Although Scalmalloy powder Batch II did not develop to its full potential, as discussed in section 4.4.7, the massive influence of the precipitation strengthening is shown. The extent to which both other effects, grain boundary and solid solution strengthening, individually contribute to strengthening can hardly be estimated. The only conclusion that can be made is, that all three effects are simultaneously interacting with each other in an incredibly complex manner. The effects estimated to be most dominant are grain size and precipitation hardening. The distribution of $Al_3(Sc_{(1-x)}, Zr_x)$ precipitations in additive manufactured Scalmalloy is also discussed in the literature. Jäggle [8, 125] has investigated samples provided out of the test series used in this thesis. Two different powder batches, and hence two different AM materials were analysed by atom probe tomography to determine the distribution of precipitations and their composition, since a significant drop in strength was noted between these two materials. His analysis showed that $Al_3(Sc_{(1-x)}, Zr_x)$, Al_6Mn and Mg-rich (assumed to be $Mg_{17}Al_{12}$) precipitations are in the microstructure. Scandium-rich precipitations were measured to have a radius of 0.5-3nm which corresponds very well with the TEM analysis mentioned above. However, Jäggle furthermore identified particle free zones in each material of a different width. Materials, revealing a lower yield strength, have particle free zone of 70nm instead of 38nm for the reference high strength material. The uniformity and distribution of UFG and FG bands also differ significantly between both materials. The reference material has a very uniform alternating distribution, but the other samples show a rather turbulent microstructure with a smaller fraction of the equiaxed UFG zone. Hardness measurements in both bands, UFG and

4. Results and discussion

FG, do not indicate a significant difference. However, his conclusion, that the fraction of UFG is correlated to the powder atomising process, is incorrect. It is rather the combination of powder and parameters, that was not ideally chosen and lead to a microstructure of non-uniform alternating UFG and FG bands. Still, the smaller fraction of UFG bands can indeed lead to a drop in yield strength.

In [120], $\text{Al}_3(\text{Sc,Zr})$ particles are found of the same size range already in as-built condition, which is assumed to be the result of an intrinsic heat treatment by processing at very low scan speeds of $v_s = 170 \text{ mm/s}$. However, at higher scan speeds in as-built condition, also no evidence for intragranular $\text{Al}_3(\text{Sc,Zr})$ precipitations was found but an increase of dislocations and a decrease of grain size ($1.1 \mu\text{m} - 600 \text{ nm}$) were noted in the UFG zone. Spierings noticed only a slight dependency of scan velocity on hardness, and the yield strength stays more or less unaffected by different scan velocities.

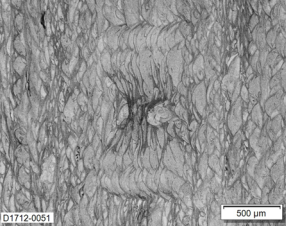
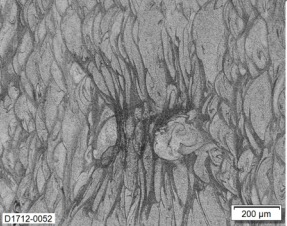
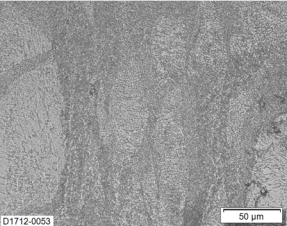
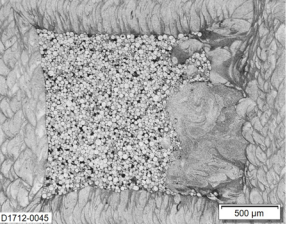
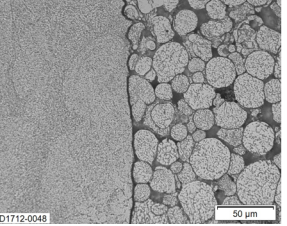
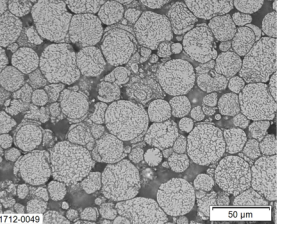
Stress relaxation or heat resistance tests at elevated temperatures gave an indication of the needed pressure for hot isostatic pressing at $300^\circ\text{C} - 325^\circ\text{C}$. Cylindrical and milled test specimens, in B6 x 30 shape, built on Platform P5 of SilmagAl Batch I at $P_L = 195 \text{ W}$, $h = 100 \mu\text{m}$, $z = 30 \mu\text{m}$ and $v_s = 300 \text{ mm/s}$, were individually loaded at elevated temperatures in z-direction with an initial standard load and a constant strain of 1 mm/min . The initial load for samples heated to 150°C was set to 300 MPa , and after only 1 hour a remaining load lower than 100 MPa was obtained. However, an immediate creeping was noted when testing at 300°C and an initial load of 100 MPa (see Appendix A.19) and a remaining load of less than 20 MPa was measured after only 5 minutes. It can hence be assumed that a HIP process at $300^\circ\text{C} - 325^\circ\text{C}$ and $1000 \text{ bar} - 2000 \text{ bar}$ does influence the microstructure of Scalmetalloy.

Hot isostatic pressing of Scalmetalloy was investigated further in the project PROCEED in co-operation with Ariane Group. Cylindrical test coupons with artificially induced defects were manufactured with Scalmetalloy Batch II on Platform P5 at $P_L = 400 \text{ W}$, $h = 100 \mu\text{m}$, $z = 30 \mu\text{m}$ and $v_s = 800 \text{ mm/s}$ and analysed by CT scans before and after HIP. Four different defect sizes, summarised in Table 4.10, were geometrically modelled and embedded in the cylinders. Computer tomography scans were done with a resolution of $90 \mu\text{m}$ before and after HIP and each defect size was measured (see Appendix A.18). In Table 4.10, microsections are also included for both defects, leading to the lowest and highest volume reduction of 54% and 94% , respectively. The etched microsections reveal quite well that creep processes during HIP occurred. A change in grain morphology is noticed on the boundaries of the artificial defects. They seem rather elongated no pronounced UFG and FG bands anymore. The powder particles, that remained in the defect after HIP, fell out partly during the microsectional preparation. They did not go into solution with the surrounding material. For the bigger defect, with an initial size of height and diameter of 2 mm , many particles in the defect remained glued to the AM surrounding material or each other, and it is remarkable shown that between these powder particles and AM matrix no fusion process started. They remained non-interconnected and were only deformed and pressed together. A sharp boundary between powder particles and AM material is formed with an oxygen layer, a so called kissing bond. Hot isostatic pressing at $325^\circ\text{C} / 4 \text{ h} / 1000 \text{ bar}$ indeed reduced defect sizes, but did not repair the microstructure through complete fusion processes. It can be rather interpreted as some kind of gluing, and non-powder-filled spherical pores may be glued together quite well, but a lack of fusion poros-

4. Results and discussion

ity, which accompanies most probably an oxygen layer, forms kissing bonds only after HIP at 325 °C / 4h / 1000 bar.

Table 4.10.: Microsections of Scalmaalloy after HIP with artificial defects

| Defect dimension Height x Diameter | Volume reduction after HIP | | |
|---------------------------------------|--|--|---|
| 1.5 mm x 1.5 mm | 59 % | | |
| 0.6 mm x 1 mm | 94% | | |
| |  |  |  |
| 0.8 mm x 0.8 mm | 91% | | |
| 2 mm x 2 mm | 54% | | |
| |  |  |  |

4. Results and discussion

SilmagAl

The capability for precipitation hardening of as-built SilmagAl Batch I AM material was investigated in more detail. Milled cylindrical test specimens, B6 x 30, were built on Platform P5 at $z = 50 \mu\text{m}$, $P_L = 400\text{W}$, $v_s = 1250\text{mm/s}$, $h = 150\mu\text{m}$ and aged at 165°C for 2 - 7 h. Three specimens were tested for each temperature level, and Figure 4.26 reveals that a plateau between 4 and 6 h was achieved with no further increase in strength. The elongation stayed rather unaffected in a range between 5.8 and 7 % but after 6 h decreases both the R_m and $R_{p0.2}$ level.

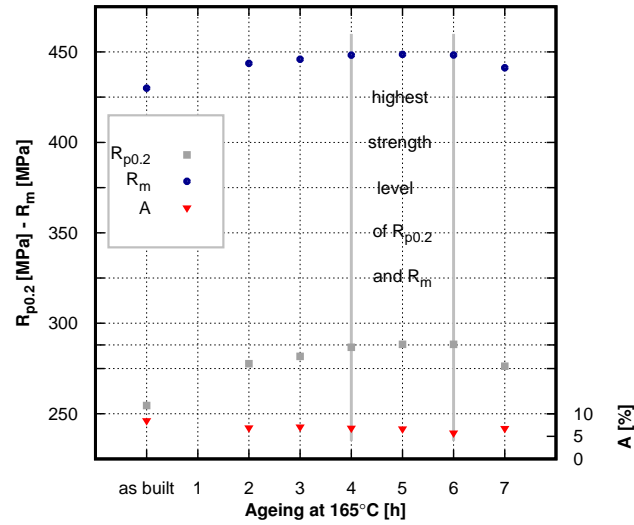


Figure 4.26.: Influence of increasing age hardening duration at 165°C on R_m , $R_{p0.2}$ and (A) in SilmagAl

FINDINGS:

- An ageing step for Scalmalloy at 325°C (4 - 8 h) revealed that precipitation hardening caused by $\text{Al}_3(\text{Sc}_{(1-x)}, \text{Zr}_x)$ particles occurs and is sufficient to create a high strength level.
- The homogenously distributed β phase in as-built condition of Scalmalloy diffused to grain boundaries after ageing, partly even organised in continuous chains.
- Hot isostatic pressing do not activate any diffusion processes in Scalmalloy, kissing bonds may occur depending on defect dimension.
- Ageing at 165°C causes precipitation hardening in SilmagAl at a favorable duration between 4 and 6 h.

4.4. Results and discussion of material characterisation

4.4.1. Result and discussion: density

The mean density obtained by the computation method depending on the composition of each Scalmaalloy and SilmagAl powder batch was measured as follows:

$$\rho_{Scalmaalloy} = 2.66 \frac{g}{cm^3} \quad (4.1)$$

$$\rho_{SilmagAl} = 2.67 \frac{g}{cm^3} \quad (4.2)$$

Hot isostatic pressed cubes for AM Scalmaalloy and SilmagAl out of powder Batch I were also analysed regarding density by the principle of Archimedes. Both methods confirm each other, even though also in the HIP condition a low residual porosity (below 0.05 %) has to be assumed. For the sake of convenience, no more density evaluations were performed, as a rounded density to two decimal places seems sufficient.

However, a detailed porosity analysis on the basis of measurements according to Archimedes and optical evaluation of microsections, as proposed by [126], was omitted. Inaccuracies of both measurement methods tend to warp the result, especially as the porosity is expected to be below 0.05 %. Minor errors in measurement have a significant influence. One error in Archimedes measurements can be caused, for example, by air bubbles adhering to the samples' rough as-built surface, which causes an additional buoyancy. However, milling specimens for smoothen the surface to avoid adherent air bubbles would possibly remove sub-surface porosity, which makes any result less meaningful. Optical evaluation of porosity is strongly dependent on the chosen resolution and the microsectional plane or predetermined position on the micrograph. No such optical measurement procedure is qualified yet as a quality indicator for metal materials to determine final acceptance criteria. Hence, the microsections' porosity was only evaluated qualitatively rather than quantitatively within this thesis.

FINDINGS:

- The density of Scalmaalloy and SilmagAl is quite low compared to the most common used Al-alloy 2024 with a density of $\rho = 2.78 \frac{g}{cm^3}$.

4.4.2. Results and discussion: corrosion

Both Al-alloys, Scalmaalloy and SilmagAl, have been tested regarding their susceptibility to AIC in the corrosive medium NaCl for 24 h and 30 days. The sample sizes are described in Section 3.4.3. Specimens were optical analysed regarding evolution, morphology and intensity of pits, partly also by use of SEM and microsections. AA5083 sheet material was tested and analysed simultaneously in the same test environment, to secure that the test conditions were maintained. The resulting corrosive attack to the AA5083 test specimens corresponded to their commonly known behaviour, see Figure A.20. Hence, the test can be considered appropriately performed.

4. Results and discussion

Testing according to ASTM G44 [102], with alternating periods of dipping into corrosive medium for 10 min and drying for 50 min, is considered to be a rather conservative approach compared to in aerospace commonly used salt spray tests. Specimens are kept wet during salt spray tests, and that procedure does not allow an appropriate activation of corrosion mechanism. Only the transition between the wet and the drying period causes a corrosion flow as only then local spots develop which contain a highly concentrated corrosive medium. The locally higher concentration favours the attack on grain boundaries. The ASTM G44 is rated as a test which imitates environmental conditions in aircrafts quite closely.

Scalmalloy test specimens show a minor corrosive attack after AIC testing. Small pits with a size ($< 50 \mu\text{m}$) are observed. No large-scale equal material removal is caused. Most of the milled surface of the specimen stayed intact, shown in Figure 4.27. The analysis of the microsections of the specimens were done to investigate if intergranular corrosion took place but only very flat troughs were found. This means, no intergranular corrosion along grain boundaries took place in this specific test environment. If a material finally exhibits a corrosive susceptibility, depends on the requirements of allowed number and size of pits for a certain area which is most often evaluated by comparing to conventional used other alloys. Hence, can be stated that compared to AA5083, Scalmalloy show a minor corrosive attack in this unloaded test condition.

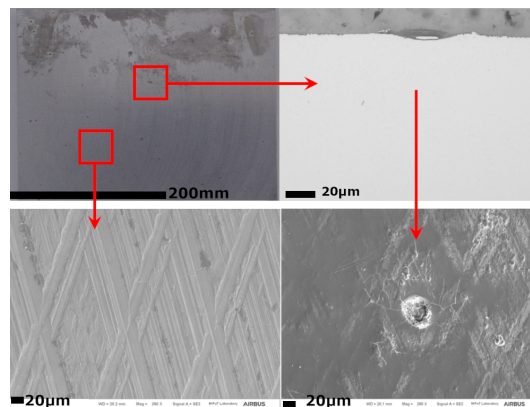


Figure 4.27.: Minor pitting attack on a milled surface of Scalmaalloy powder Batch II samples manufactured at $P_L = 400$ W, $h = 100$ μm , $z = 30$ μm and $v_s = 800$ mm/s; P5; aged at 325 $^{\circ}\text{C}/4\text{h} + 325$ $^{\circ}\text{C}/4\text{h}/2000\text{bar}$ and sensitised at 120 $^{\circ}\text{C} / 168\text{h}$

SilmagAl test specimens revealed an increased corrosive attack after testing. The number of pits is as increased as their dimensions. Additionally, cracks were observed which are elongated in xy-direction, parallel to layers. Both, cracks and pits have a length or diameter of $\leq 300 \mu\text{m}$, as illustrated in Figure 4.28. The microsectional analysis revealed the increased dimensions of the pits compared to Scalmalloy, but SilmagAl also did not reveal any intergranular attack in this test environment. Hence, SilmagAl is rated intermediate susceptible to pitting.

4. Results and discussion

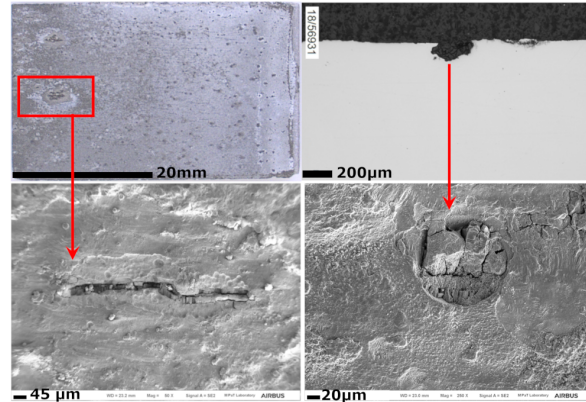


Figure 4.28.: Pitting attack on a milled surface of SilmagAl powder Batch II samples manufactured at $P_L = 400\text{W}$, $h = 150\mu\text{m}$, $z = 50\mu\text{m}$ and $v_s = 1320\text{ mm/s}$; P5; annealed at $540\text{ }^\circ\text{C} / 2\text{ h} / 1000\text{ bar} + 550\text{ }^\circ\text{C}/1\text{h} + \text{WQ} + 165\text{ }^\circ\text{C} / 7\text{h}$

Stress corrosion cracking tests followed for both Al-alloys under the same conditions according to ASTM G44 [102] by additionally applying loads at a level of 90 % of R_m . The results are summarised in Table 4.11.

Two specimens, manufactured with Scalmaalloy powder Batch I, build in z-direction, stayed intact over the entire test duration of 30 days. All eight samples, manufactured with Batch II, failed. However, during SilmagAl SCC testing, one specimen of each build direction, z- and xy, failed. Overviews of the test coupons after testing are given in the Appendix A.22 and A.21.

Microsectional analysis was performed in addition, to explain the failure of Scalmaalloy test samples. The investigation revealed for specimens out of Scalmaalloy powder Batch I and II, a microstructure of high porosity. A severe corrosive attack on pores which are opened to the surface was detected. The optical analysis of the microsections highlights furthermore the propagation of the corrosive attack along grain boundaries. The diffusion of the β - phase and their formation, partly in chains, on grain boundaries seem to cause this early failure. A TEM analysis in Section 4.3 highlighted such diffusion of the β -phase (Al_5Mg_8) already after ageing. The microstructure after sensitisation was not analysed by use of a TEM but these SCC results indicates a further and more pronounced diffusion of the β - phase to grain boundaries. If Scalmaalloy is really as susceptible to SCC as presumed by these test results, is difficult to predict. The corrosive attack in the loaded condition is so much higher than the observed attack in the unloaded condition in AIC, that further tests are necessary to draw a final conclusion about SCC resistance of Scalmaalloy. It is hence recommended, that the SCC test is repeated with a more representative, high quality microstructure without such a high porosity and at a lower load level. A test load of 90 % of R_m is very high and industrially may be not relevant.

The microsectional analysis of SilmagAl test coupons revealed also a certain porosity, however not as severe as seen on Scalmaalloy samples. The overall corrosive attack was comparable to the observed attack without loading. Failure occurred for both SilmagAl specimens while the

4. Results and discussion

load was adapted during the test. Although it was done carefully, an influence of this manual loading during testing can not be eliminated. Nevertheless is concluded, that the early failure of SilmagAl samples were caused because of its intermediate susceptibility to corrosion in NaCl.

Table 4.11.: Test results of stress corrosion cracking (SCC) of Scalmalloy and SilmagAl

| Scalmalloy | | | | |
|--------------|---------------------|-----------------|--------------------|----------------------------|
| Powder batch | Number of specimens | Build direction | Applied load [MPa] | Number of failed specimens |
| I | 3 | z | 450 | 1 |
| I | 3 | xy | 468 | 3 |
| II | 4 | z | 451 | 4 |
| II | 4 | xy | 478 | 4 |
| SilmagAl | | | | |
| I | 5 | z | 253 | 1 |
| I | 4 | xy | 275 | 1 |

Intergranular corrosion susceptibility of Scalmalloy was tested under even higher aggressive test conditions according to ASTM G67 [78]. Test samples were weighted before and after being exposed to HNO_3 for 24 hours. Different mass losses were measured in dependence on build direction of the specimens, see Table 4.12. Samples built in xy-direction, revealed a mass loss which is almost twice as high as the mass loss of samples built in z-direction. The microsectional analysis highlighted that a very uniform material removal in xy-direction, parallel to layer orientation and weld paths, was created. The material removal in z-direction, however, leads to a more jagged surface and a rather non-uniform material removal. This difference is caused by the microstructures of Scalmalloy which develops in alternating FG and UFG bands during SLM, explained in Section 4.2.3. The corrosive attack on grain boundaries in ultra-fine grain bands causes a fast separation between these grains. As result, the ultra-fine grains drop out fast and easily. Whereas the rather elongated fine grains resist longer to the corrosive attack. Compared to AA5083, tested as reference and resulting in a mass loss of 45 - 50 $[\text{g}/\text{cm}^3]$, is Scalmalloy less resistance. Hence, the susceptibility of Scalmalloy to IC is rated intermediate critical after sensitisation.

4. Results and discussion

Table 4.12.: Test results of IC of Scalmalloy

| Scalmalloy | | | | | | |
|--------------|-----------------|-----------------|----------------------|---------------------|------------------------|--------------------|
| Powder batch | Number of parts | Build direction | Mass before test [g] | Mass after test [g] | Mass loss [g/cm^3] | Standard deviation |
| I | 3 | z | 3992.03 | 3273.2 | 61.9 | 2.18 |
| I | 3 | xy | 4013.2 | 3599.7 | 35.44 | 2.84 |

The exfoliation corrosion behaviour of Scalmalloy was tested according to ASTM G66 [79]. Slight different intensities are observed again depending on the build direction of the samples. Samples built in z-direction, exhibit more pits than samples built in xy-direction, see Figure 4.29. The pits are in their shape more irregular and in their dimension larger compared to pits after AIC and also compared to pits on AA5083 after EXCO testing. However, neither an exfoliation and peeling off in layers, nor macroscopic signs of Pit-blistering were observed.

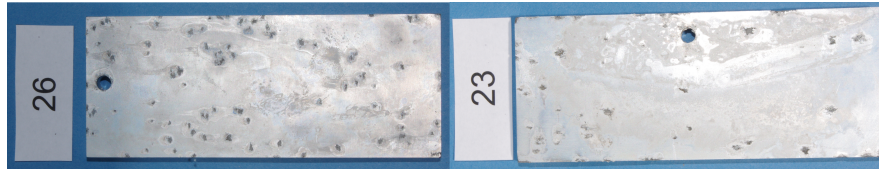


Figure 4.29.: Scalmalloy test specimen after EXCO testing

FINDINGS:

- The remaining defect and porosity level in Scalmalloy AM test coupons influences the corrosive attack significantly.
- Scalmalloy is more resistant than SilmagAl to AIC.
- Both, Scalmalloy and SilmagAl, are not classified highly susceptible to pitting in an unloaded NaCl test environment.
- Scalmalloy in sensitised condition tends to be more susceptible to SCC at a load level of 90 % of R_m , than SilmagAl.
- Scalmalloy reveal a uniform corrosive attack in IC and a higher mass loss compared to AA5083 sheet material.
- EXCO tests highlighted that Scalmalloy is rather non-critical classified regarding exfoliation corrosion.

4. Results and discussion

4.4.3. Result and discussion: static tensile strength

The presented static tensile strengths (ST) in the following Figures 4.31 - 4.35 represent the mean values of at least three and a maximum of ten cylindrical B4 x 20, B5 x 25 or B6 x 30 test samples. In every diagram the platform, build direction and the used heat treatment is mentioned. The used temperature in an additional HIP step correlates with the chosen ageing temperature, only the used pressure differs. The Hot isostatic pressing (HIP) at 1000 bar is referred to as HIP-1 and at 2000 bar to HIP-2. Presented in each diagram are $R_{p0.2}$, R_m , A and E.

Static tensile tests of Scalmaalloy Batch I reveal on different platforms and different chosen process parameters a very stable and consistent material behaviour, as seen in Figure 4.31. Scalmaalloy was processed on Platform P1 and P4 with Parameter Set 1 and on Platform P2 with Parameter Set 3.

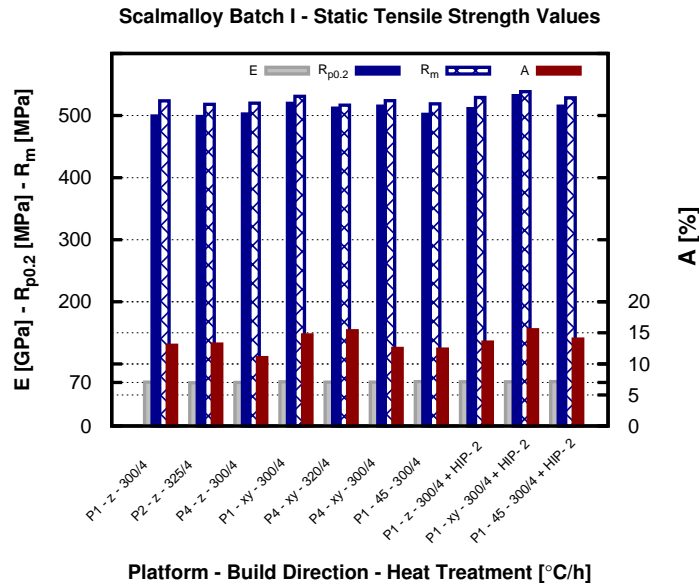


Figure 4.30.: Static tensile strength stress strain curve of Scalmaalloy samples of powder Batch I

The standard deviation of $R_{p0.2}$ and R_m between all aged specimens in the three build directions xy, z and 45 ° on Platforms P1, P2 and P4 is less than 10 MPa, and the standard deviation of $R_{p0.2}$ and R_m of all aged and HIP'ed samples on Platform P1 for all three build directions is around 11 MPa. The difference between yield and ultimate strength, $\Delta\sigma = R_m - R_{p0.2}$, ranges surprisingly from $5 \text{ MPa} \leq \Delta\sigma \leq 25 \text{ MPa}$. The Young's modulus is about 70 - 72 GPa and the elongation in the range of $11 \leq A \leq 15$ in aged and $14 \leq A \leq 16$ in aged and HIP condition. HIP apparently influences Scalmaalloy's ductility. Scalmaalloy powder Batch I obviously leads to a stable and reproducible process response on both laboratory scale at low

4. Results and discussion

build rate Parameter Set 1 and also for industrial applicable Parameter Set 3 at higher build rates.

One stress strain curve of each sample tested in xy-direction in aged condition built on Platform P1 and one sample built on P4 is drawn in Figure 4.31. Both curves exhibit a significant load drop after reaching R_m , which is followed by serrated yielding and elongating with little work hardening and several minor load drops. Work hardening seems to be slightly higher for the sample built on P4 than the one manufactured on P1. This difference indicates that $R_{p0.2}$ is not necessarily the right choice for measuring the yield strength of Scalmaalloy. A more suitable approach would be the definition of a lower and upper yield strength as is done for steel, to highlight the special hardening mechanisms that occur in Scalmaalloy.

Serrated yielding is well known for Al magnesium alloys and extensively described in literature [127]. A very similar to the one of Scalmaalloy is the stress strain curve of an Al6Mg2Sc1Zr alloy manufactured by the powder metallurgy route, as described in [123].

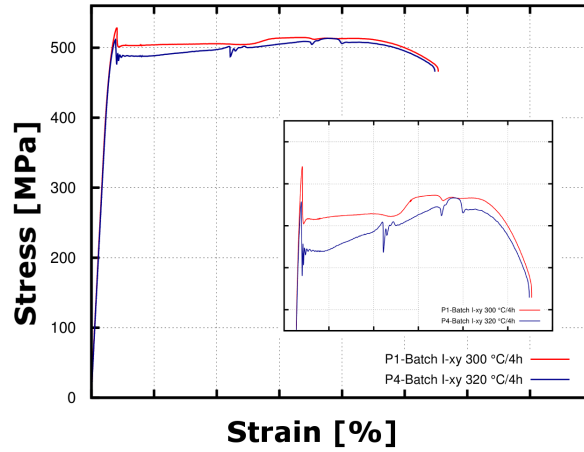


Figure 4.31.: Static tensile strength of Scalmaalloy samples of powder Batch I

A very different picture is drawn for Scalmaalloy Batch II, which demonstrates an inconsistent static tensile response on different platforms, shown in Figure 4.32. Scalmaalloy powder Batch II was processed on Platform P5 and Parameter Set 2 and on P3 at Parameter Set 5.

4. Results and discussion

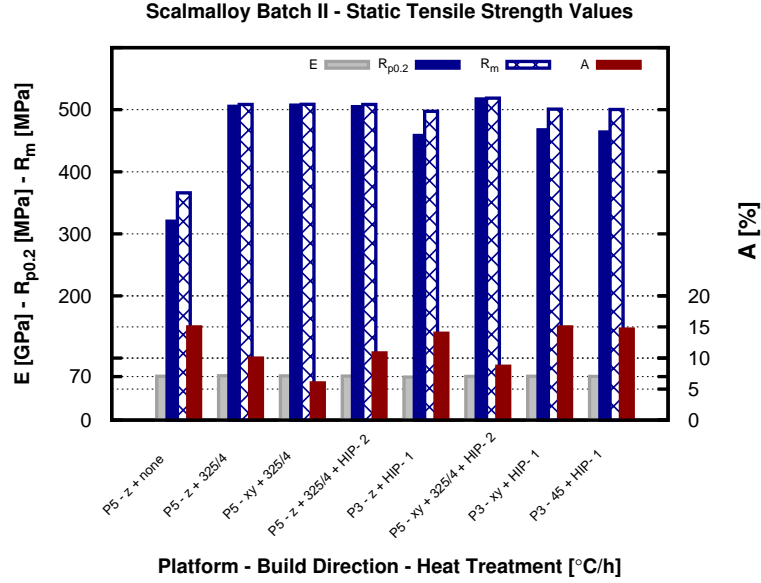


Figure 4.32.: Static tensile strength of Scalmalloy samples of powder Batch II

The process on P5 leads to an elongation of 15 % in the as-built condition which is initially too low. Precipitation hardening is always associated with a ductility loss, which means that an ageing step at 325 °C / 4h leads to a decrease of (A). The reduction after ageing was measured as $A = 6$ % for xy and 10 % for build direction z. Although HIP at 325 °C / 4h / 2000bar improves the elongation again to $A \approx 9$ % for xy and $A = 11$ % in z-direction, the achieved elongation is below the expected range. Many pores on the fracture surface also indicated that the material's quality and hence the process was not ideal. Scalmalloy Batch I demonstrated clearly that an elongation $A > 10$ % is also achievable after ageing and most definite $A \geq 14$ % after HIP. Both, $R_{p0.2}$ and R_m exceed 500 MPa for Scalmalloy Batch II on Platform P5, and a very low $\Delta\sigma$ between $R_{p0.2}$ and R_m was noted.

The process on Platform P3 leads to static strength response with low scatter on an elongation level of $A \approx 15$ %, with R_m over 500 MPa, but also to a substantially lower yield strength level, although samples in xy, z and 45° were only tested in hot isostatic pressed condition. This is not surprising, as the combination of Platform P3 and Parameter Set 4 was developed for industrial environments with a high build rate. The distribution of both UFG and FG bands is different to all other investigated AM Scalmalloy materials built at a lower z of 20 μm or 30 μm . Parameters Set 4 creates only a very small UFG band and hence is the hall-petch relation less contributing to the strengthening mechanism. Probably more dominant is here precipitation and solid solution hardening. It is also unlikely that a peak precipitation hardening was reached at the used heat treatment of 325 °C / 4h / 1000bar.

Hence, the chosen combination of Scalmalloy Batch II and process parameters sets 2 and 5 on both Platforms, are not ideally suited to achieve the full potential of Scalmalloy nor can a

4. Results and discussion

stable process over several builds be assumed.

Scalmalloy powder Batch III was processed on Platform P2 at Parameter Set 3 and tested in aged at 325 °C / 4h, and the HIP condition at 325 °C / 4h at either 1000 bar or 2000 bar. All samples were initially also heat treated at 300 °C / 2h. All reached values were in the exact same range as Scalmalloy powder Batch I. The standard deviation of $R_{p0.2}$ and R_m for each tested heat treatment condition with both build directions xy and z lies between 6 and 9 MPa, elongation is between $11 \leq A \leq 14$ and the Youngs modulus is $E = 70 - 72$ GPa. Scalmalloy Batch III b not only reproduces Scalmalloy Batch I results, but was also a very stable processed.

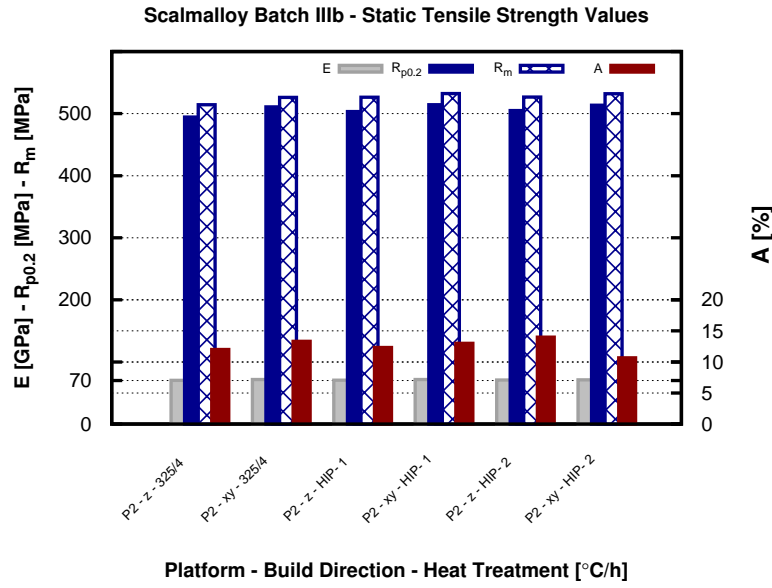


Figure 4.33.: Static tensile strength of Scalmalloy samples of powder Batch IIIb

SilmagAl powder Batch I was tested on Platform P5 with Parameter Set 5 in as-built, aged (165 °C / 7h), T6 (550 °C / 1h / WQ + 165 °C / 7h) and HIP (540 °C / 2h / 1000bar) plus T6 conditions. The as-built condition showed in xy direction a $R_{p0.2}$ of 247 MPa, a R_m of 430 MPa at 8.5 % elongation and in z-directions was $R_{p0.2} = 255$ MPa, $R_m = 407$ MPa at $A = 13$ % was achieved. After ageing and hence precipitation hardening increases in xy-direction $R_{p0.2}$ about 75 MPa. However, R_m and A remained unaffected and same values as in as built condition were obtained. In the z-direction both $R_{p0.2}$ and R_m increases about 30 MPa after aging at a decreasing elongation to $A = 9$ %. Precipitations in the microstructure are obviously not homogeneously distributed to affect and induce hardening mechanism in both build directions equally to generate an isotropic material behaviour. As indicated in [124], a solution annealing step before aging removes any segregations and aims to bring all

4. Results and discussion

alloying elements into solution to homogenise the microstructure. The results of SilmagAl in T6 condition confirm the homogenisation and very isotropical values were obtained. The $R_{p0.2}$ level is in both directions about 280 ± 6 MPa, the tensile strength $328 \text{ MPa} \pm 2$ MPa and the elongation decreases to $5 \% \pm 1 \%$. A higher porosity caused by hydrogen outgassing is noticed on the fracture surface of the specimens compared to as-built or aged test pieces, which causes probably the decrease in elongation. The influence of porosity is more significant under variable loads, so outgassing is discussed in more detail in Section 4.4.4. An additional HIP step accelerates outgassing and obviously closes or at least reduces the developing porosity, leading to an increase in all values. In xy-direction is $R_{p0.2} = 300$ MPa, $R_m = 350$ MPa at $A = 11 \%$ obtained and $R_{p0.2} = 310$ MPa, $R_m = 368$ MPa at $A = 11.5\%$ in z-direction. Especially the HIP plus T6 condition reveals a high potential by producing moderate strength at a sufficient ductility level.

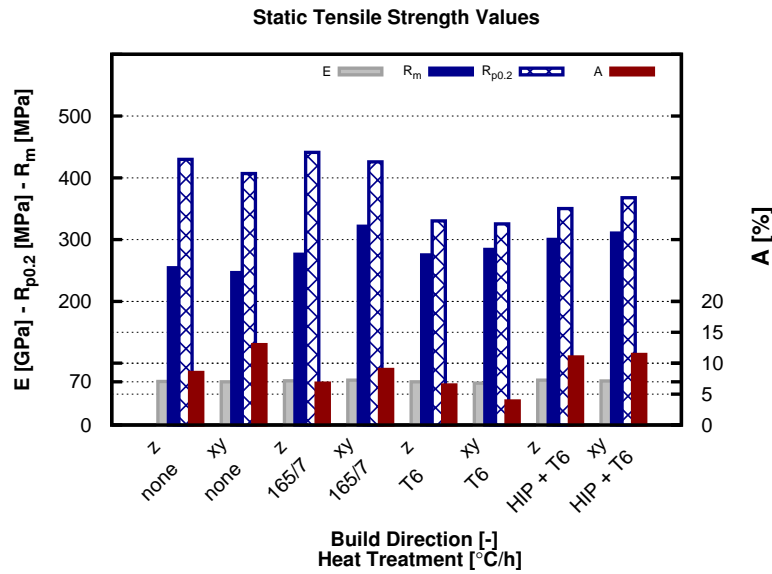


Figure 4.34.: Static tensile strength of SilmagAl samples of powder Batch I

SilmagAl powder Batch II reproduces the observed ST strength values in all temper conditions impressively; only the elongation is in each condition slightly lower. In the as-built condition was only the xy direction tested and $R_{p0.2} = 247$ MPa, $R_m = 420$ MPa at $A = 7 \%$ achieved. The subsequent precipitation hardening results in $R_{p0.2} = 336$ MPa, $R_m = 439$ MPa at $A = 5.5 \%$ for xy direction and in $R_{p0.2} = 283$ MPa, $R_m = 444$ MPa at $A = 5\%$ for z direction. Homogenisation and ageing led to $R_{p0.2} = 289 \text{ MPa} \pm 3$ MPa, $R_m = 333$ MPa at $A = 4 \% \pm 1 \%$ for both directions. The preset HIP step induces again an increase of $R_{p0.2} = 303$ MPa, $R_m = 355$ MPa at $A = 10\%$ in the xy-direction.

The static tensile response of SilmagAl Batches I and II matches very well and confirms that

4. Results and discussion

for both powders an equal process stability was achieved.

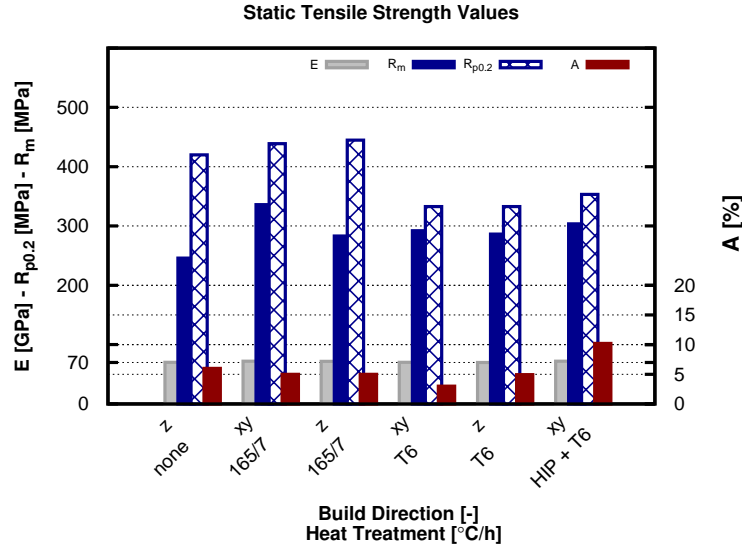


Figure 4.35.: Static tensile strength of SilmagAl samples of powder Batch II

FINDINGS:

- The highest static tensile strength values for Scalmalloy were measured for powder Batch I, processed with Parameters Set 1 on platform P1 in aged and HIP condition in xy-direction $R_{p0.2} = 532$ MPa, $R_m = 539$ MPa and an elongation $A = 16$ %
- Scalmalloy powder Batches I and III b processed at Parameters Set 1 or 3 on Platforms P1, P2 and P4 lead to reproducible high static strength values with a low scatter.
- No satisfying elongation values were obtained for Scalmalloy powder Batch II processed at Parameters Set 2 on platform P5.
- A high porosity on the fracture surfaces of tested Scalmalloy Batch II samples, manufactured at Parameters Set 2 on platform P5, do not correlate with the highly dense microstructure as analysed in 4.2.
- Scalmalloy Batch II, processed on an industrial scale on Platform P5 and Parameter Set 4, reveal a low scatter in $R_{p0.2}$, R_m and E in each build direction xy, z and 45° , but a significant low $R_{p0.2}$ level was measured.
- Both SilmagAl powder batches result in very similar ST values in each temper condition; only the elongation is slightly reduced in tests of powder Batch II compared to Batch I.

4. Results and discussion

- A moderate strength level of $R_{p0.2} \geq 300$ MPa, $R_m \geq 350$ MPa at sufficiently high elongation of $A \geq 10$ % can be obtained for SilmagAl in HIP + T6 condition.

4.4.4. Result and discussion: high cycle fatigue

All HCF tests were performed at a load ratio of $R = 0.1$ and notch factor $K = 1.035$ on specimens with a milled surface, as the process parameters were not optimised to create a smooth surface. Tests were terminated either at 3×10^6 cycles as assumed in DIN 6072 [82] or after an extended run time of 3×10^7 cycles. An analysis according to [82] shall also generate a Wöhler curve that indicates the 10 %, 50 % and 90 % probability of failure. Due to the obtained scatter for most of the curves and a limited number of tested specimens, the generation of the them was omitted throughout, as it would not be meaningful nor statistically correct.

Figure 4.36 summarises all tested Scalmaalloy specimens in aged (powder Batch II), aged and HIP (powder Batch I and II) and only HIP condition (powder Batch II) in xy and z direction in a S-N-diagramm. The notation of the samples follows the same rules as the notation in chapter 4.4.3.

Fatigue limit for samples of powder Batch I, manufactured with Parameter Set 1 on P4 and tested in xy and z direction, was achieved at $\sigma_{\max} = 300$ MPa for 3×10^7 cycles. A fatigue limit of $\sigma_{\max} \approx 312.5$ MPa is estimated for 3×10^6 cycles. This limit is considerably higher than fatigue limits of conventional high strength Al alloys like 7075, with an fatigue limit of 275 MPa at 3×10^6 cycles. However, in both tested directions, scatter appears in the low cycle fatigue regime. A surface fracture analysis of all test specimens revealed minor gas porosity and a crack initiation only at pores or defects at the surface. Different areas as fatigue striations after crack initiations, ductile fracture dimple structure and final fracture are clearly definable.

Scalmaalloy powder Batch II samples, manufactured on P5 at Parameter Set 2, were tested in aged and aged and HIP condition. A run out at $N = 3 \times 10^7$ was achieved only at $\sigma_{\max} = 160$ MPa for the z- direction in aged and at $\sigma_{\max} = 240$ MPa for xy- direction in aged and HIP condition. In both conditions and both directions, a severe scatter is noticed. Defects were exposed to the surface after milling and already macroscopic detectable before testing. Fracture surfaces also feature large lack of fusion porosity and a very turbulent microstructure. Areas of striations or dimple structures are not equally pronounced definable, as for Scalmaalloy Batch I specimens. Moreover, single scan paths are clearly visible. The microstructure quality is obviously inferior compared to the microstructure of specimens of Scalmaalloy Batch I built on P4. The high process stability of Scalmaalloy Batch I on P5 at Parameter Set 2, as predicted in Section 4.2.2 by analysing cubic samples, was not achieved during the manufacturing of these HCF specimens.

Although the increase of fatigue limit to $\sigma_{\max} = 240$ MPa indeed reveals that a certain bonding effect or defect size reduction after HIP can be achieved, nonetheless the high scatter in the HCF response can not be removed. Kissing bonds are created by the additional HIP step, see also chapter 4.3. That means that the internal surfaces of a defect are pressed on each other but without diffusion processes being activated. It only leads to some kind of cold gluing, which is even more dangerous than the high initial porosity of the aged configuration without HIP as kissing bonds are a real challenge for quality control or NDT inspection methods. They

4. Results and discussion

will stay in most cases undetected and this is an unacceptable risk with regard to licensing as aerospace material.

To sum up, all specimens of Scalmalloy Batch II, built on Platform P5 at Parameter Set 2, demonstrate a HCF behaviour if the microstructural quality is low and inhibits large porosity or defect areas in aged and aged plus HIP condition.

The Scalmalloy HCF curve out of powder Batch II, built with the industrial Parameter Set 4 on P3, has a fatigue limit at 3×10^6 cycles of $\sigma_{\max} = 285$ MPa but failed after extended testing at 4.2×10^6 cycles. Compared to Scalmalloy Batch I, according to this number of cycles, the fatigue limit is around 27.5 MPa lower. On all fracture surfaces of all specimens, a high but fine and homogeneously distributed gas porosity is clearly visible. One test specimen failed at 280 MPa in the low cycle regime already at 7.9×10^4 cycles. The fracture surface analysis of this specimen featured large inclusions that led to this early failure, for which powder contamination is the most likely reason. It would be possible to create a useful Wöhler curve only if that test specimen was removed from the calculation. However, that omission clearly warps the evaluation regarding the stability of the used manufacturing route.

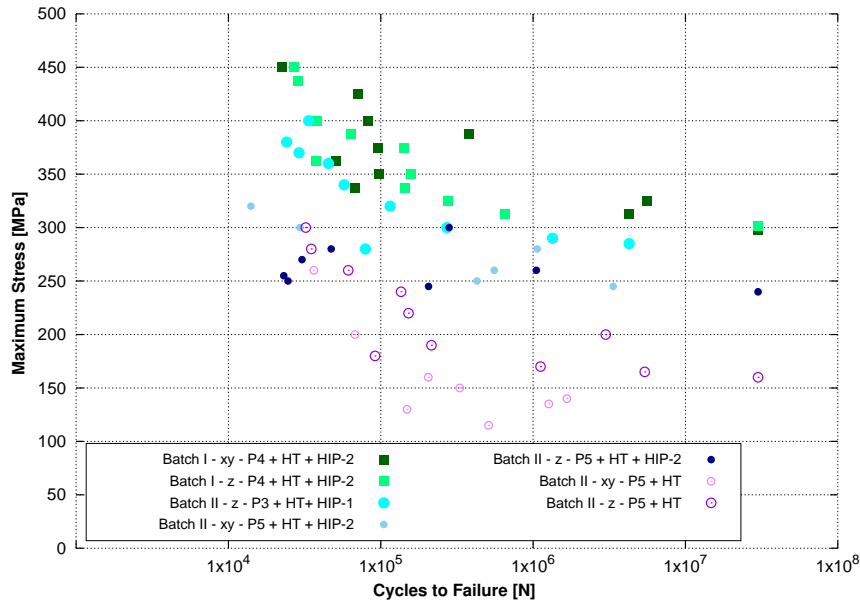


Figure 4.36.: High Cycle Fatigue (HCF) of Scalmalloy Batches I and II

Figure 4.37 displays all data points of seven high cycle fatigue (HCF) tests of AM SilmagAl in different heat treatment conditions. Build directions xy and z have both been tested for SilmagAl powder Batch I in aged, T6 or HIP and T6 condition; however SilmagAl powder Batch II was tested only in the aged condition for xy direction. Tests in T6 and aged condition were terminated at $N = 3 \times 10^6$; however, HCF tests for powder Batch I in the T6 plus HIP condition were terminated at $N = 3 \times 10^7$, as they obtained the highest fatigue limits and seemed to be

4. Results and discussion

the most promising heat treatment condition regarding fatigue.

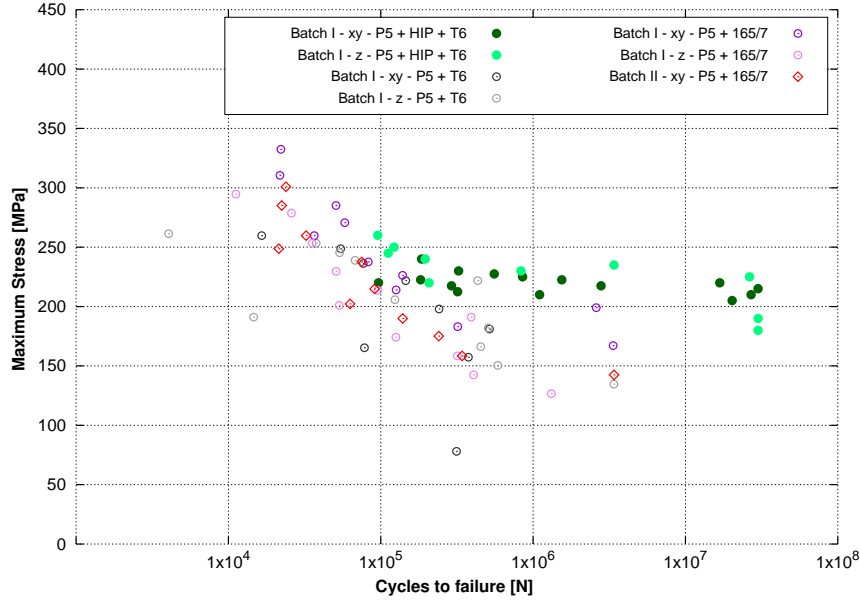


Figure 4.37.: High Cycle Fatigue (HCF) of SilmagAl Batches I and II

The HCF response of the aged condition confirms the anisotropic material behaviour which was already observed in yield strength in static tensile testing. The xy- direction for powder Batch I reveal a comparably low scatter and a fatigue limit at $N \approx 3 \times 10^6$ and $\sigma_{\max} = 180$ MPa. However, a scatter in the low cycle fatigue range in z- direction is obtained and a significant lower fatigue limit at $N = 1.3 \times 10^6$ and $\sigma_{\max} = 127$ MPa. The defect and porosity density on fracture surfaces on samples out of the z- direction seems to be higher compared to samples out of the xy- direction. It is furthermore assumed that segregations in the HAZ influence and decrease the fatigue resistance in z- direction. SilmagAl powder Batch II obtained in xy- direction an overall lower fatigue resistance and a lower fatigue limit at $\sigma_{\max} = 142$ MPa and $N \approx 3 \times 10^6$ compared to powder Batch I. A different and increased oxygen content is assumed to be one of the reasons as also the elongation of samples out of powder Batch II in static tensile testing is reduced compared to samples out of Batch I. The differences between these three curves in fatigue resistance emphasises that more tests are necessary to evaluate the microstructure, chemical composition and the porosity or defect density and occurrence properly in the aged temper condition for SilmagAl.

The direct comparison of the aged and the T6 condition indicates that the additional solution annealing step causes a material quality decrease. The effectiveness of T6, the homogenisation the microstructure with a subsequent precipitation hardening, cannot be validated, as a high defect level dominates the HCF behaviour of these samples. A fracture surface comparison of both conditions highlights that in these specimens an increased microstructural porosity ex-

4. Results and discussion

ists. Solution annealing at 550 °C / 1 h obviously causes an outgassing of dissolved interstitial hydrogen, which leads to a localized porosity that provides pre-existing sites for cavity growth [128]. In general, the diffusion of hydrogen in an Al matrix is heat and time dependent and Al is known to be an extremely low outgassing material at lower temperatures [129, 130]. Hence, effects of hydrogen release are not visible after ageing at 165 °C / 7 but evidently activated by the chosen annealing heat treatment cycle. That means necessarily that HIP in the annealing temperature range at 540 °C / 2 h also causes hydrogen diffusion but accelerated due to the used high pressure. In these tests, the remaining hydrogen content after HIP must be quite low, as the downstream solution annealing and water quenching does not lead to a significant visible porosity on the fracture surface. A high fatigue limit at $N = 3 \times 10^7$ and $\sigma_{\max} = 210$ MPa in xy- direction and $\sigma_{\max} = 225$ MPa in z- direction was achieved. That means, that the efficiency of applying a HIP cycle for AM SilmagAl at an annealing temperature level and a subsequent T6 heat treatment is clearly shown. However, it also has to be emphasised that HIP in the annealing temperature level will not remove any initial level of hydrogen contamination equally efficiently; it is more likely that a (low) threshold hydrogen content limits the effectiveness of HIP.

In [1] similar fatigue limits $\sigma_{\max} > 200$ MPa are reached for AlSi10Mg and tested at $R = 0.1$ but processed at $P_L = 250$ W and slow scan speed of $v_s = 50$ mm/s. In [131], the influence of a preheating of the platform is investigated by comparing Wöhler curves of AlSi10Mg samples built at a heated base plate of 30 °C and 300 °C. The highest fatigue limit here was reached at $N = 3 \times 10^7$ and 200 MPa in xy direction without preheating in the T6 condition.

FINDINGS

- Scalmalloy Batch I, processed at the laboratory level with low build rate parameters, generates a perfect microstructure that leads to a high fatigue resistance and a run out at $N = 3 \times 10^7$ at 300 MPa in both build directions xy and z.
- Scalmalloy Batch II, processed with a Parameter Set 2 of increased build rate, generates a highly unstable process while printing more complex builds than cubes. Large microstructural defects occurred, which dominate the fatigue resistance in both tested heat treatment conditions. Hot isostatic pressing of these samples creates furthermore dangerous kissing bonds which lead to an unacceptable scatter in the HCF response for $N > 1 \times 10^5$ cycles.
- Scalmalloy Batch II processed on industrial scale indicates that the process stability is also not completely satisfactory, as one outlier at 280 MPa and 79339 Cycles was determined and the fatigue limit at $N = 3 \times 10^7$ is 27.5 MPa lower compared to Scalmalloy Batch I processed at laboratory level.
- SilmagAl Batch I in the HIP plus T6 condition reaches the highest fatigue limits at $N = 3 \times 10^7$ and 210 MPa in xy- and 225 MPa in z-direction.
- SilmagAl Batch I in temper condition aged reveal anisotropic material behaviour with different significant scatter in xy- and z- direction. SilmagAl Batch II achieved in aged condition in xy- direction a lower fatigue resistance.

4. Results and discussion

- A proper analysis of SilmagAl Batch I in T6 temper condition was not possible as hydrogen outgassing during the annealing created a high defect quantity which was dominating the HCF response.

4.4.5. Result and discussion: fracture toughness

Table 4.13 summarises all fracture toughness test results for Scalmalloy and SilmagAl. All K_Q and K_{IC} values are the average values of the tested number of specimens. Scalmalloy was tested in HIP plus aged condition and SilmagAl was tested in HIP plus T6 temper condition. A valid sample width, according to ASTM E399 to fulfill the plasticity criterion (samples width $\geq 2.5 (K_Q / R_{p0.2})^2$), leads to sample dimensions which are large and difficult to manufacture in SLM processes. Large samples shall ensure that the plastic zone stays small in relation to the tested cross-section. Loading is also restricted to essentially the linear elastic regime by the load criteria ($F_{max} / F_Q \leq 1.1$). If all validity criteria are met, can only be evaluated when the test is completed. Although guidelines help to choose the correct dimension, there is no guarantee ahead of the testing that a valid K_{IC} will be obtained.

Indeed, all CT18 specimens did not meet the plasticity or load criterion to render a valid K_{IC} . Only CT30 specimens for Scalmalloy powder Batch I and II yielded valid K_{IC} values, but it has to be remarked that Batch I samples with crack growth in xy- plane were additionally side grooved after it was noted that the tested z- plane crack growth did not result in a valid K_{IC} . Another approach, according to ASTM E1820 [132], was tested on one CT30 sample of Scalmalloy Batch I with crack growth in xy- plane as well. ASTM E1820 allows an evaluation based on the J- integral if a valid K_{IC} value could not be obtained. However, the therefore required loading and unloading could not be realised for Scalmalloy, as final fracture occurred already after three load cycles, so neither a valid J_{IC} nor K_{IC} was rendered.

The K_{IC} tests with samples of Scalmalloy powder Batch I yielded surprisingly very high fracture toughness values of $K_Q = 39 \text{ MPa}\sqrt{m}$ for crack growth in z- and $K_{IC} = 38 \text{ MPa}\sqrt{m}$ for crack growth in xy- direction. The Scalmalloy material concept intended to combine a high strength material behaviour by keeping a high ductility. The obtained high K_Q and K_{IC} values confirm that this aim was successfully achieved. However, test samples manufactured on Platform P3 with parameter set 4 and P5 with parameter set 2 with Scalmalloy powder Batch II did not yield equally high values. A drop of 5 - 6 $\text{MPa}\sqrt{m}$ for crack growth in z- direction and a drop of 10 $\text{MPa}\sqrt{m}$ for crack growth in xy- direction were noted.

The fracture toughness results of SilmagAl matches well the intrinsic fracture toughness estimation by Speidel [108] (see section 3.4.6). A $K_{IC} \approx 20 \text{ MPa}\sqrt{m}$ was estimated and values of $K_Q = 18 \text{ MPa}\sqrt{m}$ for crack growth in z- plane for SilmagAl powder Batch I, and $K_Q = 19 \text{ MPa}\sqrt{m}$ for crack growth in xy- direction for both powder Batches I and II were obtained.

Fracture toughness normally depends strongly on constituent particles [84] and is considered to response very sensitive to microstructural inconsistencies. Large and coarse particles, precipitations on grain boundaries, dendrite arm spacing, segregations of constituent particles [84] or precipitation free zones [47] all have a negative effect on the fracture toughness. As indicated by ST or HCF response, the Scalmalloy powder Batch II constitution did not result in an ideal stable SLM process. The full potential that the chemical composition of Scalmal-

4. Results and discussion

loy Batch II would offer was not exploited. Hence it is assumed that a uniform distribution of UFG and FG microstructure (observed in Section 4.2.3) was created only in fracture toughness samples out of Scalmaalloy Batch I. A rather turbulent distribution of these two bands, resulting in particle-free zones, enrichment of oxides and porosity probably lead to the noticed drop in fracture toughness. Especially the particle-free zones are considered quite influential, as they are softer than the surrounding material and plastic deformation starts quite easily and leads to void formation and their coalescence.

A considerably low fracture toughness was measured for SilmagAl in both crack-growth directions, xy and z. SilmagAl was tested only in temper condition HIP + T6 which included an annealing step with water quenching. It is estimated that the chosen water quenching procedure did not offer cooling rates sufficient enough to realise the full potential of the material. A complete prevention of grain boundary precipitations was probably not achieved. It is assumed that the low values are due to the formation of grain boundary precipitations which cause grain boundary fracture and / or due to large constituent particles like oxides. For established Al alloys, so called C-curves exist which reveal temperature-time-dependencies on precipitations and hence critical zones for quenching. It would be necessary to establish a C-curve for SilmagAl to find the best possible temper condition regarding optimal fracture toughness values.

Table 4.13.: Overview fracture toughness K_{IC} test results of Scalmaalloy and SilmagAl

| Scalmaalloy | | | | | | | |
|--------------|-----------------------------|--------------------------|--------------------------|------------------|----------------------|-------------------------|-------------------|
| Powder Batch | Platform + Para - meter Set | Crack Growth Di- rection | Plas- ticity Cri- terion | Load Cri- terion | K_q MPa \sqrt{m} | K_{IC} MPa \sqrt{m} | Specimen (number) |
| I | P4 + 1 | z | invalid | invalid | 39 | 38 | CT30 (3) |
| I | P4 + 1 | xy | valid | valid | | | CT30 (2) |
| II | P3 + 4 | z | valid | valid | | 34 | CT30 (3) |
| II | P5 + 2 | z | invalid | invalid | 33 | | CT18 (3) |
| II | P5 + 2 | xy | invalid | invalid | 28 | | CT18 (3) |
| SilmagAl | | | | | | | |
| I | P5 + 5 | z | invalid | invalid | 18 | | CT18 (3) |
| I | P5 + 5 | xy | invalid | invalid | 19 | | CT18 (5) |
| II | P5 + 5 | xy | invalid | valid | 19 | | CT18 (2) |

FINDINGS

- Scalmaalloy powder Batch I on P4 with Parameter Set 1 obtained very high fracture toughness values with $K_Q > 38 \text{ MPa}\sqrt{m}$ for both tested crack growth directions.
- It was not possible to reproduce with Scalmaalloy powder Batch II equally high K_Q

4. Results and discussion

values, neither at platform P3 and Parameter Set 4 nor at platform P5 and Parameter Set 2.

- The microstructural differences in the test samples out of Scalmalloy Batch I and II are significant and hence do not result in the same K_Q level.
- Fracture toughness test coupons out of both tested SilmagAl powder batches I and II render a low KQ value level of $K_Q = (18 - 19) \text{ MPa}\sqrt{m}$ for the HIP + T6 condition.

4.4.6. Result and discussion: crack growth and crack growth threshold

A damage tolerance analysis is essential for any new material to ensure that parts are designed to support a slow and stable crack growth until the crack can be determined by any non-destructive inspection method. As the microstructural analysis of both materials displayed substantial differences from known microstructures of conventional aluminium alloys, a determination of the complete crack propagation behaviour of all three $\Delta a/\Delta N - \Delta K$ regions (see Figure 2.11) was done for both materials Scalmalloy and SilmagAl. Specimens were manufactured out of powder Batch I on either Platform P4 and Parameter Set 1 in HIP plus aged condition for Scalmalloy or on Platform P5 and Parameter Set 5 in HIP plus T6 condition for SilmagAl respectively. Fatigue crack growth and fatigue crack growth threshold measurements were executed for crack growth in the xy- and z- direction at load ratio $R = 0.1$ and $R = 0.7$. Figure 4.38 contains two $\Delta a/\Delta N - \Delta K$ curves at $R = 0.1$ for Scalmalloy and two for SilmagAl with each crack growth direction xy and z. However, Figure 4.39 presents only three $\Delta a/\Delta N - \Delta K$ curves at $R = 0.7$ with Scalmalloy specimens tested with crack growth in xy- and z- direction and one SilmagAl specimen tested with crack growth in z- direction.

4. Results and discussion

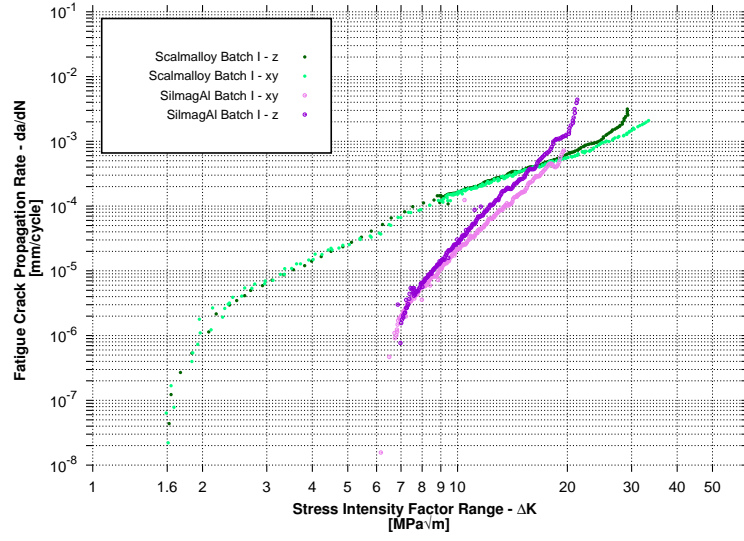


Figure 4.38.: Scalmalloy and SilmagAl Batch I fatigue crack growth rate $\Delta a/\Delta N$ - ΔK including ΔK_{th} values for load ratio $R = 0.1$ and crack growth direction z and xy

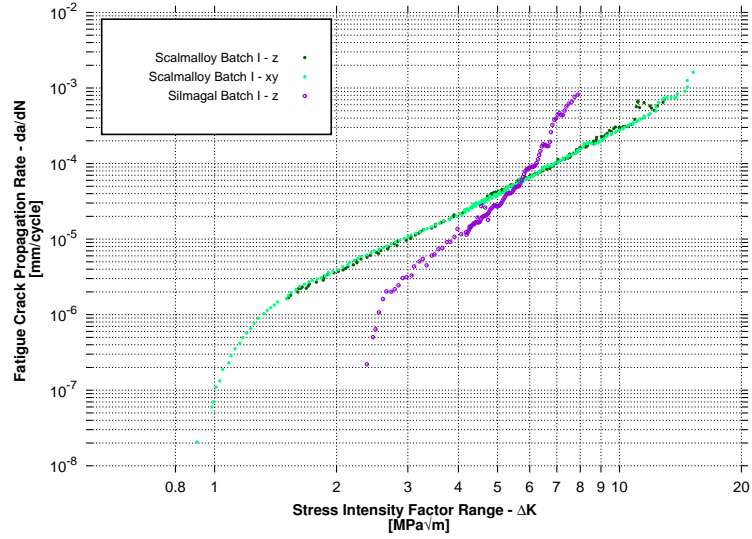


Figure 4.39.: Scalmalloy and SilmagAl Batch I fatigue crack growth rate $\Delta a/\Delta N$ - ΔK including ΔK_{th} values for load ratio $R=0.7$ and crack growth direction z and xy

For both alloys, no difference is notable if the crack grows in xy - or z - direction at both load ratios. However, the near-threshold regime and the fatigue crack propagation under cyclic

4. Results and discussion

loading differ significantly between the two alloys. SilmagAl at a lower $R_{p0.2}$ and R_m level, displays for load ratios $R = 0.1$ more favorable crack propagation values compared to Scalmalloy. The crack propagates in the Paris regime of the $\Delta a/\Delta N$ - ΔK SilmagAl curve (until $\approx \Delta K = 18 \text{ MPa}\sqrt{m}$) significantly less than in Scalmalloy. Threshold values for Scalmalloy specimens were measured already at a low level of $\Delta K_{th} = 1.6 \text{ MPa}\sqrt{m}$ in both crack growth directions xy and z . However, the crack propagation threshold values of SilmagAl test specimens are between $6 \text{ MPa}\sqrt{m} \leq \Delta K_{th} \leq 7 \text{ MPa}\sqrt{m}$ in xy - and z - direction. Crack closure effects are mainly eliminated at load ratio $R = 0.7$ which results in slightly different behaviour between the alloys. The crack in the SilmagAl sample grew only to $\Delta K = 5.5 \text{ MPa}\sqrt{m}$ slower compared to cracks in Scalmalloy samples. At $\Delta K > 5.5 \text{ MPa}\sqrt{m}$ Scalmalloy test samples changed into a slower crack propagation behaviour compared to SilmagAl. For both alloys, decreases the ΔK_{th} with the increasing load ratio, from $\Delta K_{th} = 1.6 \text{ MPa}\sqrt{m}$ to $< 1 \text{ MPa}\sqrt{m}$ for Scalmalloy and from $\Delta K_{th} = 7 \text{ MPa}\sqrt{m}$ to $2.3 \text{ MPa}\sqrt{m}$ for SilmagAl (for crack growth in z -direction). Crack closure effects are hence more pronounced in SilmagAl than in Scalmalloy. The near-threshold Regime I in fatigue crack curves is in general strongly dependent on microstructural features around the crack tip. The influence of the very local microstructure around the crack tip is significantly reduced in upper Paris regime II but becomes dominant again in the final stage, Stage III, where the ΔK reaches fracture toughness K_C and leads to unstable crack growth. Slipping planes in front of the crack tip are generally considered to be predominantly dependent on grain and precipitation size and distribution [84]. The very special microstructure of Scalmalloy with alternating ultra-fine grain and fine grain bands with homogeneously distributed full coherent $Al_3(Sc_{(1-x)},Zr_x)$ precipitations is hence assumed to be the main driver for its poor fatigue crack growth behaviour. In Scalmalloy, neither grain boundaries nor precipitations are able to prevent crack growth propagation under cyclic loads. If the plastic zone in front of the crack tip is of the same size as the grains, the fracture can change from intra- to less favourable inter-granular, as shown for ultrafine grained Al-alloys in [133]. However, Pao [134] obtained very similar ΔK_{th} values for fine grained Al7Mg material which was manufactured by powder metallurgy, but the noted fracture was still transgranular although the fracture paths are less tortuous compared to conventionally grained Al7Mg material. On the other side, it can be assumed that coarser grains and the size and distribution of precipitations in SilmagAl lead to a more favourable, lower crack propagation. Further investigations are necessary to investigate the mechanism that lead to the observed crack propagation in Scalmalloy and SilmagAl.

FINDINGS

- The crack growth behaviour confirm the extraordinary microstructure of alternating UFG and FG bands in AM Scalmalloy test samples, which are manufactured with Batch I on P4 with Parameter Set 1. The crack starts growing on surprisingly low threshold values for both load ratios $R = 0.1$ and $R = 0.7$.
- SilmagAl test coupons out of powder Batch I and manufactured on P5 with Parameter Set 5 result in higher threshold values and slower crack propagation behaviour in the lower Paris regime compared to Scalmalloy for both load ratios $R = 0.1$ and $R = 0.7$.
- Only in the upper Paris regime is the fatigue crack propagation in Scalmalloy test sam-

4. Results and discussion

ples significantly slower compared to crack growth in SilmagAl specimens (or other conventional high strength Al- alloys).

4.4.7. Discussion of powder, process and material properties correlation

This section mainly concerns the dependency of powder characteristics of each investigated batch on its processability in SLM systems. The impact of the chosen parameter sets on the microstructure and hence the response of the material properties will be evaluated, as well as the stability of the process.

Section 4.1.7 discussed that the surface fractal ψ , the avalanche angle α_P and the avalanche energy E_{av} together cover a wide range of powder characteristics, and these three are the most informative of all investigated powder characteristics. An intrinsic reorganisation behaviour of the powder which led to a smooth bulk surface and a resulting $\psi \approx 2$ can be obtained only if the powder batch contains mainly spherical particles at a size distribution with a higher Span value and if it is only moderate cohesive. The chemical composition of both alloys, Scal-malloy and SilmagAl, also had a significant influence on their processability. For LBW of Al-alloys, as shown in [34], the evaporation temperature of the alloying elements also affects the welding mode. Scalmalloy contains a high amount of Mg which evaporates at low temperatures. During processing all Scalmalloy powder batches a fast and pronounced development of weld smoke, consisting of metal vapor and other residues, was noted, and high speed videos of the process additionally highlighted very vigorous melt pool dynamics. However, Si, as one of the main alloying elements in SilmagAl, has almost no influence on the evaporation temperature, but decreases the melt's viscosity, producing a homogeneous weld bead formation. No pronounced vigorous melt pool dynamics are observed.

Scalmalloy Batch I displayed a very smooth bulk surface at $\psi = 1.91$, which results in multiple suitable parameter combinations on different platforms. For every combination, it was possible to find a stable heat conductivity welding mode which led to a very uniform microstructure, analysed in Section 4.2.1 and 4.2.3. The heat transfer was constant over the build of all test specimens and the observed alternating UFG and FG bands developed consistently. The extensive material characterisation leads to the conclusion that a high material quality was achieved, performing very consistently even under fatigue loads. Scalmalloy powder Batch I was very well suited for use in SLM systems, and high process stability was gained.

Scalmalloy Batch II was already critically evaluated regarding suitability for SLM processes in Section 4.1.7. Only around 50 % of all particles are spherically shaped; all remaining particles have a nodular morphology. This is, among others, a reason for high interparticle forces as measured by $\alpha_P = 52.34^\circ$ and more obvious by $E_{av} = 30.61$ kJ/kg. A surface fractal of $\psi = 2.76$ also revealed that only a non-ideal jagged powder bulk surface was achieved by this powder configuration. That affected mainly the processability of this powder batch. A transfer of the obtained suitable parameter set of Scalmalloy Batch I to Batch II was not possible. The energy input into the powder Batch II followed different mechanisms.

On Platform P5, only a very narrow parameter set consisting of $P_L = 400$ W at $v_s = 800$ mm/s

4. Results and discussion

was identified to create a uniform microsection and a low porosity. However, the material characterisation showed that this parameter set did not result in a high process stability. The static tensile test analysis highlights that the full potential Scalmetalloy offers regarding ductility and strength was not obtained. In static tensile tests, the elongation in all tested conditions, as-built, aged and aged plus HIP, was on the one hand too low and on the other hand scattered severely. A massively porous fracture surface on several HCF test specimens was noted, leading to a poor fatigue behavior on a low load level. The fracture toughness values are also lower compared to values obtained for Scalmetalloy Batch I. Both powder Batches I and II followed obviously different welding modes and resulted hence in a different microstructure.

Contrary to Batch I, rather jagged bulks surface of Batch II created beam traps, as explained in Section 2.1.1, which results in locally higher absorption and transition or keyhole welding mode. Equation 2.1 changes according to [135] in 4.3.

$$P_L = P_{refl} + P_{abs} + P_{trans} + P_{plasma} + P_{vapour} \quad (4.3)$$

Although generally a lower laser power dissipation and a higher absorption is targeted in LBW, the noted non-uniform and only local high absorption in SLM is not beneficial regarding development of a uniform microstructure. The high material performance obtained for Scalmetalloy Batch I based mainly on the uniform alternating UFG and FG bands. An unpredictable shift and mix of all three welding modes, heat conductivity, transition and keyhole welding, during the process changes the fraction of UFG and FG bands. The microstructure is no longer uniform and consists of rather turbulently spread UFG and FG bands. This turbulence leads to diminished mechanical properties, as noted when testing processed Scalmetalloy Batch II on Platform P5.

The industrial combination of Parameters Set 4 on Platform P3 for Batch II, however, revealed in ST testing a high elongation level but at lower $R_{p0.2}$. The obtained Wöhler curve also revealed a lower load level compared to Batch I, and the fracture toughness values also do not reach the high values obtained for Batch I. Although the low scatter in all results of Batch II processed on P3 do not indicate a severe porosity problem or missing process stability, the high material performance of Scalmetalloy which is theoretically feasible is not achieved. Hence, it can be concluded, that the powder configuration of Scalmetalloy powder Batch II cannot be recommended for any qualification process.

Scalmetalloy powder Batch IIIb cohesiveness' and the level of inter-particle forces are comparable to Batch I at $\alpha_P = 44.14^\circ$ and $E_{av} = 18.93$ kJ/kg. The surface fractale $\psi = 2.41$ is higher than Batch I but lower than Batch II and the particles morphology is mainly spherical. The powder's constitution matches Batch I, except for the missing high fraction of fine particles and minor deviations in the chemical composition. The transfer of used parameter sets for Batch I to Batch IIIb are feasible, and a similar microstructure is developed. The slightly higher roughness of the powders bulk surface of Batch IIIb compared to Batch I seems to be negligible. Beam traps and local high absorptions could not be observed, probably because the powder particles were less cohesive than particles in Batch II and were mainly spherical. Although a comprehensive material characterisation was not done, indicates the static strength behaviour that a very similar material behaviour to Batch I can be realised. The elongation in static tensile testing was constantly higher than 11 %. A uniform distribution of the UFG

4. Results and discussion

and FG bands was achieved, equal to the observed microstructure of Scalmalloy Batch I material. Whether a full reproducibility of the high material quality of Batch I is achieved, can be evaluated only after a comprehensive characterisation but it is assumed that it is quite likely.

Scalmalloy powder Batch V revealed the poorest surface fractal of all tested powders at $\psi = 2.94$, a low $\alpha_P = 33.84^\circ$, indicating high flowability and $E_{av} = 15.5$ kJ/kg which is comparable to the cohesiveness to powder Batch I. It was not possible to define an operating window with the tested amount of powder. Each tested parameter set resulted in a severely cracked and porous microstructure. Only at a 400 W and 600 mm/s was enough energy induced to produce at least partly dense areas in the microstructure. Many reasons for this result can be found in the powder's constitution. The particle size distribution is rather mono-modal compared to the other batches with a large $d_{50} = 65.35$ and the powder's flowability is also quite high, these two characteristics are identified as the most dominating process-influencing characteristics. After recoating reorganises powder Batch V in a most unpropitious way. The high flowability leads to a distribution of the powder's particles on the base plate that is not nearly close packing, and if no mechanical interlocking between powder particles is guaranteed, no homogeneous heat transfer can be realised. The absorption decreases significantly, and the reflexivity increases. The poor surface fractal value $\psi = 2.94$ measured in the RPA is most probably even worse in the real processing environment. This behaviour supports by implication also that a certain level of fine particles are beneficial for the processability of a powder.

Guertler [136] has shown for AlSi10Mg powders that a particle size distribution with high number of fine particles leads to a more stable process. This was also confirmed by comparing the processability of all Scalmalloy powder batches. Especially for Scalmalloy powder Batch I, the fraction of fine particles was obviously beneficial for the reorganisation behaviour ($\psi = 1.91$) of the powder after being applied on the platform, and hence for a constant heat transfer and uniform welding mode.

That leads to the conclusion that the configuration of powder Batch V is also not suited for a qualification process.

The evaluation of SilmagAl powder batches followed the same line of argument, but as SilmagAl creates a low-viscosity melt, the effects of powder's characteristics are less notable. The analysis of SilmagAl Batch I highlights that the powder's configuration consists of perfectly spheroidal particles with a median $\alpha_P = 43.92^\circ$ and $E_{av} = 17.7$ kJ/kg, indicating a certain cohesiveness that results in a low bulk surface roughness of $\psi = 2.39$. The material characterisation revealed that a high process stability was achieved, and a low scatter in the results were observed. Defects in T6 condition were caused by hydrogen release and cannot be traced back to an unsuited combination of processing parameters. It is assumed that it was rather the powder handling that lead to hydrogen contamination.

However, SilmagAl Batch II indicates that the powder configuration leads to a severely jagged powder bulk surface $\psi = 4.4$ and a high flowability. This is actually the same combination as noted for Scalmalloy Batch V. However, contrary to Scalmalloy Batch V, SilmagAl Batch II was almost as easily processable as SilmagAl Batch I. SilmagAl obviously is stable and processable over a wide range of powder compositions and parameter sets. The weld

4. Results and discussion

bead formation benefits highly from the low viscous melt and compensates non-ideal powder characteristics and a non-ideal heat transfer. SilmagAl combines obviously a very tolerant behaviour against powder or process deviations by achieving moderate strength levels and sufficient elongation in static tensile testing. No substantial differences were noted in static tensile testing between both SilmagAl powder batches. The microstructural response also did not indicate severe process instabilities. But nevertheless SilmagAl Batch II AM material was admittedly not comprehensively characterised and as a slight decrease in HCF behaviour and elongation was observed, it is expected that other material characteristics, like K_{IC} would also deviate to the observed values that were obtained for SilmagAl batch I.

There is, therefore, a definite need for a specification of the Scalmaalloy and SilmagAl powder to ensure that the best possible microstructure of both alloys manufactured in SLM processes can be obtained. Table 4.14 presents the most relevant powder characteristics, summarised and ranged to certain values.

FINDINGS:

- Test coupons out of Scalmaalloy Batch I led in every material characterising test consistent values.
- Samples out of Scalmaalloy Batch III led to properties that are quite close to Batch I and the AM material of Batch III showed in static tensile test and microstructural analysis a very comparable response. Hence, a conclusion to the powder characteristics on processability can be drawn.
- The powder's bulk surface or reorganisation behaviour, as described by ψ_P , of Scalmaalloy Batch I is close to 2 which describes a perfect smooth surface. This characteristic is obviously important to obtain a high microstructural quality of the final AM part after SLM.
- Scalmaalloy Batch II powder was already rated critical for use in SLM process after the analysis of the powder particle's morphology, interparticle forces and ψ_P . This criticality was confirmed by material characterising tests as in no test the full potential (as shown for Scalmaalloy Batch I) was achieved.
- A proposed final powder specification for Scalmaalloy shall hence contain the definite description of: bulk surface roughness (e.g. ψ_P), particle shape, particle size distribution, chemical composition, allowed impurities, phases and porosity.
- The evaluation of Scalmaalloy samples out of powder Batch I regarding fracture mechanics revealed an early crack propagation start, but a lower propagation in the upper Paris' regime. Fracture toughness tests yielded a very ductile behaviour.
- SilmagAl powders showed a very tolerant behaviour and are also processable in a broad parameter window.
- Both SilmagAl powder batches obtained equal static tensile properties but the HCF behaviour of Batch II decreases compared to Batch I.

4. Results and discussion

- SimagAl powder Batch I characteristics are comparable to Scalmalloy Batch I and III.

A summary for the final powder specification range for both Al-alloys, Scalmalloy and SilmagAl, is derived from all findings of this thesis and now given in the following Table 4.14.

Table 4.14.: Powder specification range of Scalmalloy and SilmagAl powders

| Scalmalloy | |
|----------------------------|---|
| Particle size distribution | Span ≥ 1 $35 \leq d_{50} \leq 45$ |
| Particle shape | only spheroidal |
| Bulk surface roughness | smooth e.g. measured by surface fractal $1.5 \leq \psi \leq 2.5$ |
| Impurities | according to chemical composition range |
| Phases | size of primary AlSc3 phases $< 20 \mu\text{m}$ |
| Inner particle porosity | $< 0.5\%$ |
| SilmagAl | |
| Particle size distribution | Span ≥ 0.8 $35 \leq d_{50} \leq 45$ |
| Particle shape | only spheroidal |
| Bulk surface roughness | smooth e.g. measured by surface fractal $2 \leq \psi \leq 2.5$ |
| Impurities | according to chemical composition range |
| Phases | none |
| Inner particle porosity | $< 0.5 \%$ |

4. Results and discussion

All process and material characterising tests for Scalmalloy and SilmagAl of this thesis showed that depending on processing route very different mechanical properties can be achieved. Hence, different material specification can be considered for Scalmalloy and SilmagAl. Exemplary extracts of such specifications are given in Tables 4.15 and 4.16 and include the criticality of application in aerospace. It should be differed between principle structural elements (PSE) and non-principle structural elements (non-PSE).

Table 4.15.: Possible material specifications for Scalmalloy manufactured by SLM

| Scalmalloy | | |
|--------------------------------------|---------------------------------------|-------------------------------|
| Part | PSE | non-PSE |
| Manufacturing method | SLM | |
| Heat treatment | 325 °C/4h AND 325 °C/4h/2000bar | 325 °C/(4-8)h HIP optional |
| Static strength | | |
| R _m | 520 MPa | 500 MPa |
| R _{p0.2} | 500 MPa | 480 MPa |
| A | 13 % | 8 % |
| HCF (R = 0.1 K _t = 1.035) | | |
| Cycles: | | |
| 1E06 | 300 MPa | 250 MPa |
| 1E05 | 325 MPa | 275 MPa |
| 1E04 | 400 MPa | 350 MPa |
| Fracture Toughness | | |
| K _{IC} | ≥ 35 MPa√m | ≥ 25 MPa√m |

4. Results and discussion

Table 4.16.: Possible material specifications for SilmagAl manufactured by SLM

| SilmagAl | | |
|--------------------------------------|--|---|
| Part | PSE | non-PSE |
| Manufacturing method | SLM | |
| Heat treatment | 540 °C/2h/1000bar 550 °C/1h + 165 °C/(5-7)h | |
| | | HIP optional 550 °C/1h + 165 °C/(5-7)h |
| Static strength | | |
| R _m | 350 MPa | 300 MPa |
| R _{p0.2} | 300 MPa | 250 MPa |
| A | 8 % | 3 % |
| HCF (R = 0.1 K _t = 1.035) | | |
| Cycles: | | |
| 1E06 | 200 MPa | 125 MPa |
| 1E05 | 225 MPa | 150 MPa |
| 1E04 | 300 MPa | 225 MPa |
| Fracture Toughness | | |
| K _{IC} | ≥ 18 MPa√m | ≥ 12 MPa√m |

5. Conclusion and Outlook

The main goal of the present thesis was to explore the suitability of new Al-alloy options for the Selective Laser Melting (SLM) process and to investigate the interaction between the three process steps; powder, build process and heat treatment.

It has been shown that both material options, Scalmalloy and SilmagAl, benefit from the SLM process opportunities such as high cooling rates. Material properties are gained which are comparable or even slightly better than conventionally used Al-alloys in aerospace.

However, all new findings reported in this thesis, shed new light on the importance of a tight power specification for SLM with regard to obtain a stable process, which consistently generates the same material quality. New characterisation methods which offer, for example, the analysis of the powder's surface roughness after recoating have to be taken into account and described precisely. For Scalmalloy, it was demonstrated, that a surface fractal value ψ_P which is dependent on cohesiveness, particle shape and distribution, indicates favourable processability. A constant smooth weld seam is aimed for, which a jagged powders surface roughness cannot realise, as too many occasions for beam traps are generated. Hence, a predictability of how the weld seam will form is not given. If during SLM the welding mode changes constantly between conduction, transition and deep penetration mode, a homogeneous and predictable weld seam, and hence uniform microstructure, cannot be realised. This means, that a powder specification for Scalmalloy has to be quite tight, as already small deviations from a perfectly suited powder can result in an unstable process and hence turbulent microstructure, decreasing the material performance. However, SilmagAl is more tolerant and shows a very high compensation of non-ideal powder characteristics and a non-ideal heat transfer. A limitation of the powder's characteristics in a powder specification is nevertheless proposed for SilmagAl to ensure a stable process, even though minor deviations from perfect powder constitution can likely be compensated.

Although the discussion in Section 4.4.7 highlights that powder batches of different supplier in different quality levels are indeed processable in a research laboratory environment, is the transformation into an industrial environment for aerospace applications most likely not successful without a well-defined powder material specification. A stable process over multiple builds by utilising the full build height of a machine can not be guaranteed. If the powder quality is not appropriate, a continuous adaption of the process parameters during the SLM manufacturing process itself would be required. But no qualification for aerospace parts can be launched if the processing route is not fixed. Hence, for both material options, the definition of particle size (PS), particle size distribution (PSD), bulk surface roughness (e.g. ψ_P), impurities, phases and inner particle porosity is as mandatory as the chemical composition.

The process analysis demonstrated that significant differences in both material options regarding process stability exist. SilmagAl is stable processable over broad powder configurations and process parameters which might offer industrial interesting high build rates; however,

5. Conclusion and Outlook

Scalmalloy is very sensitive to already small deviations in the powder specification, and suitable parameter combinations do not necessarily offer sufficient build rates. An operating window for Scalmalloy can be described neither by a specific volume energy density (see Equation 2.2), nor by the top view optical analysis of the morphology of single weld paths. The most effective way is to determine, by help of microsections, the welding mode by measuring the weld seam depth and width and to limit the parameters in a way that an aspect ratio of $A < 1$ is achieved. Heat conductivity welding is for both material options, Scalmalloy and SilmagAl, the most stable welding mode which creates a microstructure that exploits its full potential. That does not mean necessarily that transition and deep penetration welding do not create a dense microstructure; rather, that the excessive remelting and large heat input associated with both welding modes will lead to a less perfect microstructure as obtained by heat conductivity welding. And a non-uniform microstructure necessarily will lead to a significant drop in material performance.

It can thus be suggested that different material specifications for each alloy shall be defined which also considers the safety class and criticality of a part. This approach also satisfies suppliers need to open SLM for a broader range of applications. Such material specifications or design allowable values for both material qualities are partially proposed and given in Table 4.15 for Scalmalloy and in Table 4.16 for SilmagAl. All values are deduced from the comprehensive material characterisation (overview given in Table 3.2) for both materials in Section 4.4. The mechanical tests that were performed cover the static tensile strength, high cycle fatigue, fracture toughness, crack growth and crack growth threshold analysis.

5. Conclusion and Outlook

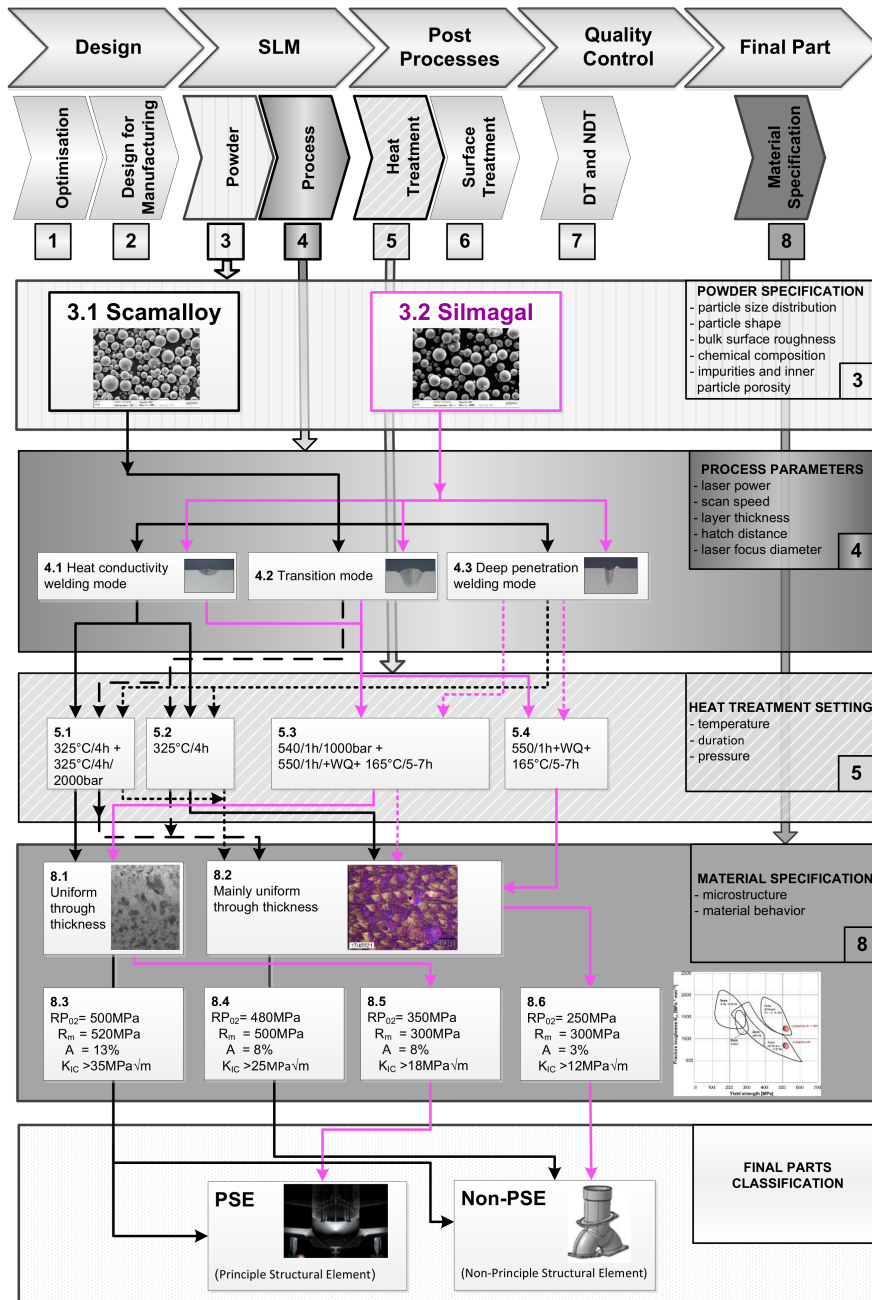


Figure 5.1.: Cause-effect diagram of powder-process-heat treatment relation for different qualification routes for Scalmalloy and SilmagAl

5. Conclusion and Outlook

The second aim of this study was to extrapolate qualification possibilities for Al-alloys, exemplary for Scalmalloy and SilmagAl. These possibilities are explained by help of Figure 5.1. The process chain, as shown in Figure 1.2, is extended by a cause-effect-diagram to illustrate possible paths of qualifying Scalmalloy and SilmagAl manufactured by SLM for aerospace applications. Each investigated process step is numbered (powder = 3, build process = 4, heat treatment = 5 and material specification = 8) and the final parts are distinguished between principle structural element (PSE) and non-principle structural element (non-PSE).

The only possible path for manufacturing Scalmalloy PSE parts requires a well-defined powder (3.1), SLM build process parameters which ensure heat conductivity welding mode (4.1) and a heat treatment with an additional hot isostatic pressing (HIP) step. Although HIP of Scalmalloy at 325°C clearly does not eliminate every gas or process porosity as no diffusion processes are activated, yet does improve mechanical properties as shown in Section 4.4. A uniform microstructure (8.1) consisting of two bands of alternating ultra-fine equiaxed (UFG) and fine columnar (FG) grains is targeted with a homogeneously distribution of full coherent $Al_3(Sc_{(1-x)},Zr_x)$ precipitations. It is assumed that such a microstructure will succeed the high material specifications of 8.3 and Table 4.15.

More options are possible for the manufacturing of non-PSE parts. The second material specification 8.4 (Table 4.15) mitigates the requirements on microstructure (8.2) to mainly uniform through thickness. Both, UFG and FG, bands shall still exist but it is not mandatory to keep a certain volume fraction of these bands. This requirement can be achieved by manufacturing in all three welding modes (4.1, 4.2 and 4.3) and it can be chosen between heat treatment 5.1 or 5.2.

To obtain SilmagAl PSE parts, two different paths are possible and suggested, whereas various paths can be followed for non-PSE. PSE parts of SilmagAl shall be manufactured in either heat conductivity or transition mode 4.1 and 4.2. The T6 heat treatment also includes an additional HIP step in 5.3. A uniform fine eutectic microstructure which consists of fine columnar grains without any large Mg or Si segregation or particles is aimed to achieve the material specification 8.5 or Table 4.16. However, various welding modes and heat treatment combinations are possible to achieve the requirements for non-PSE part material specification 8.4.

Nevertheless, further research should be carried out to expand the above proposed qualification routes to more heat treatment options, e.g. by solely precipitation hardening at 165°C for SilmagAl. Also the influence of a heated platform on the evolution of the microstructure of Scalmalloy and SilmagAl was not investigated so far and should be considered.

Special requirements on the machine configuration exist additionally for processing Scalmalloy regarding gas flow. A non-negligible portion of welding smoke is created, which counteracts uniform welding. Machine configurations presently continue to face trouble in realising a constant laminar gas flow over the complete build plate which would also ensure that only a very low oxygen content remains in the process chamber. Hence, it is necessary to put an additional focus on the gas flow and oxygen level while processing these two aluminium alloys. The entire topic of oxygen contamination of any aluminum alloy during powder atomisation, handling and final processing was not investigated in this thesis, but this source of contamination must also be covered for the aerospace qualification of SilmagAl and Scalmalloy. All material characterising investigations within this thesis are only based on milled coupons. On part basis, the additive manufactured surface will lead to a drop in almost all

5. Conclusion and Outlook

material properties, however, that must be examined in more detail. It is also necessary to follow a conservative approach by adding surface protection to both alloys, as indicated after analysing the corrosion test results. Scalmalloy seems to be vulnerable to corrosion attack if a, so far undefined, defect or porosity level remains in the microstructure and if it is exposed to elevated temperatures. Especially the fatigue crack propagation behaviour of Scalmalloy shows that small sharp cracks, induced by small corrosion pits or any other flaws caused by in-service usage, may lead to early structural failure. The entire surface post-build treatment of both Al-alloy options is a wide-ranging topic that requires further investigations.

A. Appendix

A.1. Powder analysis

A.1.1. Particle morphology

Microsectional and SEM images for particle morphology analysis

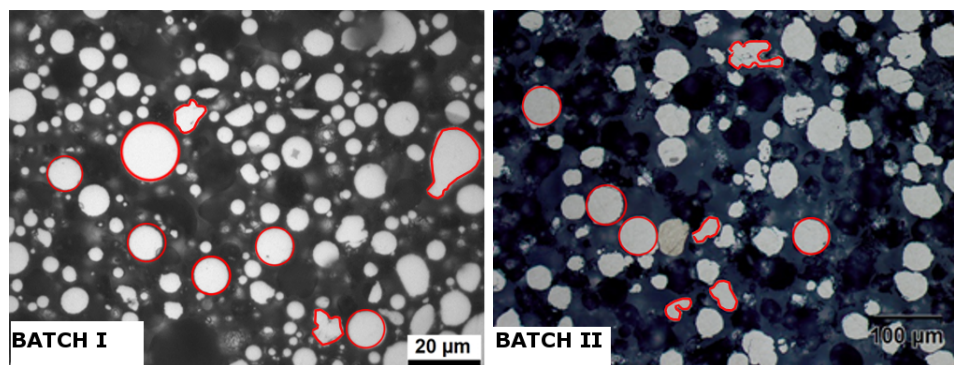


Figure A.1.: Exemplary microsections of Scalmalloy powder Batches with highlighted examples for spheroidal and/or nodular particles

A. Appendix

Mechanical influences / dented spots at different locations in Scalmalloy powder Batches II, IV and V.

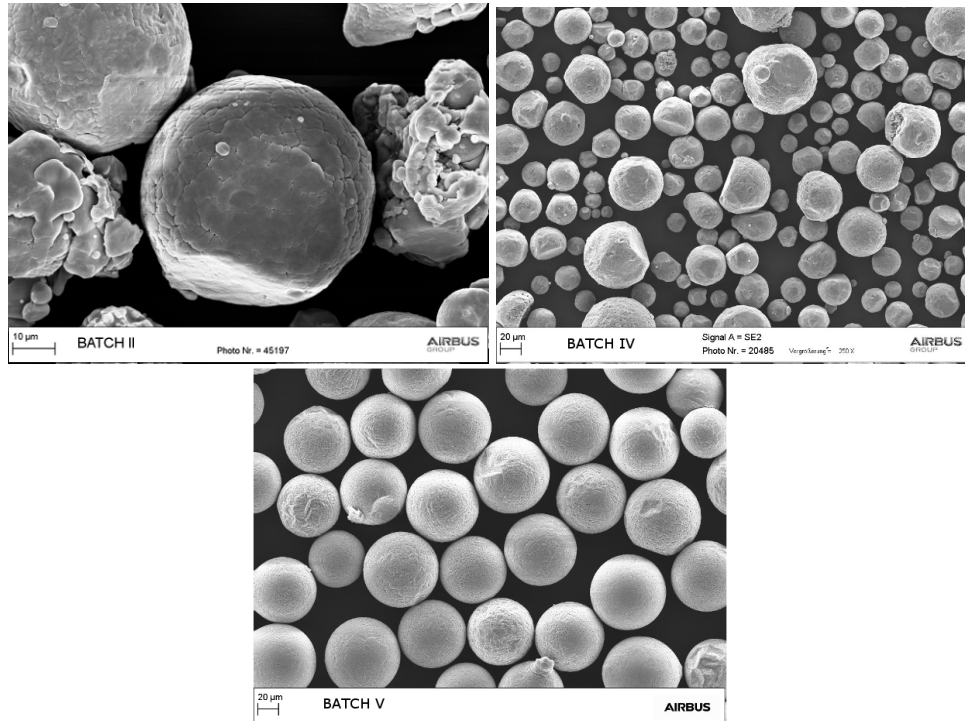


Figure A.2.: Dented spots on the particles surface in Scalmalloy powder Batches II, IV and V

A.1.2. Particle size distribution and particle size

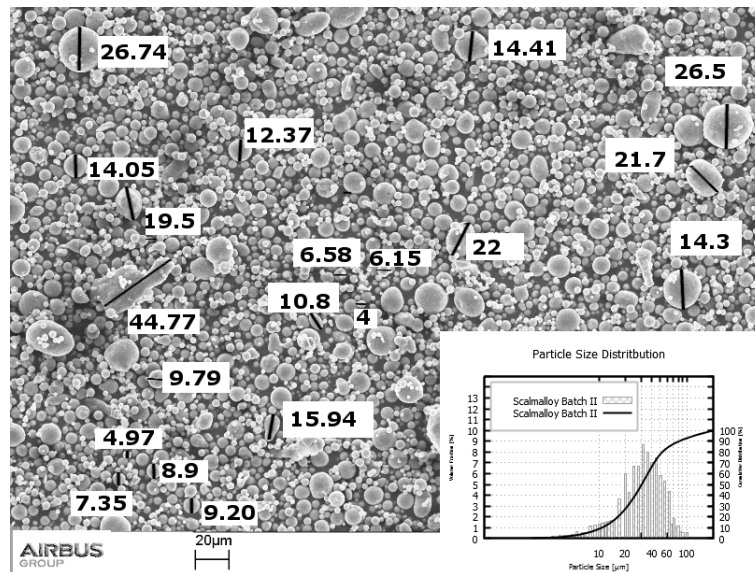


Figure A.3.: Scalmaalloy Batch I - Correlation of PS measurements with SEM picture analysis

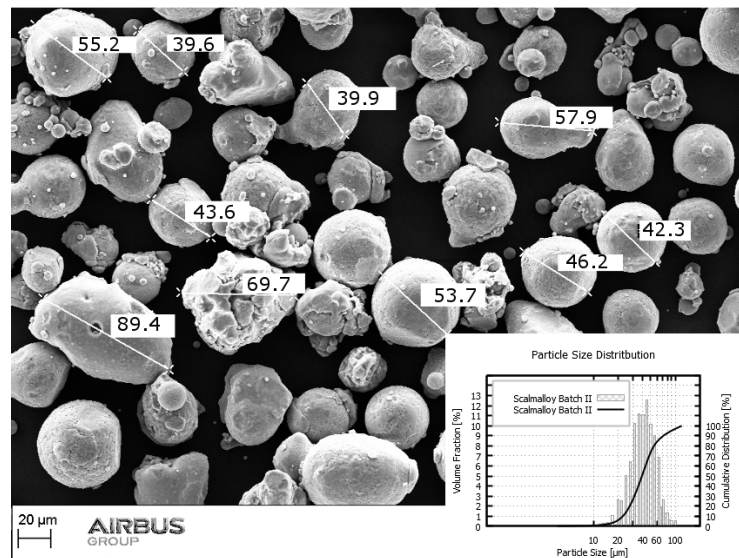


Figure A.4.: Scalmaalloy Batch II - Correlation of PS measurements with SEM picture analysis

A. Appendix

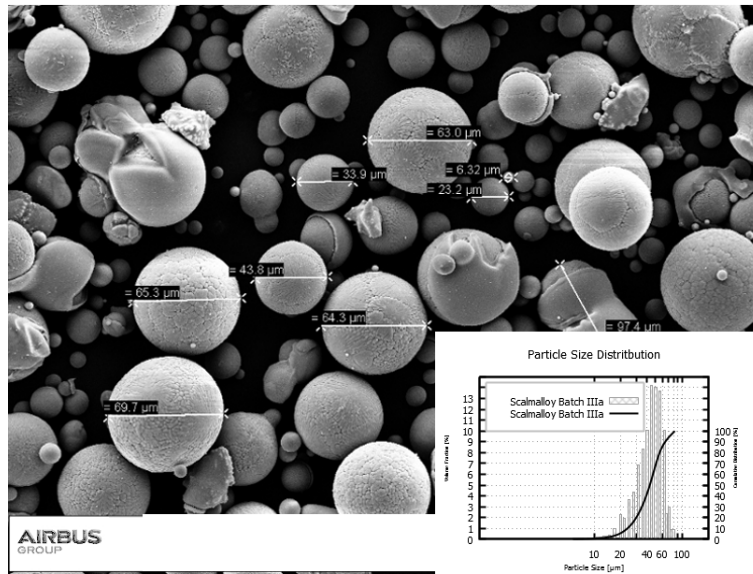


Figure A.5.: Scalmalloy Batch IIIa - Correlation of PS measurements with SEM picture analysis

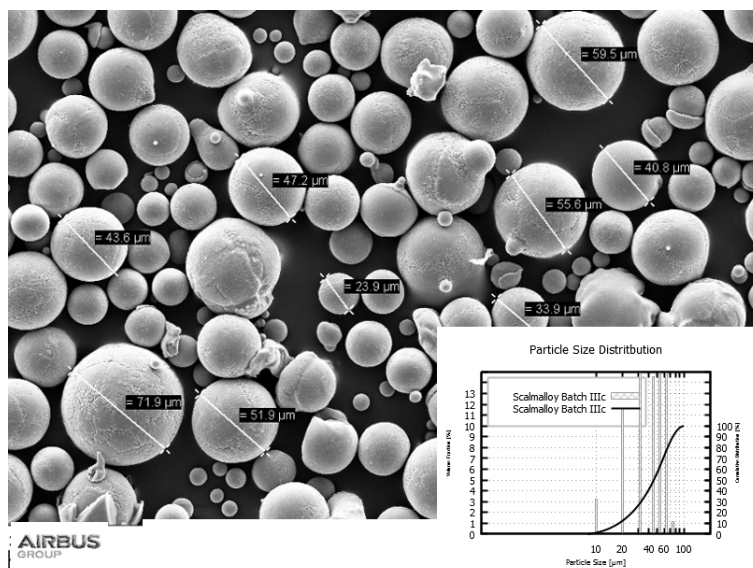


Figure A.6.: Scalmalloy Batch IIIb - Correlation of PS measurements with SEM picture analysis

A. Appendix

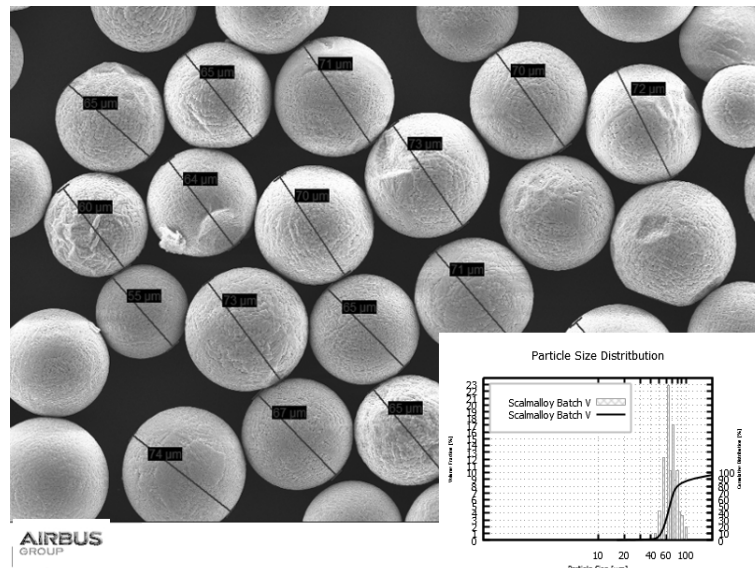


Figure A.7.: Scalmalloy Batch V - Correlation of PS measurements with SEM picture analysis

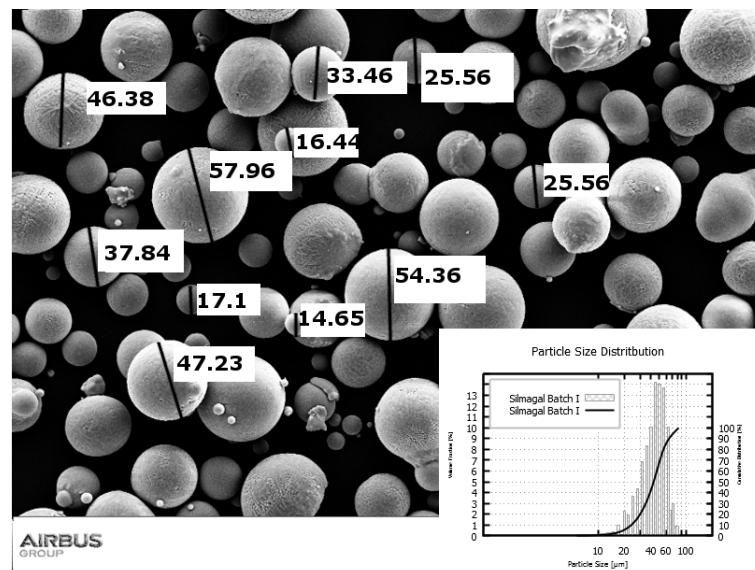


Figure A.8.: SilmagAl powder Batch I - Correlation of PS measurements with SEM picture analysis

A. Appendix

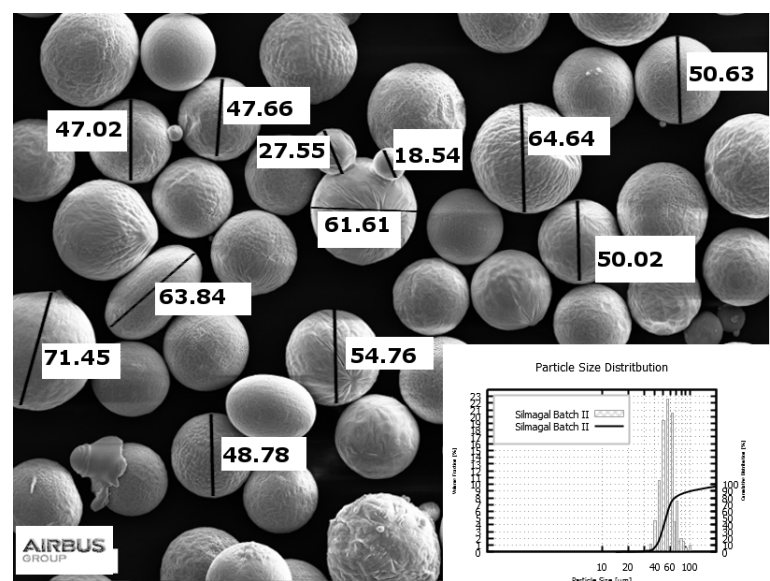
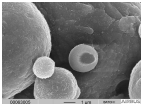
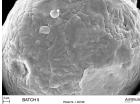
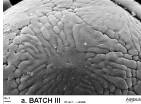
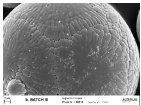
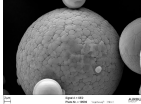
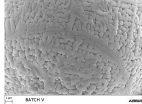
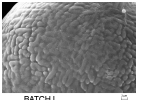



Figure A.9.: SilmagAl powder Batch II - Correlation of PS measurements with SEM picture analysis

Table A.1.: Dendritical surface structure of Scalmalloy and SilmagAl powders

| Batch I | Batch II | Batch III | Batch IV | Batch V |
|---|---|--|--|---|
| Scalmalloy | | | | |
|  |  |   |  |  |
| SilmagAl | | | | |
|  |  | | | |

A.1.3. Impurities analysis

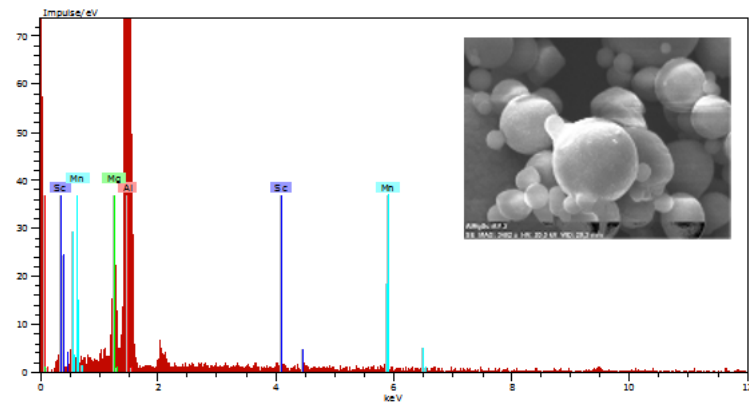


Figure A.10.: Scalma alloy powder Batch I - SEM-EDS analysis

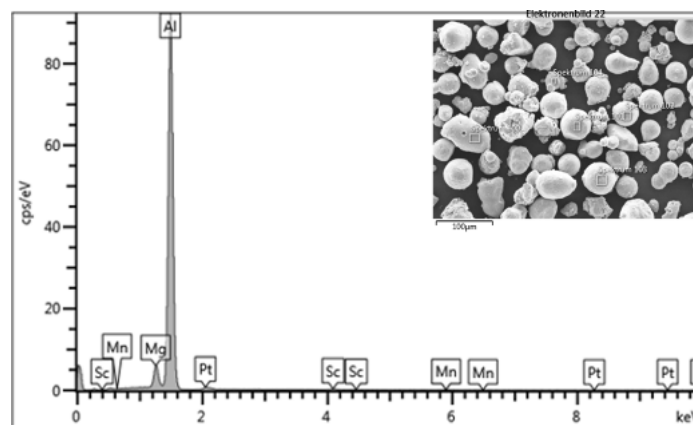


Figure A.11.: Scalmalloy powder Batch II - SEM-EDS analysis

A. Appendix

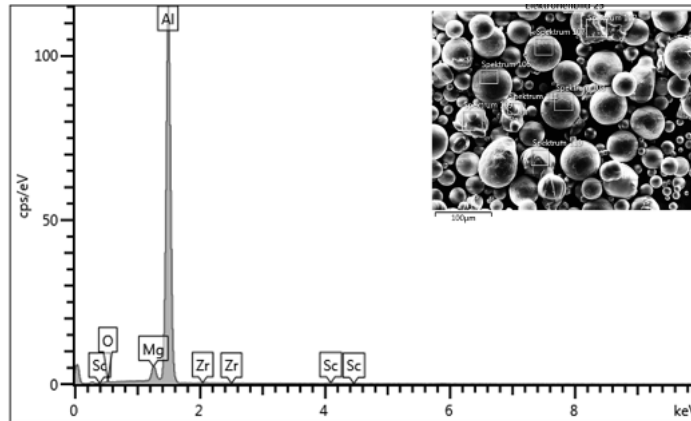


Figure A.12.: Scalmalloy powder Batch III a - SEM-EDS analysis

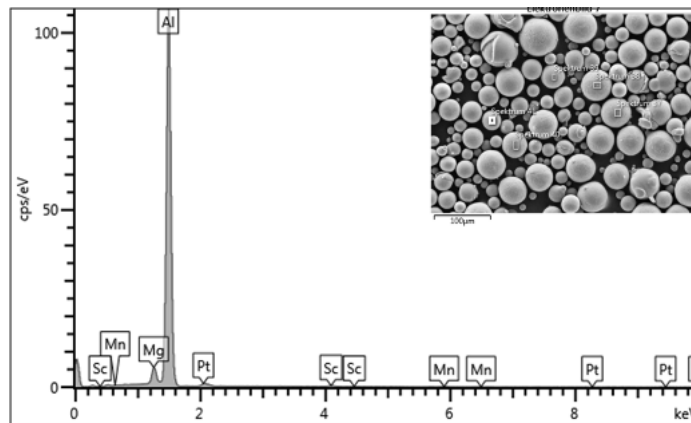


Figure A.13.: Scalmalloy powder Batch III b - SEM-EDS analysis

A. Appendix

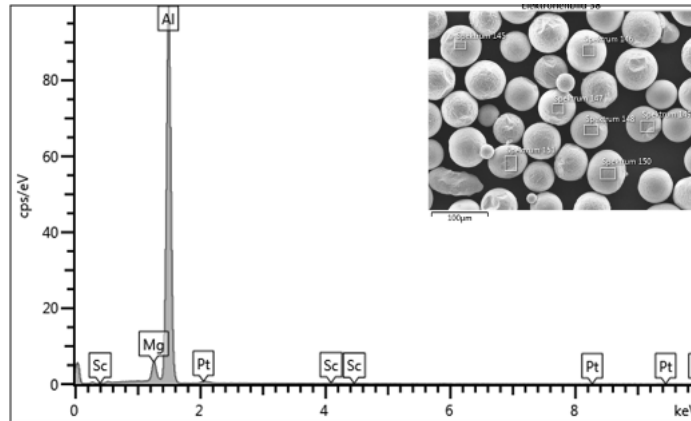


Figure A.14.: Scalmaalloy powder Batch V - SEM-EDS analysis

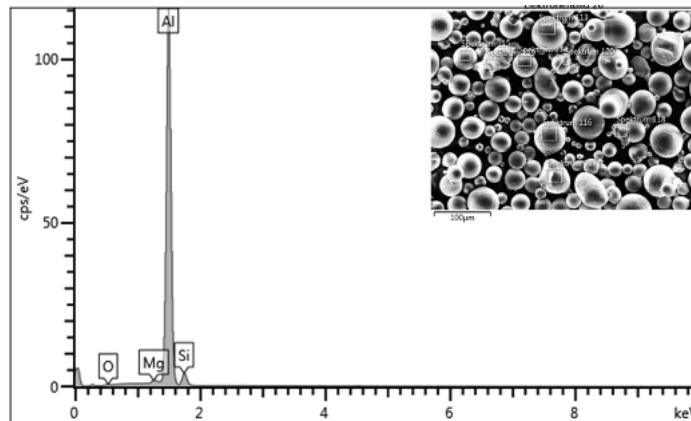


Figure A.15.: SilmagAl powder Batch I - SEM-EDS analysis

A. Appendix

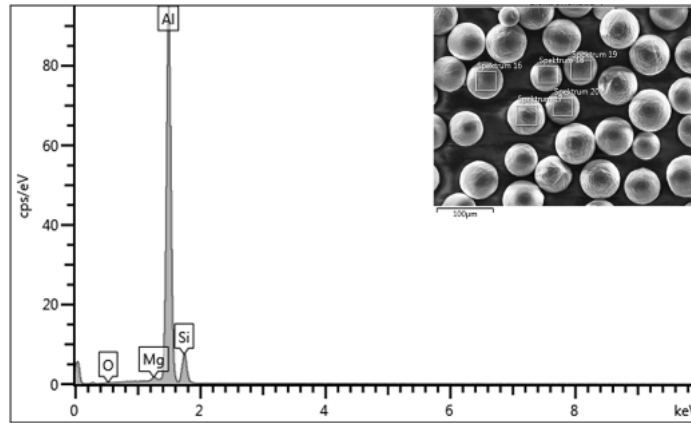


Figure A.16.: SilmagAl powder Batch II - SEM-EDS analysis

A.2. Process analysis

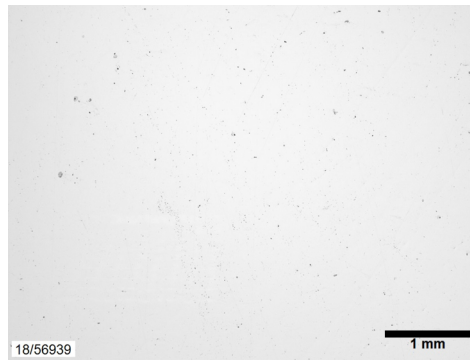


Figure A.17.: Microsection of test sample manufactured out of Scalmaalloy powder Batch IIIb, processed at $P_L = 370$ W, $h = 100$ μm, $z = 30$ μm and $v_s = 1600$ mm/s

A.3. Material characterisation

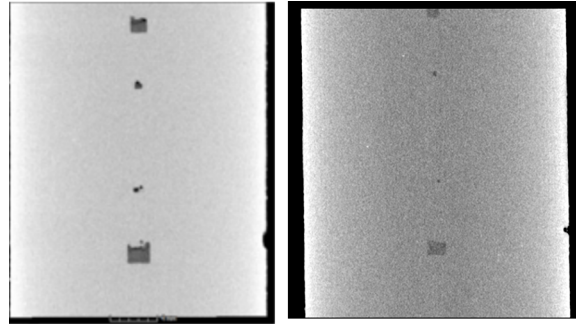


Figure A.18.: CT scan of cylindrical test specimen with artificial defects before (left) and (right) HIP at 325°C/4h/1000bar; manufactured of Scalmalloy Batch II at $z = 30 \mu\text{m}$, $P_L = 400 \text{ W}$, $v_s = 800 \text{ mm/s}$ and $h = 100 \mu\text{m}$

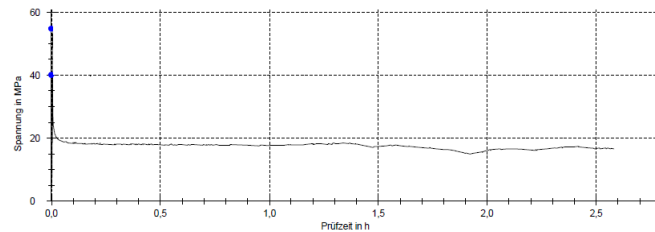


Figure A.19.: Stress relaxation tests at 300 °C of Scalmalloy Batch I specimen, built at $z = 30 \mu\text{m}$, $P_L = 195 \text{ W}$, $v_s = 300 \text{ mm/s}$ and $h = 100 \mu\text{m}$ revealing the low thermal strength of Scalmalloy

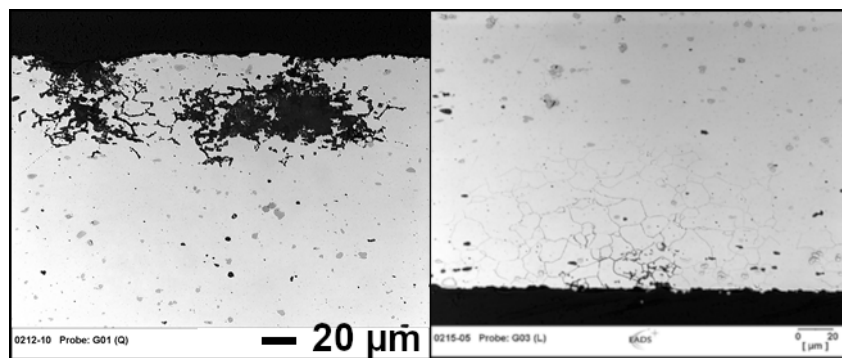


Figure A.20.: Microsection of 5083 (sensitised at 150 °C / 240h) after AIC testing

A. Appendix

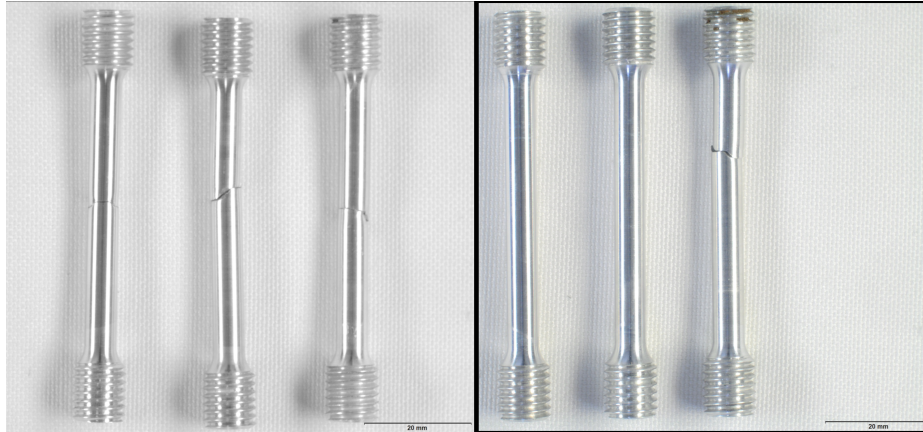


Figure A.21.: Overview of Scalmaalloy Batch I test coupons after SCC testing

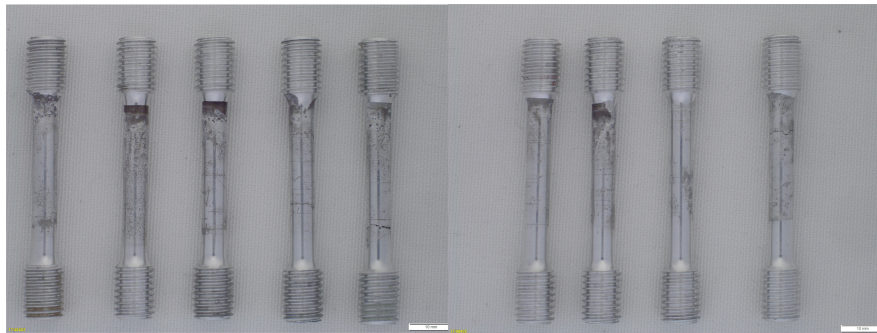


Figure A.22.: Overview of Silmagal Batch I test coupons after SCC testing

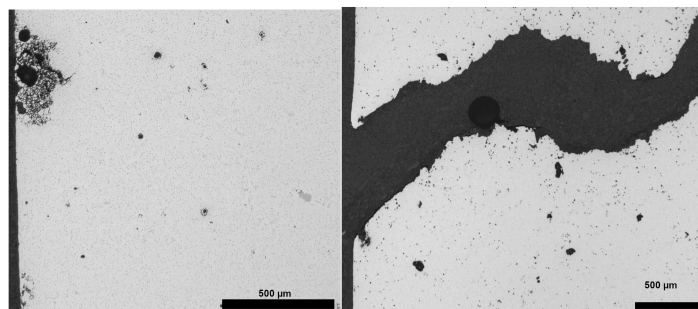


Figure A.23.: Microsection of Scalmaalloy Batch I failed SCC test coupon

A. Appendix

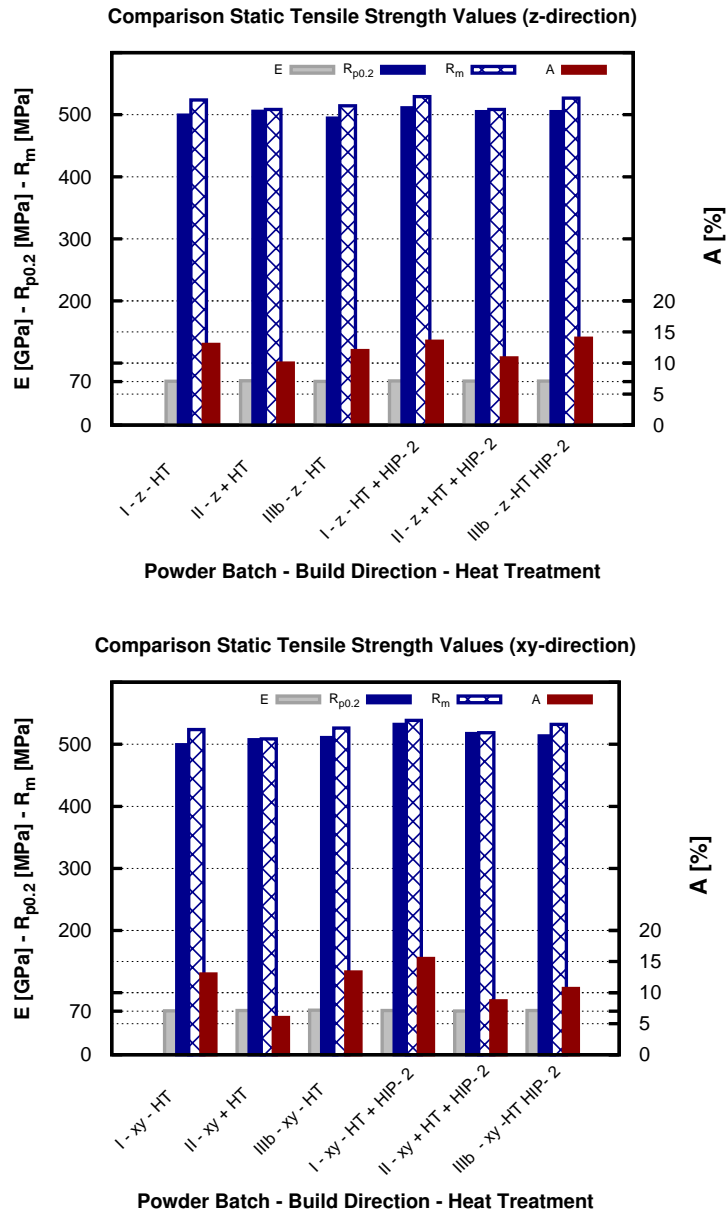


Figure A.24.: Summary of all static tested Scalmalloy powder Batches for build direction xy and z

A. Appendix

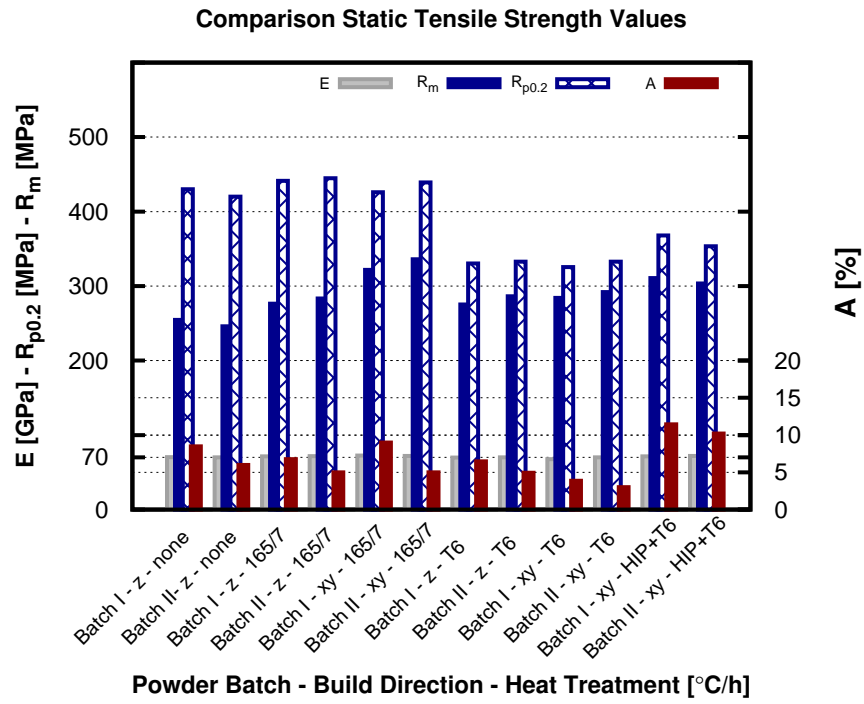


Figure A.25.: Summary of all static tested SilmagAl powder Batches for build direction xy and z

Bibliography

- [1] D. Buchbinder and W. Meiners. AluGenerativ: Generative Fertigung von Aluminiumbauteilen für die Serienproduktion. Technical report, Fraunhofer ILT, 2010.
- [2] S. Sterk. EU-Project: Coalsece² - Deliverable D2.10, Final report on validation & assessment of improved fixed leading edge structural details. Technical report, NLR, 2012.
- [3] Airbus APWorks GmbH. <http://www.apworks.de>, Retrieved from 11-11-2017.
- [4] K. Schmidtke, F. Palm, A. Hawkins, and C. Emmelmann. Process and Mechanical Properties: Applicability of a Scandium modified Al-alloy for Laser Additive Manufacturing. *Physics Procedia*, 12:369–374, 2011.
- [5] A.B. Spierings, K. Dawson, M. Voegtlin, F. Palm, and P.J. Uggowitzer. Microstructure and mechanical properties of as-processed scandiummodified aluminium using selective laser melting. *CIRP Annals - Manufacturing Technology*, 65:213–216, 2016.
- [6] A.B. Spierings, K. Dawson, K. Kern, F. Palm, and K. Wegener. SLM-processed Sc- and Zr- modified Al-Mg alloy: Mechanical properties and microstructural effects of heat treatment. *Materials Science and Engineering: A*, 701:264–273, July 2017.
- [7] A.B. Spierings, K. Dawson, T. Heeling, P.J. Uggowitzer, R. Schäublin, F. Palm, and K. Wegener. Microstructural features of Sc- and Zr-modified Al-Mg alloys processed by selective laser melting. *Materials and Design*, 115:52–63, 2017.
- [8] E.A. Jägle, Z. Sheng, L.Wu, L. Lu, J. Risse, A. Weisheit, and D. Raabe. Precipitation Reactions in Age-Hardenable Alloys During Laser Additive Manufacturing. *The Journal of The Minerals, Metals & Materials Society (TMS)*, 68(3):943–949, 2016.
- [9] K. Schmidtke and F. Palm. Exceptional grain refinement in directly built up Sc-modified AlMg-alloys is promising a quantum leap in ultimate light weight design. *Proceedings of the 9th International Conference: Trends in Welding Research 2012*, 2012.
- [10] K. Schmidtke, F. Palm, V. Holzinger, and C. Emmelmann. Microstructure and mechanical properties of additive manufactured aluminium alloys Scalmalloy and Silmagal. In *Proceedings Lasers in Manufacturing*, 2017.
- [11] J.H. Rao, Y. Zhang, X. Fang, Y. Chen, X. Wu, and C.H.J. Davies. The origins for tensile properties of selective laser melted aluminium alloy A357. *Additive Manufacturing*, 17:113–122, 2017.

Bibliography

- [12] D. Buchbinder. *Selective Laser Melting von Aluminiumgusslegierungen*. PhD thesis, RWTH Aachen, 2013.
- [13] N. E. Uzan, R. Shneck, O. Yeheskel, and N. Frage. Fatigue of AlSi10Mg specimens fabricated by additive manufacturing selective laser melting (AM-SLM). *Materials Science and Engineering A*, 704:229–237, 2017.
- [14] I. Gison, D. Rosen, and D. Stucker. *Additive Manufacturing Technologies*. Springer, 2014.
- [15] J. Kranz. *Methodik und Richtlinien für die Konstruktion von laseradditiv gefertigten Leichtbaustrukturen*. PhD thesis, TU Hamburg-Harburg, 2017.
- [16] SLM Solutions Group AG. <https://slm-solutions.de/>, Retrieved from 04-11-2017.
- [17] Electro Optical Systems (EOS) GmbH. www.eos.info/en, Retrieved from 04-11-2017.
- [18] Concept Laser. GE Additive company. <https://www.concept-laser.de>, Retrieved from 04-11-2017.
- [19] MATSUURA Machinery GmbH. <https://www.matsuura.de>, Retrieved from 05-11-2017.
- [20] Deutsches Institut für Normung. DIN EN ISO/ASTM 52900 - Additive manufacturing -General principles -Terminology, 2017.
- [21] Deutsches Institut für Normung. DIN EN ISO 17296-2 Additive manufacturing - General principles - Part 2: Overview of process categories and feedstock, 2015.
- [22] Verein deutscher Ingenieure e.V. VDI 3404, Generative Fertigungsverfahren: Rapid-Technologien (Rapid Prototyping), 2009.
- [23] A. Gebhardt. *Additive Fertigungsverfahren*. Hanser Verlag, 2016.
- [24] M. Petersen. *Lasergenerieren von Metall-Keramik-Verbundwerkstoffen*. PhD thesis, TU Hamburg-Harburg, 2006.
- [25] W. Meiners. *Direktes Selektives Laser Sintern einkomponentiger metallischer Werkstoffe*. PhD thesis, RWTH Aachen, 1999.
- [26] J. Steinberger. *Optimierung des Selektiven-Laser-Sinterns zur Herstellung von Feingussteilen für die Luftfahrtindustrie*. PhD thesis, TU München, 2001.
- [27] M. Munsch. *Reduzierung von Eigenspannungen und Verzug in der laseradditiven Fertigung*. PhD thesis, TU Hamburg-Harburg, 2013.
- [28] J.-St. Hötter, M. Fateri, and A. Gebhardt. Prozessoptimierung des SLM Prozesses mit hochreflektierenden und thermisch sehr gut leitenden Materialien durch systematische Parameterfindung und begleitende Simulation am Beispiel von Silber. *RTejournal*, 9, 2012.

Bibliography

- [29] M.A. Eisen. *Optimierte Parameterfindung und prozessorientiertes Qualitätsmanagement für das Selective Laser Melting Verfahren*. PhD thesis, Universität Duisburg Essen, 2009.
- [30] D. Gu and Y. Shen. Balling phenomena in direct laser sintering of stainless steel powder: Metallurgical mechanisms and control methods. *Materials and Design*, 30:2903–2910, 2009.
- [31] J. Rapp. *Laserschweisseignung von Aluminiumwerkstoffen für Anwendungen im Leichtbau*. PhD thesis, Universität Stuttgart, 1996.
- [32] M. Klassen. *Prozessdynamik und resultierende Prozessinstabilitäten beim Laserstrahlschweißen von Aluminiumlegierungen*. PhD thesis, Universität Bremen, 2000.
- [33] C. Schinzel. *Nd:YAG-Laserstrahlschweißen von Aluminiumwerkstoffen für Anwendungen im Automobilbau*. PhD thesis, Universität Stuttgart, 2002.
- [34] C. Heimerdinger. *Laserstrahlschweißen von Aluminiumlegierungen für die Luftfahrt*. PhD thesis, Universität Stuttgart, 2003.
- [35] Inc.s Amada Miyachi America. AMADA Laser Welding Fundamentals. <http://www.amadamiyachi.com>, Retrieved from 03-04-2018.
- [36] E. Brandl. *Microstructural and mechanical properties of additive manufactured titanium (Ti-6Al-4V) using wire*. PhD thesis, BTU Cottbus, 2010.
- [37] A.J. Birnesser. *Prozessregelung beim Laserstrahlschweißen*. PhD thesis, Universität Stuttgart, 2011.
- [38] M. Beck. *Modellierung des Lasertiefschweißens*. PhD thesis, Universität Stuttgart, 1996.
- [39] M.C. Tsai and S. Kou. Marangoni convection in weld pools with a free surface. *International Journal for numerical methods in fluids*, 9(12):1503 – 1516, 1989.
- [40] R. Poprawe. *Lasertechnik für die Fertigung*. Springer, 2005.
- [41] S. Kou. *WELDING METALLURGY*. John Wiley & Sons, Inc., Hoboken, New Jersey., 2003.
- [42] B. Ilchner and R. Singer. *Werkstoffwissenschaften und Fertigungstechnik*. Springer, 2009.
- [43] L.A. Willey. Aluminum scandium alloy. USA patent (US3619181 A), 1971.
- [44] S. Michelfeit. *Werkstoffgesetze einer AlSi-Gusslegierung unter Hochtemperaturbeanspruchung in Abhängigkeit des Werkstoffzustandes*. PhD thesis, TU Darmstadt, 2012.
- [45] ASM editorial advisory board, editor. *ASM Specialty Handbook: Aluminum and Aluminum Alloys*. ASM International, 1993.

Bibliography

- [46] C. Kammer. *Aluminium Taschenbuch Band 1*. Aluminium Zentrale Düsseldorf, 1995.
- [47] F. Ostermann. *Anwendungstechnologie Aluminium*. Springer Verlag, 2007.
- [48] R. Goswami, G. Spanos, P.S. Pao, and R.L. Holtz. Precipitation behaviour of the β phase in Al-5083. *Materials Science and Engineering: A*, pages 1089–1095, 2009.
- [49] J. Yan, N.M. Heckman, L. Velasco, and A. M. Hodge. Improve Sensitization and corrosion resistance of an Al-Mg alloy by optimization of grain boundaries. *Scientific Reports* www.natur.com, 2016.
- [50] R.K Gupta, R. Zhang, C.H.J. Davies, and N. Birbilis. Influence of Mg content on the sensitization and corrosion of Al-xMg (-Mn) alloys. *Corrosion*, 69(11):1081–1087, 2013.
- [51] L.S. Toropova, D.G. Eskin, and M.L. Kharakterova und T.V. Dobatkina. *Advanced Aluminum Alloys Containing Scandium*. Gordon and Breach Science Publishers, 1998.
- [52] T. Richardson, editor. *Shreir's Corrosion*. Elsevier B.V., 2009.
- [53] B.A. Parker, Z.F. Zhou, and P. Nolle. The effect of small additions of scandium on the properties of aluminium alloys. *Journal of Material Science*, pages 452–458, 1995.
- [54] J. Roystein and N. Ryum. Scandium in aluminium alloys. *International Materials Reviews*, 50:19–44, 2005.
- [55] G. Tempus and K.H. Rendigs. Neue schweisssbare Aluminiumlegierungen. *DGLR-Tagung Bremen*, 1998.
- [56] C. Fuller. *Temporal Evolution of the Microstructures of Al(Sc,Zr) Alloys and Their Influences on Mechanical Properties*. PhD thesis, Northwestern University, 2003.
- [57] V.G. Davydov, V.L. Elagin, V.V. Zakharov, and T.D. Rostova. Nonferrous Metals and Alloys - Alloying aluminum alloys with Sc and Zr additives. *Metal Science and Heat Treatment*, 1996.
- [58] J. L. Murray. The Al-Sc (aluminium-scandium) system. *Journal of Phase Equilibria*, 19(4):380–384, 1998.
- [59] C. Sigli. Zirconium Solubility in Aluminium Alloys. *Proceedings of the 9th International Conference on Aluminium Alloys*, pages 1353–1358, 2004.
- [60] C.B Fuller and D. N. Seidman. Temporal evolution of the nanostructure of Al(Sc,Zr) alloys: Part II-coarsening of $Al_3(Sc_{1-x}Zr_x)$ precipitates. *Acta Materialia*, 53:5415–5428, 2005.
- [61] A.F. Norman, P.B. Prangnell, and R.S. McEwen. The solidification behaviour of dilute Aluminium-Scandium Alloys. *Acta materialia*, 46(16):5715–5732, 1998.
- [62] A. Tolley, V. Ramilovic, and U. Dahmen. Segregation in $Al_3(Sc,Zr)$ precipitates in Al-Sc-Zr alloys. *Scripta Materialia*, 53:621–625, 2005.

Bibliography

- [63] V. Radmilovic, A. Tolley, E.A. Marquis, M.D. Rossell, Z. Lee, and U. Dahmen. Monodisperse $Al_3(LiScZr)$ core/shell precipitates in Al alloys. *Scripta Materialia*, 58:529–532, 2008.
- [64] Key to Metals AG. Melting and Casting of Copper and Aluminum Alloys: Part One. <http://www.totalmateria.com/>, Retrieved from 10-02-2018.
- [65] ASM editorial advisory board, editor. *ASM Handbook Powder Metal Technologies and Applications*. ASM International, 1999.
- [66] S. Dietrich, M. Wunderer, A. Huissel, and M.F. Zäh. A New Approach For A Flexible Powder Production For Additive Manufacturing. *16th Maching Innovations Conference for Aerosapce Industry - MIC*, pages 88–95, 2016.
- [67] E. Louvis, P. Fox, and C.J. Sutcliffe. Selective laser melting of aluminium components. *Journal of Materials Processing Technology*, pages 275–284, 2011.
- [68] The UK Centre for Materials Education. Collaborative Open Resource Environment for Materials. <http://core.materials.ac.uk>, Retrieved from 01-12-2017.
- [69] Tallinn University of Technology. Grain boundary strengthening. https://www.ttu.ee/public/s/Sustainable_Energetics/materials/Engineering_for_Natural_Scientist/_L7_Strengthening_131.pdf, Retrieved from 01-12-2017.
- [70] Deutsches Instiut für Normung. DIN 65122 Luft- und Raumfahrt: Pulver zur Verwendung für die additive Fertigung mittels Pulverbettverfahren: Technische Lieferbedingungen. Deutsches Institut für Normung, 2017.
- [71] J. Tomas. *Transport und Lagerung von Partikelsystemen*, chapter 6, pages 361–431. Institut für Verfahrenstechnik, 2007.
- [72] W. Schatt, K.-P. Wieters, and B. Kieback. *Pulvermetallurgie*. Springer-Verlag Berlin Heidelberg, 2007.
- [73] A.J. Yule and J.J. Dunkely. *Atomisation of Melts*. Oxford University Press, 1994.
- [74] F. v. Lenel. *Powder Metallurgy*. Metal Powder Industries Federation, 1980.
- [75] Sapa Profiles UK; part of Sapa Group. <http://www.aluminiumdesign.net/why-aluminium/properties-of-aluminium/>, Retrieved from 07-09-2017.
- [76] Deutsches Institut für Normung. DIN EN ISO 8044 Corrosion of metals and alloys - basic terms and definitions, 2015.
- [77] T.W. Jelinek. *Oberflächenbehandlung von Aluminium*. Eugen G. Leuze Verlag, 1997.
- [78] ASTM International. ASTM G 67 Standard Test Method for Determining the Susceptibility to Intergranular Corrosion of 5xxx Series Aluminum Alloys by Mass Loss After Exposure to Nitric Acid (NAML Test), 2013.

Bibliography

- [79] ASTM International. ASTM G 66 Standard Test Method for Visual Assessment of Exfoliation Corrosion Susceptibility of 5xxx Series aluminum alloys (ASSET test), 2013.
- [80] ASTM International. ASTM G 193 Standard Terminology and Acronyms Relating to Corrosion, 2012.
- [81] J.E. Shigley and C.R. Mischke. *Mechanical Engineering Design*. McGraw-Hill, 2001.
- [82] Deutsches Institut für Normung. DIN EN 6072 Luft- und Raumfahrt - Metallische Werkstoffe - Prüfverfahren - Ermüdungstest mit konstanter Amplitude, 2011.
- [83] ASTM International. ASTM E399 Standard Test Method for Linear-Elastic Plane Strain Fracture Toughness K_{IC} of Metallic Materials, 2012.
- [84] ASM International Handbook Committee, editor. *ASM Handbook Fatigue and Fracture*. ASM International, 1996.
- [85] J.G. Kaufman, R.L. Moore, and P.E. Schilling. Fracture toughness of structural aluminum alloys. *Engineering Fracture Mechanics*, 2(3):197–210, 1967.
- [86] ASTM International. ASTM E647 Standard Test Method for Measurement of Fatigue Crack Growth Rates, 2015.
- [87] ASTM International. ASTM B 964 Standard Test Methods for Flow Rate of Metal Powders Using the Carney Funnel, 2009.
- [88] Mercury Scientific Inc. Revolution Powder Analyzer. <http://mercuryscientific.com/instruments/revolution-powder-analyzer>, Retrieved from 04-03-2018.
- [89] A.B. Spierings, M. Voeglin, T. Bauer, and K. Wegener. Powder flowability characterisation methodology for powder-bed based metal additive manufacturing. *Progress in Additive Manufacturing*, 1:9–20, 2016.
- [90] D. Geldart, N. Harnby, and A.C. Wong. Fluidization of cohesive powders. *Powder Technology*, 37:25–37, 1984.
- [91] Deutsches Institut für Normung. DIN EN ISO 3923-1: 2010 1-08 Metallic powders determination of apparent density, 2010.
- [92] Deutsches Institut für Normung. DIN EN ISO 3252 Powder metallurgy - Vocabulary, 1999.
- [93] ASTM International. ASTM B 822 Standard Test Method for Particle Size Distribution of Metal Powders and Related Compounds by Light Scattering, 2010.
- [94] International Organization for Standardization. ISO 13320 Particle Size Analysis - Laser diffraction methods, 2009.
- [95] Fritsch GmbH Manufacturers of Laboratory Instruments. *Manual Laser particle Sizer analysette 22 COMPACT*. Fritsch GmbH.

Bibliography

- [96] Sintavia. www.sintavia.com, Retrieved from 15-11-2017.
- [97] D. Schwarze. Selective Laser Melting: Eine produktive Fertigungstechnologie. In *Jubiläumsveranstaltung 20. Fachtagung Rapid Prototyping*, November 2015.
- [98] D.L. Zhang, L.H. Zheng, and D.H. St John. Effect of a short solution treatment time on microstructure and mechanical properties of modified Al-7wt.%Si-0.3wt.%Mg alloy. *Journal of Light Metals*, 2:27–36, 2002.
- [99] W. Li, S. Li, J. Liu, A. Zhang, Y. Zhou, Q. Wei, C. Yan, and Y. Shi. Effect of heat treatment on AlSi10Mg alloy fabricated by selective laser melting: Microstructure evolution, mechanical properties and fracture mechanism. *Materials Science and Engineering A*, 663:116–125, 2016.
- [100] Deutsches Institut für Normung. DIN EN ISO 2921 Normbegrifflichkeiten für die Additive Fertigung - Koordinatensysteme und Prüfmethodologien, 2017.
- [101] Aluminium Association, editor. *Aluminum Standards and Data 1997*. The Aluminum Association, 1997.
- [102] ASTM International. ASTM G44 Standard Practice for Exposure of Metals and Alloys by Alternating Immersion in Neutral 3.5 % Sodium Chloride Solution, 1999.
- [103] Deutsches Institut für Normung. DIN 50125 Test pieces for tensile testing of metallic materials, 2004.
- [104] Deutsches Institut für Normung. DIN EN 2002-001 Luft- und Raumfahrt - Metallische Werkstoffe - Prüfverfahren Teil 1: Zugversuch bei Raumtemperatur, 2006.
- [105] Deutsches Institut für Normung. DIN EN ISO 6892 - 1 Metallic materials - Tensile testing Part 1: Method of test at room temperature, 2009.
- [106] ASTM International. ASTM E466 Conducting Force Controlled Constant Amplitude Axial Fatigue Tests of Metallic Materials, 2007.
- [107] H. Blumenauer and G. Pusch. *Technische Bruchmechanik*. VEB Deutscher Verlag für Grundstoffindustrie Leipzig, 1982.
- [108] M.O. Speidel. 6th European Non-Ferrous Metals Industry Colloquium of the CAEF. In *Proceedings*, volume 6, 1982.
- [109] M. Tiryakioglu. Fracture toughness potential of cast Al-7%Si-Mg alloys. *Materials Science and Engineering A*, 497(1-2):512–514, 2008.
- [110] Mercury Scientific Inc. *Revolution Powder Analyzer User Manual*, August 2014.
- [111] V. Seyda, D. Herzog, and C. Emmelmann. Relationship between powder characteristics and part properties in laser melting of Ti-6Al-4V, and implications on quality. *Journal of Laser Applications*, 29(2), 2017.

Bibliography

- [112] M. Schmid. *Selektives Lasersintern (SLS) mit Kunststoffen: Technologie, Prozesse und Werkstoffe*. Carl Hanser Verlag GmbH Co KG, 2015.
- [113] J. Dawes, R. Bowerman, and R. Trepleton. Introduction to the Additive Manufacturing Powder Metallurgy Supply Chain. *Johnson Matthey technology review*, 59(3):243–256, 2015.
- [114] Y. Milman. Structure and mechanical behavior of Al-Sc alloys. *Materials Science Forum*, 519-521:567–572, 2006.
- [115] R. Schneider. *Weldability of high-strength aluminum alloys for aerospace applications*. PhD thesis, TU Wien, 2008.
- [116] G. Schulze. *Die Metallurgie des Schweissens*. Springer, 2010.
- [117] K. Hyde. *The Addition of Scandium to Aerospace Castings*. PhD thesis, University of Manchester, 2001.
- [118] J. Taendl, A. Orthacker, H. Amenitsch, G. Kothleitner, and C. Poletti. Influence of the degree of scandium supersaturation on the precipitation kinetics of rapidly solidified Al-Mg-Sc-Zr alloys. *Acta Materialia*, 117:43–50, 2016.
- [119] K. Hyde, A. Norman, and P. Pragnell. The effect of cooling rate on the morphology of primary Al_3Sc intermetallic particles in Al-Sc alloys. *Acta Materialia*, 49:1327–1337, 2001.
- [120] A.B. Spierings, K. Dawson, P.J. Uggowitzer, and K. Wegener. Influence of SLM scan-speed on microstructure, precipitation of Al_3Sc particles and mechanical properties in Sc- and Zr-modified Al-Mg alloys. *Materials and Design*, 140:134–143, 2018.
- [121] Wikipedia. Zener pinning. www.wikipedia.com, Retrieved from 01-01-2018.
- [122] E. Nes, N. Ryum, and O. Hunderi. On the Zener drag. *Acta Metallurgica*, 33(1):11–22, 1985.
- [123] K.L. Kendig and D.B. Miracle. Strengthening mechanism of an Al-Mg-Sc-Zr alloy. *Acta Materialia*, 50:4165–4175, 2002.
- [124] T. Vilaro. *Fabrication directe de pièces aéronautiques et spatiales en Nimonic 263 et A360 par le procédé de fusion sélective par laser : approche thermique, microstructurale et mécanique*. PhD thesis, Paris Tech, 2011.
- [125] E.A. Jäggle, L. Wu, L. Lu, and D. Raabe. Small variations in powder composition lead to strong differences in part properties. <https://www.mpie.de/3476534/Jaeggle.pdf>, May 2016.
- [126] Verein deutscher Ingenieure e.V. VDI 3405 Blatt 2, Additive Fertigungsverfahren - Strahlschmelzen metallischer Bauteile - Qualifizierung, Qualitätssicherung und Nachbearbeitung, 2013.

Bibliography

- [127] H.H. Rossig. *Streckgrenzenüberhöhung und ausgeprägter Fliessbereich vielkristalliner Aluminium-Magnesium-Legierungen*. PhD thesis, RWTH Aachen, 1971.
- [128] G.E. Totten and D.S. MacKenzie, editors. *Handbook of Aluminium: Vol.1: Physical Metallurgy and Processess*. Marcel Dekker, Inc, 2002.
- [129] R-P. Gangloff and B. Somerday, editors. *Gaseous hydrogen embrittlement of materials in energy technologies*. Woodhead Publishing, 2012.
- [130] VACOM Vakuum Komponenten & Messtechnik GmbH. Outgassing Rates of Aluminum compared to Stainless Steel. <https://www.vacom.de/en/>, Retrieved from 04-03-2017.
- [131] E. Brandl, U. Heckenberger, V. Holzinger, and D. Buchbinder. Additive manufactured AlSi10Mg samples using Selective Laser Melting (SLM): Microstructure, high cycle fatigue, and fracture behavior. *Materials & Design*, 34:159–169, 2012.
- [132] ASTM International. ASTM E1820 Standard Test Method for Measurement of Fracture Toughness, 2008.
- [133] K. Hockauf. *Ermüdungs- und Rissfortschrittsverhalten ausscheidungshärtbarer ultrafeinkörniger Aluminiumlegierungen*. PhD thesis, TU Chemnitz, 2011.
- [134] P.S. Pao, H.N. Jones, S.F. Cheng, and C.R. Feng. Fatigue crack propagation in ultrafine grained Al-Mg alloy. *International Journal of Fatigue*, 27:1164–1169, 2005.
- [135] E. Beyer. *Schweissen mit Laser: Grundlagen*. Springer- Verlag Berlin Heidelberg, 1995.
- [136] F.J. Gürtler, M. Karg, M. Dobler, S. Kohl, I. Tzivilsky, and M. Schmidt. Fatigue properties of AlSi10Mg obtained by additive manufacturing: Defect-based modelling and prediction of fatigue strength. *Solid Freeform Fabricaton Symposium - Proceedings*, 2018.